Title
Exploring novel concepts of x-ray radiation generation

Permalink
https://escholarship.org/uc/item/9cx419db

Author
Hakimi, Sahel

Publication Date
2020

Peer reviewed|Thesis/dissertation

UNIVERSITY OF CALIFORNIA,
IRVINE

Exploring novel concepts of x-ray radiation generation

submitted in partial satisfaction of the requirements
for the degree of

DOCTOR OF PHILOSOPHY

in Physics

by

Sahel Hakimi

Committee:
Professor Franklin Dollar, Chair
Professor Toshiki Tajima
Professor Christopher Peter James Barty

2020

DEDICATION

To my family

TABLE OF CONTENTS

LIST OF FIGURES

LIST OF TABLES

ACKNOWLEDGMENTS

First, I would like to thank my advisors, Toshiki Tajima and Franklin Dollar. I am grateful for the opportunity to be a part of the frontier research on x-ray driven wakefield acceleration in nanotubes as well as the quest for bringing a suitable x-ray source to reality via Thin Film Compression. I benefited from discussions with professor Tajima about the theory of LWFA and ion acceleration, history of the field from its beginning, the many impactful applications it has and how to get there in the future. To professor Dollar, I was lucky that the timing of my graduate years matched your first years at UCI. It was a unique experience to be able to set up a new lab, learn the detail of every component and design an experimental setup from scratch. Thank you for making your lab available to me, letting me pursue my topic of interest, and advising me along the way. I am grateful for the opportunity to work on the kHz LWFA experiments at your lab and be a part of other ongoing projects. Thank you for making time to answer my questions and chat about physics at all levels from fundamentals to grand visions for future.

I would also like to thank professor Roger McWilliams and Christopher Barty for insightful conversations about physics of lasers and plasmas as well as career options. I also like to thank Dr. Ales Necas from TAE and Arnold Guerra from UCI for physics conversations over coffee breaks.

I have to thank my friends and colleagues who made the last five years eventful: Calvin Lau, Yoonwoo Hwang, Agnese Lagzda, Brian Casas, Bella Abolfathi, Luke Stagner, Scott Nicks, Sam Taimourzadeh, Deano Farinella, Tam Nguyen, Freida Rivera, Yasmeen Mustafa, Danny Attiyah, Amina Hussein and the ones who spent countless hours with me in the lab: Nick Beier, Hunter Allison and Matthew Stanfield.

I should also thank Dr. Vladimir shiltsev for inviting me to the first workshop on beam acceleration in crystals and nanostructures at Fermilab, giving me a chance to present my research and learn from other presenters. A portion of the work presented here was done at CUOS, with the HERCULES system. I want to thank professor Karl Krushelnick and Alec Thomas for this opportunity, John Nees and Anatoly Maksimchuk for their daily help with the experiment, and Yong Ma for conducting the experiment with me and Nick.

I had a few mentors prior to becoming a graduate student at UCI who had critical roles in my journey and I would like to sincerely thank them. To professors Cynthia Cattell, James Kakalios and Robert Lysak, thank you for your guidance and support during my years at University of Minnesota. To Dr. Misty Davies, thank you for the opportunity to work with you at NASA Ames center and for teaching me the foundation of machine learning algorithms early in my career. To professor James Rosenzweig and Oliver Williams, thank you for introducing wakefield theory to me and allowing me to work with you at UCLA to improve my technical skills as a researcher.

I want to thank my family, my parents, grandparents, uncles and aunt, for their love and support. I want to thank Armin for going through this journey with me. I look forward to

the next chapters of our lives together.

Portions of this work is reproduced with permission from material published or intended to be published. The corresponding copyright statements are given below.

Reproduced from "S. Hakimi, T. Nguyen, D. Farinella, C.K. Lau, H. Wang, P. Taborek, F. Dollar, and T. Tajima, Wakefield in solid state plasma with the ionic lattice force, Physics of Plasmas. (2018) 26;25(2):023112."

Reproduced from "S. Hakimi, X. Zhang, C.K. Lau, P. Taborek, F. Dollar, and T. Tajima, X-ray laser wakefield acceleration in a nanotube, International Journal of Modern Physics A. (2019) 10;34(34):1943011."

Reproduced from "Y. Ma, D. Seipt, A.E. Hussein, S. Hakimi, N. Beier, S.B. Hansen, J. Hinojosa, A. Maksimchuk, J. Nees, K. Krushelnick, A.G. Thomas, and F. Dollar, Polarization-Dependent Self-Injection by Above Threshold Ionization Heating in a Laser Wakefield Accelerator, Physical Review Letters. (2020) 16;124(11):114801."

CURRICULUM VITAE

Sahel Hakimi

EDUCATION

Doctor of Philosophy in Physics   **2020**
University of California, Irvine   *Irvine, California*

Master of Science in Physics   **2012**
University of Minnesota, Twin Cities   *Minneapolis, Minnesota*

Bachelor of Science in Physics   **2010**
University of Minnesota, Twin Cities   *Minneapolis, Minnesota*

Bachelor of Science in Astrophysics   **2010**
University of Minnesota, Twin Cities   *Minneapolis, Minnesota*

PEER-REVIEWED PUBLICATIONS

Simultaneous ground and satellite observations of discrete auroral arcs, substorm aurora, and Alfvenic aurora with FAST and THEMIS GBO **2013**
C. A. Colpitts, **S. Hakimi**, C. A. Cattell J. Dombeck M. Maas

Journal of Geophysical Research : Space Physics 118, 6998-7010

Observation of acceleration and deceleration in gigaelectron-volt-per-metre gradient dielectric wakefield accelerators **2016**
B. D. O'Shea, G. Andonian, S. K. Barber, K. L. Fitzmorris, **S. Hakimi**, J. Harrison, P. D. Hoang, M. J. Hogan, B. Naranjo, O. B. Williams, V. Yakimenko, and J. B. Rosenzweig

Nature Communications 7, 12763 (2016)

Wakefield in solid state plasma with the ionic lattice force **2018**
S. Hakimi, T. Nguyen, D. Farinella, C. K. Lau, H. Wang, P. Taborek, F. Dollar, and T. Tajima

Physics of Plasma 25, 023112

Demonstration of thin film compression for short-pulse X-ray generation **2019**
D. M. Farinella, M. Stanfield, N. Beier, T. Nguyen, **S. Hakimi**, T. Tajima, F. Dollar, J. Wheeler and G. Mourou

International Journal of Modern Physics A 34, 1943015

X-ray Laser Wakefield Acceleration in a Nanotube **2019**
S. Hakimi, X. Zhang, C. Lau, P. Taborek, F. Dollar, and T. Tajima

International Journal of Modern Physics A 34, 1943011

Polarization-dependent self-injection by above threshold ionization heating in a laser wakefield accelerator **2020**
Y. Ma, D. Seipt, A. E. Hussein, **S. Hakimi**, N. F. Beier, S. B. Hansen, J. Hinojosa, A. Maksimchuk, J. Nees, K. Krushelnick, A. G. R. Thomas and F. Dollar

Physical Review Letters 124, 114801

Few Cycle EUV Continuum Generation via Thin Film Compression **2020**
M. Stanfield, H. Allison, N. Beier, **S. Hakimi**, A. E. Hussein, and F. Dollar

Conference on Lasers and Electro-Optics

MANUSCRIPTS IN PREPARATION

Electron Dynamics in the High-Density Laser-Wakefield   **2020**
Acceleration Regime
B. S. Nicks, **S. Hakimi**, E. Barraza-Valdez, K. D. Chestnut, G. H. DeGrandchamp, K. R. Gage, D. B. Housley, G. Huxtable, G. Lawler, D. J. Lin, P. Manwani, E. C. Nelson, G. M. layer, M. W. L. Segge- bruch, J. Sweeney, J. E. Tanner, K. Thompson, and T. Tajima

Submitted

Ultrarelativistic kilohertz intensities produced via Thin   **2020**
Film Compression
M. Stanfield, D. Farinella, N. Beier, **S. Hakimi**, H. Allison, A. E. Hussein, and F. Dollar

Submitted

Plasma Temperature Correlation with Electron Accel-   **2020**
eration Processes in Laser Wakefield Acceleration
S. Hakimi, N. F. Beier, Y. Ma, J. Hinojosa, S. B. Hansen, A. E. Hussein, A. Maksimchuk, J. Nees, T. Tajima, K. Krushelnick, A. G. R. Thomas and F. Dollar

In preparation

ABSTRACT OF THE DISSERTATION

Exploring novel concepts of x-ray radiation generation

By

Sahel Hakimi

Doctor of Philosophy in Physics

University of California, Irvine, 2020

Professor Franklin Dollar, Chair

Laser Wakefield Acceleration (LWFA) is a promising technique for the development of compact particle accelerators. The resulting electron beams have useful characteristics such as short temporal duration and high brightness. LWFA can also generate x-ray radiation, which can be tailored by properties of the interaction such as target density profile and laser polarization.

This work will discuss the theoretical regime of x-ray driven WFA in a nanotube. In this novel regime, the acceleration gradient is predicted to be on the order of TeV/cm and this is confirmed by modeling x-ray pulses in a nanotube. In this work, we include the effects of ionic motion explicitly and investigate the possibility that the lattice force could couple with the formation of a stable wake structure. We show that wakefield formation and electron acceleration processes are not influenced by the presence of polaritons. The present work indicates the acceleration gradient on the order of TeV/cm, which agrees well with wakefield theory and is consistent with previous findings without the lattice effect. This amounts to the validation by computation of the concept of the solid state plasma wakefield in nanomaterials.

This thesis also includes experimental work designed to study the wavelength scaling of LWFA as the wavelength is decreased. An experimental platform was built in a new laboratory at UCI. The laser system is a commercial system with mJ scale energy and operates

at kHz repetition rate. Generation of a sub-relativistic electron beam was confirmed by detection of bremsstrahlung radiation. This platform can be used to study electron beam and radiation generation with a near single cycle pulse as well as 2ω and 3ω of the laser pulse.

A series of LWFA experiments conducted using the HERCULES laser system are also presented. The results demonstrate that wakefield temperature and dynamics can be determined by the soft x-ray spectra of the interaction. Plasma conditions, the signature of bubble formation and electron injection are imprinted in the xuv data. A decreased self-injection threshold was observed with a circularly polarized laser pulse revealing that self-injection is polarization dependent. A different injection mechanism for a circularly polarized laser pulse is discussed.

Chapter 1

Introduction

1.1 Accelerators in society

One of the earliest particle accelerators was built about 90 years ago by Rutherford, Cockcroft and Walton [1, 2]. Later, Ernest Lawrence built the first cyclotron inspired by the idea of Rolf Wideroe [3, 4, 5]. This was the first compact accelerator as the particles were sent through the same structure multiple times, gaining more energy each time. An excellent overview of cyclotrons is given by Wilfred Basil Mann in [6]. The principle of these traditional accelerators is to use the electric field to accelerate charged particles to higher kinetic energies and use the magnetic field to steer and focus the resulting beam. It is worth noting that the development of this accelerator technology was closely related to advancements in high-power electrostatic radio-frequency (RF) and microwave source technology.

These devices rapidly grew to be an essential part of society as they offer a wealth of applications in discovery science, medicine, environment, industry, and national security [7]. Today, there are more than 30,000 accelerators operating worldwide. A small percentage of these accelerators are used for fundamental science research. These types of accelerators

generate more than 1 GeV energy particles, have km scale lengths and cost billions of dollars to assemble and operate. Majority of accelerators are being used in medical applications ($\sim 45\%$), either for imaging diagnostics or radiotherapy, and in industry ($\sim 40\%$) for surface and bulk modification such as ion implantation. The rest are used for various other applications in material characterization, radioisotope production and low energy accelerators for research [7].

The majority of current accelerators use Radio Frequency (RF) electromagnetic waves inside a hollow cavity, a waveguide. The inherent limitation with these accelerators is the ionization and material breaks-down at electric fields of about 100 MeV/m and in practice the breakdown field is even smaller due to impurities inside the material. All material, except plasma medium, will ionize and break-down. In order to achieve higher energy particles required for some applications or basic research, these accelerators have to be built larger, which makes them costly (and less available) as well.

1.1.1   Applications

The most well-known application for accelerators is their use in discovery science and fundamental research in High Energy Physics. The Largest accelerator in the world, and one of the most complicated devices ever built[1] is the Large Hadron Collider (LHC) in Geneva, Switzerland. LHC is a synchrotron accelerator for proton beams with a 27 km circumference, comparable in size to the city of Paris, which is 30 km in circumference. It is built underground at a depth comparable to the height of a 30-story building, a common practice in order to reduce background noise from cosmic rays and also a way of radiation shielding for those who live nearby. LHC produces 13 TeV of energy in a collision between two proton beams and has contributed to the basic understanding of the fundamental building blocks

---

[1]Along with the National Ignition Facility (NIF) and The Laser Interferometer Gravitational-Wave Observatory (LIGO)

of matter and verification of the standard model. In 2012, LHC confirmed observation of a particle with properties similar to the theoretical Higgs boson, a particle researchers had been searching for during the past several decades.

One of the more relatable applications of accelerators is their use for medical therapy and treatment of cancer by radiotherapy where radiation kills the cancer cells. Particle beams in form of electrons and protons or an x-ray beam can be used to treat cancer. These energetic beams can ionize matter which in turn damage the DNA. The cells with damaged DNA are not able to reproduce and are eliminated through natural processes in the body. The type of beam used depends highly on the size and location of the cancer being treated. For example, x-rays and electrons deposit most of their energy in the surface layers and are not ideal for deeper tumors. On the other hand, protons can be directed precisely towards the cancer cells and deposit their energy at a specific depth due to Bragg peak phenomena [8, 9], increasing their effectiveness for killing cancer cells and dramatically reducing the damage to nearby healthy cells. Although proton beams are preferred for treatment of some tumors, they are not widely available. In fact, there are only about 30 proton therapy centers in the US and some states do not have access to one. It is generally more difficult to accelerate and steer protons and since medical accelerators are currently based on traditional accelerator technology, proton therapy centers are fairly large, very expensive and not widely available. Patients are likely to not notice the large facility behind the treatment room that houses the ion source, the cyclotron and various beam transport and control systems before entering the gantry as shown in Figure 1.1 b and 1.1 c. Newer designs for commercial proton sources with the accelerator on the gantry have become available in the past few years [10]. A typical medical linear accelerator shown in Figure 1.1 a, generating electron and x-ray beams, cost several tens of million dollars to purchase and has an annual operation cost of a few million dollars.

Other notable applications include the use of accelerators as cargo inspection tools to strengthen

the nation's security and accelerator-driven transmutation to convert long-lived isotopes from radioactive processes into more manageable isotopes for better waste-management and environmental safety [7].

(a)

(b)
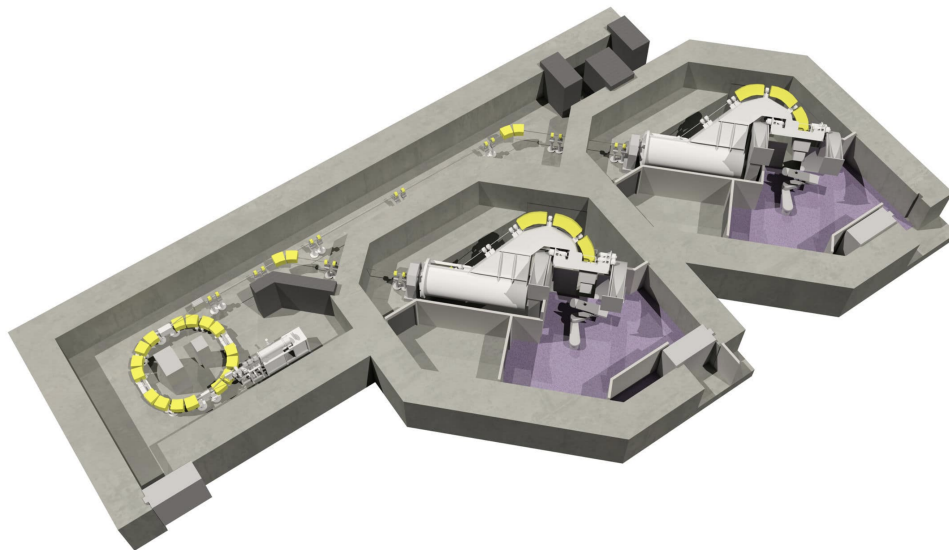
(c)

Figure 1.1: Medical devices for cancer therapy. a) A medical linear accelerator delivering an electron or an x-ray beam is shown. An electron beam from an electron gun and a pulsed radio frequency wave from a magnetron are synced and sent to a waveguide. The wave accelerates electrons to a speed near the speed of light. Electrons can collide with a target to produce an x-ray beam. b) A treatment room for proton therapy center is shown. c) The facility behind the treatment rooms is shown. First, a cyclotron accelerates protons. This proton beam is then sent to the waveguides to be directed to different treatment rooms. Various devices along the path exist for energy selection, focusing and control of the beam parameters. Image credit: Varian

1.2 Advanced accelerators

As mentioned above, any material will eventually reach a break-down limit and this is the limitation for how large the electric field can be in traditional accelerators. In 1956, Veksler suggested an alternative acceleration technology, named "coherent acceleration", where the accelerating field is due to the collection of fields from individual particles rather than externally imposed [11, 12]. Plasma is advantageous because it is already a broken-down medium made up of positive ions and free electrons and it can sustain a large electric field limited only by the plasma density, $E = m_e c \omega_{pe}/e = 96\sqrt{n_e[\text{cm}^{-3}]}$ V/m. Here, m_e and e are the electron mass and charge, c is the speed of light in the vacuum and $\omega_{pe} = \omega_p = \sqrt{(4\pi n_e e^2/m_e)}$ is the plasma frequency. n_e is the electron density in a neutral plasma. This electric field is on the order of 100 GeV/m for typically used plasma densities of 10^{18} cm^{-3}, three to four orders of magnitude higher if compared with the traditional accelerators. Due to this increase in acceleration gradient, plasma accelerators have the potential to be several orders of magnitude more compact compared to traditional RF accelerators with hollow metallic cavities. The ramifications of this is considerable, e.g. medical accelerators used for cancer treatment can become more compact, less expensive and much more accessible for all clinics and hospitals.

In 1979, Tajima and Dawson proposed a laser-driven plasma-accelerator for accelerating electrons [13]. They suggested the use of a high-intensity laser to generate a relativistic longitudinal plasma wave capable of accelerating electrons. This is now commonly known as Laser Wakefield Acceleration (LWFA)[2] technique. In the original paper, the authors required a laser intensity of $\geq 10^{18}$ W/cm^2, which was not available at the time and there was no clear path to its technology in the future either. Further, wakefield should be resonantly excited for the optimal coupling of the laser energy into the wake, i.e. the laser pulse duration should be about half the wavelength of the excited plasma wave. This requires a short pulse laser,

---

[2]This acronym is also used for Laser Wakefield Accelerator

on the order of 100 femtoseconds (fs). To remedy this issue, Tajima and Dawson suggested the use of two lasers with a beat-wave wavelength resonant with the plasma wave [13].

A few years later, the invention of Chirped Pulse Amplification (CPA) [14] enabled experimentalists to have access to lasers at the high-intensity regime needed for implementation of LWFA. It should be noted that generation of an accelerating plasma wave is not limited to photons (a laser beam). The use of electron beams for this purpose was suggested in 1985 [15] and was experimentally verified at Argonne National Laboratory [16], before any LWFA experiment. This was due to the available technology of ultrafast electron bunches (electron beam with required parameters existed before high intensity lasers with suitable parameters became a reality). Other particle species such as positrons and protons could be used too as long as they move at velocities near the speed of light and can establish a charge separation inside the plasma. The charge separation gives rise to a longitudinal plasma wave that can accelerate electrons. In practice, a laser beam or an electron beam have been used widely because of the available technology. Very recently, proton beams from the Super Proton Synchrotron at LHC have been successfully used for plasma wave generation and electron acceleration [17]. Thus, advanced accelerators use a high intensity particle beam to generate an accelerating field in a plasma medium, which can support $1000\times$ higher acceleration gradient.

1.3 Astrophysical relevance

Acceleration of energetic cosmic ray particles is usually described by the Fermi acceleration mechanism [18], where charged particles are scattered by the magnetic clouds repeatedly. However, the origin of ultra-high energy cosmic rays (UHECRs), on the order of $E = 10^{20}$ eV, is still uncertain since it would be very difficult to accelerate particles to such energies by the Fermi acceleration mechanism due to the large number of scatterings necessary and

the energy loss by synchrotron emission. Ebisuzaki and Tajima proposed that a process similar to LWFA is responsible for accelerating particles to these ultra-high energies in the relativistic jets of a accreting blackhole [19, 20]. The basics of this scheme is shown in Figure 1.2. The accretion disk of a supermassive blackhole undergoes transitions between highly magnetized and weakly magnetized states and this generates relativistic Alfven pulses traveling in the direction of the extragalactic jet. The ponderomotive force [21] of the Alfven wave is capable of accelerating nuclei to ultra-high energies in the direction parallel to the jet and without synchrotron radiation loss. Thus, a wakefield formation by Alfven waves may explain the observation of UHECRs in astrophysics as well.
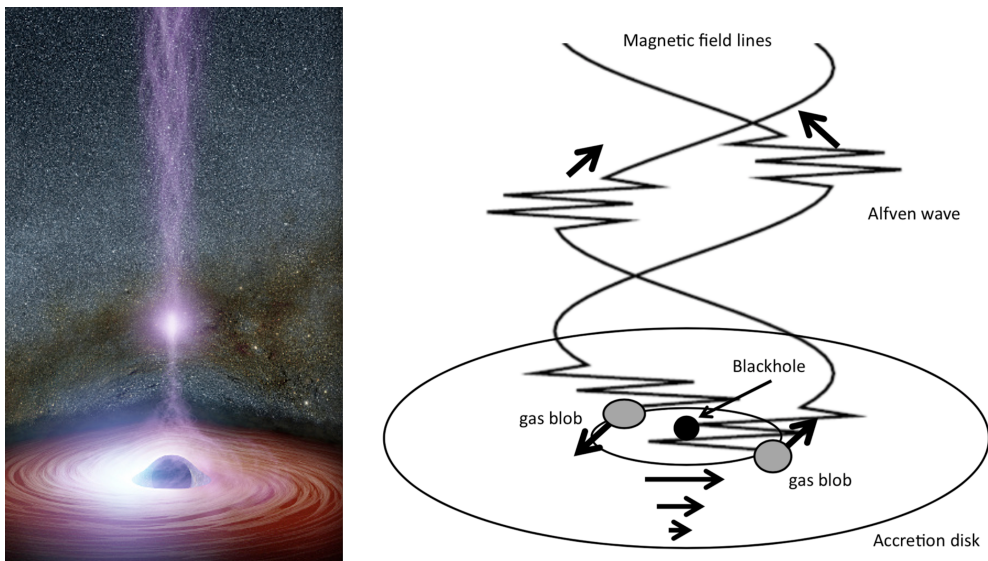
Figure 1.2: Schematic diagram of the production of intensive Alfven waves in an accretion disk. A gas blob formed near the inner edge of the accretion disk severely shakes the magnetic fields and excites relativistic Alfven waves, which propagate along the magnetic field lines of the jet. Image credit: Ebisuzaki & Tajima (2014)

1.4 Laser technology advancement

The laser was first demonstrated 60 years ago [22] using a small synthetic ruby. Laser peak power was soon improved by nearly 100 times with the use of electrical shutters, a

technique known as Q-switching [23]. This enabled the operation of pulsed lasers (0.5-500 ns). Shortly after, mode-locked lasers [24] enabled the generation of femtosecond pulses. The combination of mode-locking and Chirped Pulse Amplification (CPA) techniques with the use of Titanium:Sapphire as the gain medium have made possible the high intensity, ultra-short lasers that we use for LWFA.

1.4.1 Chirped Pulse Amplification
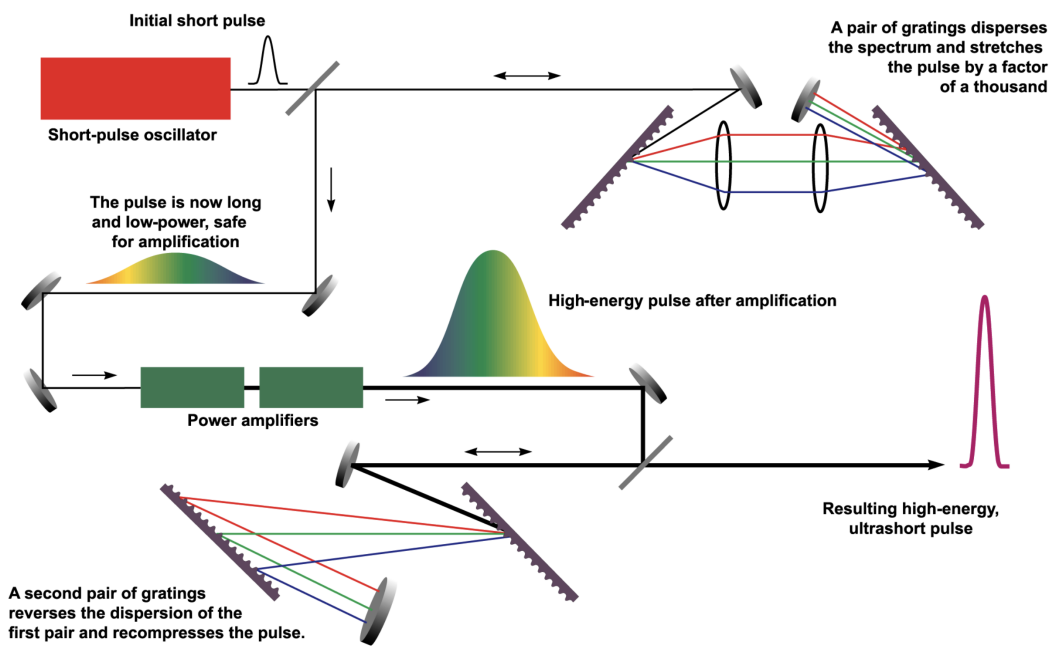
Figure 1.3: The fundamental concept of Chirped Pulse Amplification (CPA) technique is shown. An ultra-short high intensity laser pulse is chirped using a grating pair. The chirped pulse has a longer duration and is amplified inside the amplifier without causing any non-linearity or damage to the system. A matched grating pair is used to compress the chirped pulse to its original duration and producing an ultra-short and ultra-high intensity laser pulse. Image credit: Wikipedia

Particle acceleration via laser-matter interaction (electron acceleration via LWFA and ion acceleration via laser-solid interaction) is tied closely to advancements in laser technology, similar to the dependence of traditional accelerators on the technology of high-power voltage systems. The invention of CPA [14] was critical for experimental demonstration of these

acceleration mechanisms. CPA works by first stretching an ultra-short mode-locked laser pulse in order to avoid non-linear processes that would cause damage inside the amplifier medium. The pulse is then amplified and compressed back down to its short duration as seen in Figure 1.3. This results in an intensity increase by nearly 6 orders of magnitude [25], making a femtosecond pulse with tens of Joules of energy possible. The focused intensity of these pulses are $> 10^{18}$ W/cm^2 [26]. Figure 1.4 illustrates the increase in peak focused intensity in the past several decades.
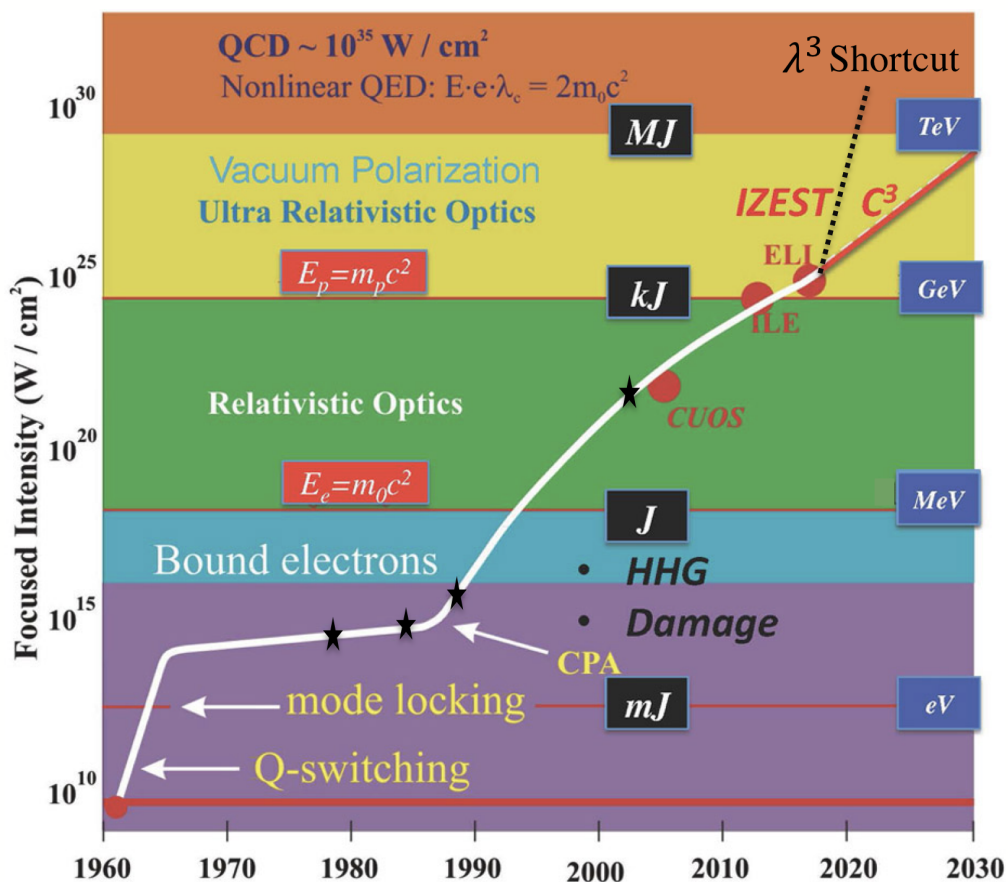
Figure 1.4: Evolution of focused intensity is shown as a function of time. The (λ^3) shortcut to the non-linear QED regime via pulse compression is also shown by a black dashed line. The black stars mark a few events with historical importance: original idea of LWFA (1979), invention of CPA (1985), first experimental demonstration of LWFA (1994) and production of mono-energetic electrons via LWFA (2004). Image credit: Tajima & Mourou (2002)

1.4.2 Single cycle x-ray pulse

The recently proposed technique of Thin Film Compression (TFC) [27] combined with the relativistic compression (RC) technique [28] could generate a coherent single cycle x-ray pulse. TFC technique could be used to compress a commonly existing 30 fs optical pulse to a single cycle optical pulse ($\sim$ 3 fs). The spectrum of the pulse is broadened via Self Phase Modulation (SPM) as the pulse travels through a thin material. This pulse can be compressed down to a shorter duration due to its now broader spectrum. This single cycle optical pulse could then be up-converted to a single cycle x-ray pulse via interacting with an overcritical target described by the Relativistic Oscillating Mirror (ROM) model [29]. This single cycle x-ray could potentially have Joules of energy and duration of a few attoseconds or zeptoseconds, translating to keV energy photons. This is a potential way to reach the ExaWatt regime in the future [30]. If we are able to focus this single cycle x-ray pulse to its much smaller diffraction limited spot size (on the order of nm), we could achieve unprecedented intensities in the Schwinger regime of 10^{29} W/cm^2 [31]. This evolution is shown in Figure 1.4 by a dashed black line, a shortcut to this regime. Thus the combination of TFC and RC techniques beautifully paves the path to a coherent single cycle x-ray pulse as shown in Figure 1.5 with potential applications in LWFA [30, 32, 33] and ion acceleration [34].

1.4.3 Coherent Amplification Network

Some applications need a high current beam requiring lasers to operate at tens of kHz repetition rate with an average power of hundreds of kW. These features do not exist in the current laser systems. However, the International Coherent Amplification Network (ICAN) is working on a solution that involves coherently combining pulses from many fiber lasers. Fiber lasers have a few advantages including a high average power (on the order of kW) and

a high efficiency due to their material properties and fiber's geometry. When the relative phases of the the pulses are controlled and made to constructively interfere, a single high-power output beam is produced [35, 36]. This is one way towards a truly compact accelerator.
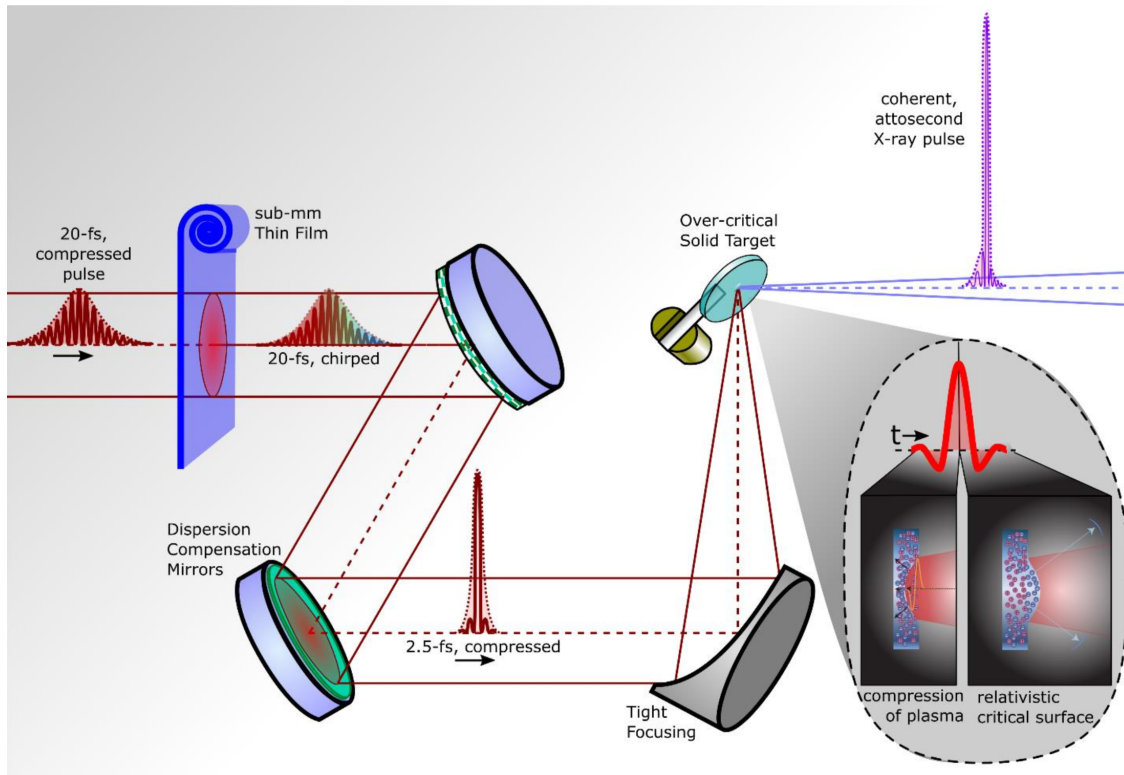
Figure 1.5: Demonstration of the two-stage single cycle coherent x-ray production scheme. TFC setup is shown on the left side where a 20 fs pulse travels through a thin piece of material and is chirped (spectrally broadened) via SPM. Dispersion compensation mirrors are used to undo the linear chirp and compress the beam to its now shorter duration due to a broader spectra. This results in a single cycle optical pulse. The scheme for RC is shown on the right, where this compressed optical pulse is focused onto a solid target. Surface electrons are pushed in and bounce back toward the positive charges. This relativistically compresses the optical pulse to an x-ray pulse. Image Credit: Wheeler (2016)

1.5 A brief survey of LWFA development

The first experimental verification of plasma accelerators was performed at Argonne National Laboratory Advanced Accelerator Test Facility with an intense 21 MeV electron bunch [16]. Shortly after implementation of CPA in laser technology, the first experimental verification of LWFA was demonstrated. A series of proof-of-principle experiments were conducted by different groups in the 1990s, demonstrating the concept of LWFA. Nakajima et al. first demonstrated acceleration of electrons injected into a high amplitude plasma wave generated by the strong interaction of the the laser pulse and plasma in the Self-Modulated LWFA (SM-LWFA) regime [37, 38]. First experimental evidence of trapped electrons, externally injected into the wakefield generated by beating two laser pulses (10.28 and 10.59 μm), was shown in UCLA [39], where a 2 MeV electron beam, collinear with the laser beams was accelerated to 28 MeV. Acceleration of injected electrons in the wakefield of a single ultra-short laser pulse was also demonstrated [40]. All of these pioneering experiments demonstrated a few GeV/m acceleration gradients. First experiment to show efficient trapping of the bulk thermal electrons was conducted using the high intensity VULCAN laser at the Rutherford Appleton Laboratory [41]. This was done in the SM-LWFA regime and triggered wave-breaking evidenced by the detection of large number of electrons and higher energy electrons. Access to the wave-breaking regime provided ~ 100 GeV/m acceleration gradient for the first time. Although demonstrating such a high acceleration gradient is an important milestone, all these experiments produced electron beams with a large energy spread. For most applications, a narrow energy spread is one of the requirements.

A new regime of LWFA, called the bubble regime, was studied by 3D particle in cell simulations [42, 43]. In this regime, the laser pulse is ultra-intense to reach wave-breaking limits and it is also ultra-short to match the resonant condition[3] for optimal coupling. The wakefield is a single cavity that traps a large number of background electrons and accelerate

---

[3] $c\tau_l \approx \frac{1}{2}\lambda_p$

them to high energies. Since the electron bunch is accelerated for the same length and all the electrons see the same electric field, this regime produces a quasi-monoenergetic electron beam. This was experimentally demonstrated in 2004 when three independent groups from France [44], UK [45] and US [46] demonstrated generation of mono-energetic ($< 10\%$ energy spread) electron beams with peak energies on the order of 100 MeV in the iconic "Dream Beam" issue of the Nature journal.

One of the main challenges for LWFA is the control of the acceleration length, which will be discussed in more details in ch. 2. To design a TeV accelerator, a few novel ideas have been proposed. One such idea is the use of 100 acceleration modules, each with its own laser (CAN lasers have been suggested [35]) to excite a wake and provide a 10 GeV energy gain for the electrons [47] for a 2 TeV electron-positron collider. Electrons are trapped in the first stage of the acceleration but there will be no more trapping in the subsequent modules. This technique will require exceptional control over the process because the electron beam would have to be injected in the accelerating phase of the wake in the next stage with fs precision. The transverse spatial alignment should also be on the order of sub-micrometer in order to maintain a high quality electron beam. The development of just a single stage accelerator producing a 10 GeV electron beam has been in the making for the past decade. The next milestone after the "Dream Beam" issue, was the generation of a GeV electron beam by guiding the laser pulse in a plasma channel in 2006 [48] by a group at the Lawrence Berkeley National Lab (LBNL). A ≥ 1 GeV beam was later reported [49] by combining several concepts of matched beam size, self-guiding of the laser pulse and ionization induced injection. A few years later, generation of a 4.2 GeV electron beam was demonstrated [50] by LBNL, which held the world's record for the highest energy electron beam generated via LWFA until it was broken in 2019 [51] by the same group. To date, this generation of ~ 8 GeV electron beam in a 9 cm capillary discharge waveguide, is the highest achieved energy in a LWFA experiment and is closest to the candidate for a single module of a 100 modules, 2 TeV electron-positron collider [47].

The achievement of an 8 GeV electron beam was due to controlling and increasing the acceleration length beyond its limiting factor by a clever design of capillary waveguide target system [51]. It is worth noting that other clever concepts on controlling the dephasing length are being explored [52, 53]. Although these concepts are not yet at the point of experimental verification, they could introduce major breakthroughs in the future. The concept of a flying focus [52], could potentially increase the acceleration length enough to make a table-top (~ 5 m) TeV LWFA possible and is currently being studied via simulations [54] at the Laboratory for Laser Energetics.

A TeV accelerator can also be reached by increasing the acceleration gradient by using an x-ray pulse as the driver for generation of a wakefield in a solid medium [30]. The shorter wavelength of an x-ray pulse increases the critical density of the laser and enables the use of a higher density plasma. A portion of the work presented in this thesis explores this concept by numerical simulations.

Since the "Dream Beam", many more experiments demonstrated LWFA in different regimes and the field has been growing steadily with novel ideas being explored at different institutions.

1.6   Dissertation outline

This thesis describes the theoretical regime of x-ray driven WFA and its study via simulations. It also includes experimental study of LWFA with an 800 nm laser in two different facilities: the Dollar lab at UCI, which has a commercial kHz system with 7 mJ of energy output and the CUOS, which houses the 300 TW HERCULES laser system with energy output of 2 J.

Chapter 2 describes the necessary physics background for the topics discussed in this dis-

sertation. Chapter 3 discusses the experimental setups, the main diagnostics and their development. A brief description of Particle in Cell (PIC) codes is included in this chapter as well. Chapter 4 examines x-ray WFA in a nanotube medium with a series of simulations in 1 and 2 dimensions. Since a suitable x-ray source for LWFA is currently not available, 2ω and 3ω of an 800 nm laser can be used to study the wavelength scaling (toward shorter wavelengths) of LWFA, which can be done with commercial lasers with small transverse profile. Chapter 5 summarizes the preliminary results from experiments done at UCI with the goal to study wavelength scaling and enhancement of betatron radiation. Chapter 6 discusses a series of experiments done at CUOS with the HERCULES system with the addition of an xuv spectrometer diagnostic system. Finally, chapter 7 contains concluding remarks and related future work.

Chapter 2

Theoretical Background

A thorough discussion of laser-driven plasma-based accelerators can be found in a number of previously published review papers [55, 56, 57]. A review paper with an emphasis on ultra-intense lasers and relativistic phenomena is given by [58]. Another review paper with emphasis on the x-ray radiation generation via laser-plasma accelerators is given by [59]. A few short reviews on the different regimes and experimental development of the field are also available in the following references [60, 61, 62, 63, 64, 65, 66]. This chapter provides the detail of the background physics [67, 68, 69, 70, 71] necessary for understanding the theoretical and experimental work described in the later chapters.

2.1 Plasma oscillations and waves

Plasma is a state of matter where electrons are separated from their parent ions by some ionization mechanism. These charges are coupled to each other by their self-consistent electromagnetic forces. This is a complicated system to solve analytically but fortunately it can be greatly simplified by assuming a collisionless plasma. In a plasma, the electric field

contribution is separated into two components with different spatial scales: electric field due to the rapid microscopic motion of individual particles in a scale length smaller than the Debye length, and the electric field due to the long-range electromagnetic force caused by any deviation from charge neutrality over scales greater than or comparable to the Debye length. This second field gives rise to the collective behavior in plasma. Plasma can be assumed to be collisionless when the latter force is much greater than the former; therefore, forces due to local motion and collisions can be ignored as they are negligible and collective behavior dominates. Thus, plasma can be formally defined as an ionized substance with an overall charge neutrality that exhibits collective behavior.

The Debye length is an estimate for the thickness of a charge cloud that would shield a potential due to a local density spike. For charge perturbations with Boltzmann distribution and potential perturbations small compared to the plasma temperature, it can be estimated as:

$$r_{De} = \sqrt{\frac{T_e}{4\pi n_e e^2}}, \tag{2.1}$$

where T_e is the electron temperature and n_e is the electron density. The Debye length could also be thought of as the characteristic length of the charge separation in a plasma. Electrons oscillate about their unperturbed location at the plasma frequency, ω_{pe}, defined as:

$$\omega_{pe} = \frac{1}{\tau} = \frac{v_{Te}}{r_{De}} = \sqrt{\frac{4\pi n_e e^2}{m_e}}, \tag{2.2}$$

where τ is the characteristic time of the charge separation and v_{Te} is the electron thermal velocity. The principal reason for the charge separation is the thermal motion of particles. In this thesis, unless otherwise noted, ions are assumed stationary due to their larger mass while electrons can move inside a plasma medium. This is because the time scale for ion motion in a gaseous plasma is on the order of a few picoseconds (ps) while the laser duration

is $\sim 30\,\text{fs}$. In the case of an x-ray pulse and a nanotube target, the time scale for ion motion is a few fs and the laser pulse is on the order of several attoseconds.
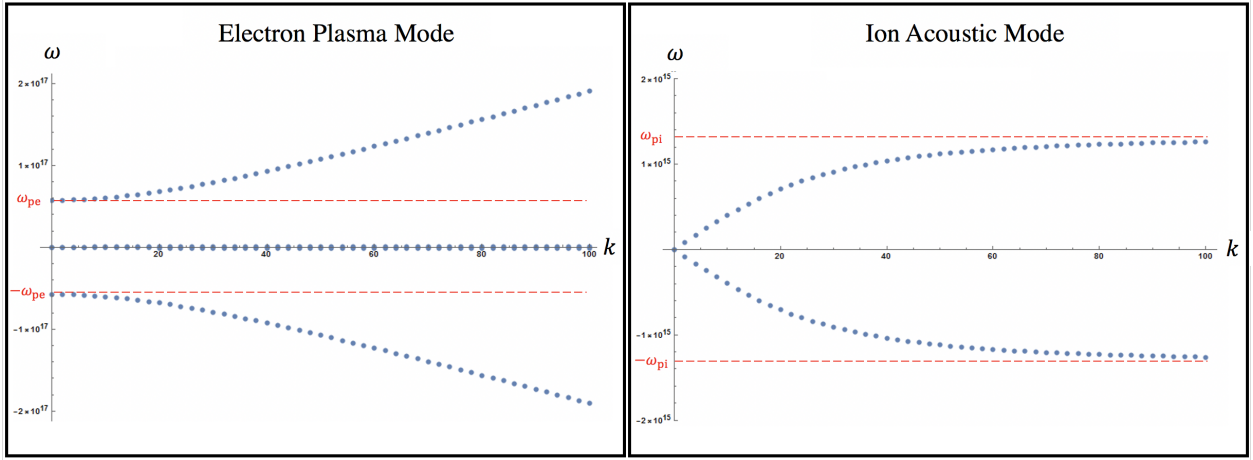
Figure 2.1: Longitudinal plasma modes when external magnetic field is not present is shown for the case where $n_e = n_i = 10^{24}\,\text{cm}^{-3}$. ($\omega_{pe} = 5.64 \times 10^{16}\,\text{rad/s}$, $\omega_{pi} = 1.32 \times 10^{15}\,\text{rad/s}$, $v_{Te}^2 = 3.3 \times 10^{30}\,(\text{m/s})^2$)

If the magnetic field is negligible, plasma can support two collective (electrostatic) modes, an electron plasma wave (also known as the Langmuir wave) and an ion acoustic wave, where the former is a high frequency density modulation wave and the latter is a low frequency density modulation wave. The general plasma dispersion relation can be derived from plasma species continuity equations and equations of motion (the zeroth and first moments of the Vlasov equation), and Poisson's equation. Small amplitude perturbation of density, velocity and electric field is assumed in order to linearize the equations and Fourier theory is used to write $\frac{\partial}{\partial t} = -i\omega$ and $\frac{\partial}{\partial x} = ik_x$. The plasma dispersion relation is given by:

$$\epsilon(k,\omega) = 1 - \frac{\omega_{pi}^2}{\omega^2} - \frac{\omega_{pe}^2}{\omega^2 - k^2 v_{Te}^2}, \tag{2.3}$$

with two solutions, $\omega^2 = \omega_{pe}^2 + k^2 v_{Te}^2$ and $\omega^2 = k^2 c_s^2$, for the plasma oscillation mode and ion acoustic mode respectively. These solutions are shown in Figure 2.1 for the case where $\omega_{pe} = 5.64 \times 10^{16}\,\text{rad/s}$, $\omega_{pi} = 1.32 \times 10^{15}\,\text{rad/s}$, and $v_{Te}^2 = \gamma T_e/m_e = (3)(1)/9.1 \times 10^{-31} =$

18

3.3×10^{30} (m/s)^2. The Langmuir wave is the longitudinal wave that accelerates trapped electrons in LWFA and heats the plasma.

2.2   Laser physics

The propagation of a laser beam can be approximated assuming it has an ideal Gaussian profile or the theoretical TEM$_{00}$ mode. Lasers are not truly Gaussian in reality and any deviations from a theoretical Gaussian is described by a quality factor called M^2, where $M^2 = 1$ is a true Gaussian. The transverse intensity distribution of a Gaussian beam is given by:

$$I(r,z) = I_0 e^{-2r^2/w(z)^2} = \frac{2P}{\pi w(z)^2} e^{-2r^2/w(z)^2}, \tag{2.4}$$

where P is the total power in the beam and $w(z)$ is the radius of $1/e^2$ contour after propagating a distant z and is given by:

$$w(z) = w_0 \sqrt{1 + (\frac{\lambda z}{\pi w_0^2})^2}, \tag{2.5}$$

where w_0 is the radius of $1/e^2$ contour at the plane where the wavefront is flat. This is the one place where the spot size is at a minimum and is known as the beam waist. A laser beam is diffraction limited if the beam waist can be as small as theoretically possible by the laws of optics, approximated by $1.22\lambda f\#$.

A laser pulse with the shortest possible duration for a given bandwidth is called a Fourier Transform Limited (FTL) pulse. Ultra-short pulses have many spectral components and when all components have the same phase, the pulse has its minimum possible duration. For a Gaussian pulse, the minimum duration-bandwidth product is 0.441.

2.2.1 Dispersion

The temporal dependence of the electric field for a Gaussian pulse is given by:

$$E(t) = E_{t0}e^{-2ln2(\frac{t}{\Delta t})^2}e^{-i(\omega_0 t + \phi(t))} + c.c., \tag{2.6}$$

where E_{t0} is the amplitude of the field, Δt is related to the minimum pulse duration, ω_0 is the carrier frequency and is related to the central wavelength of the pulse and $\phi(t)$ is the temporal phase. This definition is intuitive; however, the electric field in the frequency domain is more useful for calculations relating to the pulse dispersion in material. Δt and $\Delta \omega$ are related by the uncertainty principle through $\Delta t \Delta \omega = 4ln(2) = 2\pi C_B$, where $C_B = 0.44$ for a Gaussian pulse. Electric field in frequency domain is given by:

$$E(\omega) = E_{\omega 0}e^{-ln2(\frac{2(\omega - \omega_0)}{\Delta \omega})^2}e^{-i(\phi(\omega - \omega_0))}. \tag{2.7}$$

It is common to Taylor expand the spectral phase, $\phi(\omega - \omega_0)$, around the central frequency. The first term adds a constant value to the phase, the second term introduces a delay to the pulse and the third term is the variation of the group velocity with frequency or the Group Velocity Dispersion (GVD) given by:

$$GVD = \frac{d}{d\omega}\frac{1}{v_g} = \frac{d^2 k}{d\omega^2}, \tag{2.8}$$

$$GVD = \frac{\lambda_0^3}{2\pi c_0^2}\frac{d^2 n}{d\lambda_0^2}. \tag{2.9}$$

The first two terms do not change the shape of the pulse while GVD changes the temporal pulse shape. GVD yields Group Delay Dispersion (GDD) defined by $GVD \times L$, where L is the length of the medium.

2.2.2 Self Phase Modulation

When a very intense laser pulse propagates through material, the refractive index of the medium will change in response to the applied electric field. This is known as the Kerr effect and the intensity dependant refractive index is written as

$$n = n_0 + n_2 I(t) = n_0 + \frac{\chi_{eff}^3}{4n_0^2 \epsilon_0 c}, \tag{2.10}$$

where $I(t) = 2n_0\epsilon_0 c |E_0|^2$ and ϵ_0 is the permittivity of free space.

Self Phase Modulation (SPM) is the change in the phase of a pulse due to the non-linear refractive index of the material. With the assumptions that the medium response to the electric field is instant (on the order of fs) and the length of the medium is small enough to avoid reshaping of the pulse due to dispersion in the medium, the only thing that can happen is a change in the phase of the transmitted pulse, ϕ_{NL}. The expression for the phase is given by:

$$\phi(t) = \omega_0 t - \frac{\omega_0}{c}(n_0 + n_2 I(t))z, \tag{2.11}$$

and $\phi_{NL} = -\frac{\omega_0}{c}n_2 I(t)z$.

The instantaneous frequency, defined as $d\phi/dt$, is $\omega_0 - \frac{\omega_0}{c}n_2\frac{dI(t)}{dt}z$ with the second term representing the change in the instantaneous frequency. This change will not alter the temporal profile of the pulse; however, it will add a positive or negative GDD to it depending on the sign of n_2. If the bandwidth increases and new frequency components are generated due to SPM, the FTL value decreases. In the case of Spectral narrowing, the FTL increases as the pulse propagates through the medium.

2.3 Ionization

One of the main processes in laser-plasma interactions is the ionization of atoms in the target material in order to create the plasma medium. In LWFA, the target material can be a neutral gas plume from a gas-jet or neutral gas contained in a specifically designed gas-cell or a capillary waveguide. In many experiments, the main laser beam is used for both ionizing the target and subsequently interacting with the plasma to generate the wake. It is also possible to use a different laser for ionizing the target prior to the arrival of the main beam.

Atomic intensity is defined as the intensity that matches the binding energy of the electron to the atom for a simple Bohr model [69]. This intensity is about $3.5 \times 10^{16}\,\mathrm{W/cm^2}$. A laser with an intensity greater than this value is guaranteed to ionize any target material. The ionization could also happen at a lower intensity via Multiple Photon Ionization (MPI) and Above Threshold Ionization (ATI). A single photon of $\lambda = 800$ nm will not be able to ionize the target. However, a few of these photons can be absorbed by the atom simultaneously to free an electron as is shown in Figure 2.2 a. In MPI, an electron with binding energy E_{ion} simultaneously absorbs n photons with energy $\hbar\omega$ and is released from the atom with minimal kinetic energy. The probability of this ionization process depends on the number of photons involved in the process (the light intensity) and the ionization rate is given by:

$$\Gamma = \sigma_n I_L^n. \tag{2.12}$$

The cross section, σ_n decreases with n but at a high enough intensity ($> 10^{10}\,\mathrm{W/cm^2}$), ionization will eventually happen. An atom could also absorb more photons that are needed to overcome the binding energy. In this case the electron is freed with a total kinetic energy equal to $s\hbar\omega$, where s is the number of extra photons absorbed. This process is called Above Threshold Ionization (ATI) and is shown in Figure 2.2 b.
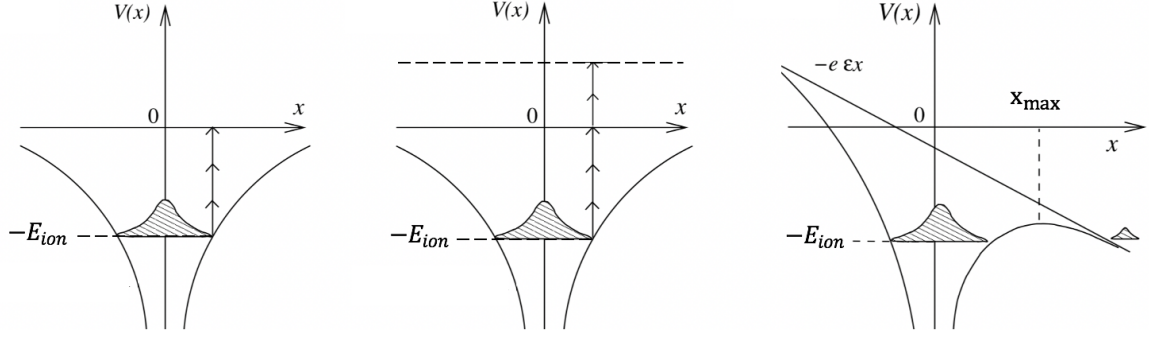
Figure 2.2: a) Schematic picture of Multiple Photon Ionization (MPI). b) Schematic picture of Above Threshold Ionization (ATI). c) Schematic picture of tunneling or Barrier Suppression Ionization (BSI) by a strong, external electric field. Image credit: Gibbon (2005)

When the laser intensity is comparable to the atomic intensity, it can distort the Coulomb field felt by the electrons. In a simple classical model, the modified potential can be written as:

$$V(x) = -Ze^2/x - e\epsilon x, \tag{2.13}$$

and is shown in Figure 2.2 c. According to quantum mechanics, an electron may tunnel through this barrier with a certain probability given by the Keldysh's formula. At $x \geq x_{max} = Ze/\epsilon$, the modified potential is lower than the ionization energy and the electrons will spontaneously escape the potential. This process is known as the Barrier Suppression Ionization (BSI). The separation between multiphoton and tunneling regimes is given by the γ parameter defined as:

$$\gamma = \omega_L \sqrt{\frac{2E_{ion}}{I_L}} \approx \sqrt{\frac{E_{ion}}{\Phi pond}}, \tag{2.14}$$

where ω_L and I_L are the angular frequency and intensity of the laser and ϕ_{pond} is the ponderomotive potential of the laser field. A large laser intensity is needed for modification of the Coulomb field; thus, $\gamma < 1$ is the tunneling regime and $\gamma > 1$ is the MPI regime.

Current high intensity optical lasers can be focused down to μm sizes producing intensities as high as 10^{22} W/cm^2. A gaseous target is usually used in the form of a capillary gas-jet, or a gas-cell to produce the desired density profile for the given laser parameters. As the laser pulse focuses inside this gaseous target, the front edge of the pulse is intense enough to free electrons and transform the gaseous material into a plasma. The peak of the laser pulse then interacts with the plasma and generates a wakefield suitable for accelerating electrons.

2.4 Single electron motion in an electromagnetic field

2.4.1 Electron quiver velocity

Motion of a particle under the influence of an electromagnetic field, $\vec{E}$ and $\vec{B}$, is described by the Lorentz equation (eq. 2.15) and an energy equation (eq. 2.16).

$$\frac{d\vec{p}}{dt} = -e(\vec{E} + \frac{1}{c}\vec{v} \times \vec{B}), \tag{2.15}$$

$$\frac{d(\gamma mc^2)}{dt} = -e(\vec{v}.\vec{E}), \tag{2.16}$$

where $\gamma = \frac{1}{\sqrt{1-\frac{v^2}{c^2}}} = \sqrt{1 + \frac{p^2}{m_e c^2}}$ is the Lorentz factor and $\vec{p} = \gamma m\vec{v}$ is the relativistic momentum. The electric and magnetic fields of the laser can be written in terms of the scalar and vector potentials:

$$\vec{E} = -\nabla\Phi - \frac{\partial\vec{A}}{\partial ct}, \tag{2.17}$$

$$\vec{B} = \nabla \times \vec{A}. \tag{2.18}$$

The normalized electrostatic and vector potentials are given by:

$$\phi = e\Phi/m_e c^2, \tag{2.19}$$

$$\vec{a} = e\vec{A}/m_e c^2. \tag{2.20}$$

We can consider an electron moving in a laser field, written as the product of a sinusoidally oscillating part and an envelope function, $\vec{E}_0(\vec{r})$:

$$\vec{E}(\vec{r},t) = \vec{E}_0(\vec{r})cos(\vec{k}.\vec{r} - \omega t), \tag{2.21}$$

$$\vec{B}(\vec{r},t) = \vec{B}_0(\vec{r})sin(\vec{k}.\vec{r} - \omega t), \tag{2.22}$$

where $\vec{B}_0(\vec{r}) = \vec{E}_0(\vec{r})/c$. An electron initially at rest will start to move due to the electric force at first and as it picks up velocity, the $\vec{v} \times \vec{B}$ term becomes important. Taking the first order approximation of eq. 2.15, $m\frac{d\vec{v_1}}{dt} = -e(\vec{E_1})$, and using eq. 2.21, we can obtain the quiver velocity of the electron oscillatory motion,

$$v_{osc} = eE/\gamma m_e \omega. \tag{2.23}$$

The normalized vector potential of the laser, a_0, can be written as $a_0 = \frac{\gamma m_e v_{osc}}{m_e c} = eE/m_e c\omega$ or $a_0 = \gamma\beta$, where $\beta = v_{osc}/c$. This is an important parameter in the discussion of intense laser-matter interaction. For an $a_0 \geq 1$, the momentum imparted to the electron is equal to or greater than $m_e c$, $(\gamma m_e v_{osc} > m_e c)$. In more practical units, a_0 can be written as a function of laser intensity and wavelength as:

$$a_0 = \sqrt{\frac{2e^2\lambda^2 I}{\pi m_e^2 c^5}} = \sqrt{\frac{I[\frac{W}{cm^2}]}{1.37}}\lambda[\mu m]. \tag{2.24}$$

2.4.2 Ponderomotive force

We can derive an expression for the ponderomotive force by taking the second order approximation of eq. 2.15, $m\frac{d\vec{v_2}}{dt} = -e[\vec{E_2} + \vec{v_1} \times \vec{B_1}]$ and averaging the motion over one laser period to obtain:

$$F_p = -\frac{e^2}{4m\omega^2}\nabla E^2(x).$$ (2.25)

Ponderomotive force results from the oscillation of particles in the electric field of a laser pulse and it is proportional to the negative gradient of the laser intensity. Since the laser intensity is higher near the axis, ponderomotive force will on average push the electrons out and away from the central region. Ions can also experience the ponderomotive force; however, the laser intensity needed to push heavier ions via ponderomotive force, is on the order of 10^{25} W/cm^2, which is not available with the current technology.

2.5 Laser Wakefield Acceleration

LWFA [13, 55] is a plasma-based accelerator, where a single ultra-intense and ultra-short laser pulse is injected into an under-dense plasma and generates a plasma wave, which accelerates electrons. The critical density of a laser depends on the laser's wavelength, $n_{cr} = \epsilon_0 m_e \omega^2/e^2 \propto 1/\lambda^2$. For LWFA, plasma density, n_e, should be less than the critical density to allow the pulse to propagate through the plasma instead of being reflected back[1]. The ponderomotive force of the laser pushes electrons out and away, creating a region of positive charge behind the laser pulse, commonly referred to as the ion cavity. The ponderomotive force pushes ions with the same force but the heavier ions do not move (unless the laser intensity is increased to 10^{25} W/cm^2). This is optimized if the pulse duration is matched

---

[1]This is in contrast with laser-driven ion acceleration where the target should be over-dense.

to 1/2 of the plasma wavelength defined as $\lambda_p = 2\pi c/\omega_{pe}$ restricting the pulse duration to < 100 fs. The charge separation in plasma generates a wave with the plasma frequency ($\omega_{pe} = \sqrt{4\pi n_0 e^2/m_e}$) behind the laser pulse that co-moves with it, known as the wake. The amplitude of this wave can reach and exceed the cold wave-breaking limit, which is sufficient to trap background electrons. Electrons can either be injected into the wake or be trapped from the background plasma. These electrons move with the wake and gain energy for some length. Figure 2.3 illustrates the wakefield structure behind the propagating laser pulse. The electric field inside the ion cavity is well suited for electron acceleration in the longitudinal direction and transverse focusing.
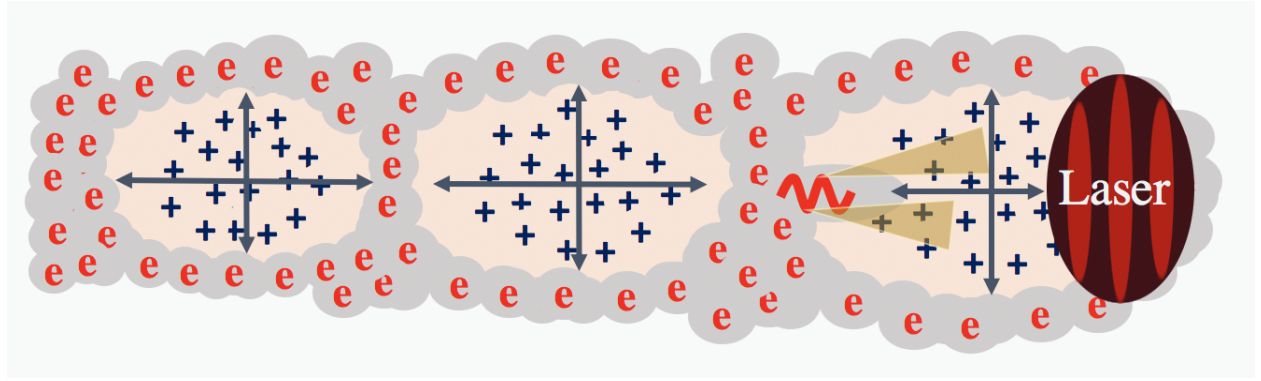
Figure 2.3: Cartoon of a wakefield structure. Laser pulse is propagating through a plasma, pushing electrons away from its path and creating an ion cavity surrounded by a sheath of electrons. Arrows indicate the direction of electric field in both longitudinal and radial directions. Trapped electrons feel an accelerating and focusing force at the end of the first bubble. Since electrons get trapped with a non-zero momentum, they also undergo betatron motion and generate betatron radiation.

The dispersion relation for an electromagnetic wave (in this case, a laser pulse) in a uniform plasma is given by:

$$\omega^2 = \omega_{pe}^2 + k^2 c^2, \tag{2.26}$$

where, ω is the angular frequency of the laser pulse and ω_{pe} is the plasma frequency and is the minimum frequency of a light wave that can propagate through the plasma. If $\omega < \omega_{pe}$,

the wavenumber k will be complex. The imaginary part of k will result in an attenuation of the wave, and the wave becomes evanescent and will not propagate. For a LWFA, the plasma medium should be under-dense ($\omega > \omega_{pe}$) to allow the laser pulse to propagate through the plasma medium and generate a wake continuously until its energy is fully depleted.

The ponderomotive force of the pulse results in a charge separation and generates a relativistic longitudinal plasma wave (the wakefield) behind the driving laser. An intense laser pulse, $a_0 \geq 1$, is required in order to move the electrons relativistically. The produced wakefield has a phase velocity equal to the group velocity of the laser pulse driving it, $v_{ph} = v_{group} = c\sqrt{1 - n_e/n_{cr}}$. It is worth noting here that wakefield phase velocity is much greater than the bulk thermal velocity of the electrons, $v_{ph} \geq v_{T_e}$. Thus, wakefield is stable and is not modifying the bulk plasma as instabilities and landau damping happen when particles and waves can couple to each other ($v_{ph} \sim v_{T_e}$).

The maximum amplitude of the wakefield is an important parameter. If the fluid velocity of the plasma reaches the wake's phase velocity, wake will lose its coherence as the electrons cross the bubble sheets. This is the limit where the density distribution start to have singularities and the wave is said to "break". For a cold plasma, the wave has a maximum amplitude (wave-breaking limit) given by:

$$E_{max} = \frac{m_e c \omega_{pe}}{e}\sqrt{2(\gamma_p - 1)}, \tag{2.27}$$

$$E_{max} = \frac{m_e v_p \omega_{pe}}{e}, \tag{2.28}$$

in the relativistic and non-relativistic regimes respectively.

Particles can be externally injected into the wake structure or be self-injected. Either way, they can ride the wave and gain a considerable amount of energy. The acceleration gradient can reach the non-relativistic wave-breaking electric field limit of $E_{TD} = \frac{m_e c \omega_{pe}}{e}$, which can be written as $E_0[\text{V/m}] \approx 0.96\sqrt{n_0[\text{cm}^{-3}]}$ to show that it only depends on the plasma electron

28

density. For a typical gas density of $n_0 = 10^{18} \text{cm}^{-3}$, acceleration gradients of $E_0 = 100$ GeV/m can be achieved. This is about three orders of magnitude larger than what is possible with the traditional RF accelerators.

2.5.1 Energy gain

As discussed above, the wake produced behind the laser in a LWFA can reach a very high amplitude, E_0. The requirement for maximum energy gain is that the electrons interact with this field for a long distance. The energy gain could be written as:

$$W_{max} = |e| \int_0^L E_0(z)dz, \tag{2.29}$$

where L is the length of acceleration.

2.5.2 Limiting factors

One of the main issues in the design of laser-plasma accelerators to date is the limits on the acceleration length which can be due to three factors: dephasing of electrons, depletion and diffraction of the laser pulse. Acceleration length should be matched with the smallest limiting length for an efficient accelerator design and a maximum energy gain.

It is possible that the accelerated electrons gain enough energy to move faster than the wakefield itself, which is moving at a speed near the speed of light. If this happens, the electrons will outrun the accelerating part of the structure and slip into the decelerating region and start to loose their energy. This distance, known as the dephasing length, is approximately $\lambda_p/2$ in the frame of the wakefield. In the lab frame, it can be calculated from the time it takes an electron moving at the speed of light to travel $\lambda_p/2$ in a frame moving

at v_{ph}:

$$t_{dp} = \frac{\lambda_p/2}{c - v_{ph}}, \tag{2.30}$$

$$L_{dp} = c \times t_{dp} = \frac{\lambda_p c}{2(c - v_{ph})} = \frac{\lambda_p}{c} \frac{\omega_L^2}{\omega_p^2} \propto \frac{\omega_L^2}{\omega_p^3} = \frac{n_{cr}}{n_e^{3/2}}. \tag{2.31}$$

The laser pulse has a finite amount of energy and as it couples to the plasma, it loses energy to it and eventually depletes and can no longer resonantly excite the plasma. This distance, known as the pump depletion length, can be approximated (in the 1D regime) by setting the energy stored in the laser pulse equal to the energy stored in the plasma wave. We assume the resonant condition, $c\tau_L = \lambda_p/2$, and a spot size of πr^2 to obtain the following estimate:

$$\frac{1}{2}\epsilon E_L^2(c\tau_L)(\pi r^2) = \frac{1}{2}\epsilon E_{wake}^2(L_{pd})(\pi r^2), \tag{2.32}$$

$$L_{pd} = \frac{E_L^2(c\tau_L)}{E_{wake}^2} = \frac{(m_e\omega_L c a_0/e)^2(c\tau_L)}{(m_e\omega_{pe}c/e)^2(a_0^4/4)} = \frac{\omega_L^2}{\omega_p^2}\frac{\lambda_p}{a_0^2} \propto \frac{\omega_L^2}{\omega_p^3}\frac{1}{a_0^2}. \tag{2.33}$$

For a laser pulse with $a_0 \approx 1$, the dephasing and pump-depletion lengths are nearly equal. In the case of $a_0 \gg 1$ ($a_0 \ll 1$), L_{pd} is smaller (larger) than L_{dp}.

A final factor limiting the length of the acceleration is the diffraction length. A focused laser pulse will diffract within a Rayleigh length, Z_R, which is the length that the spot size remains small enough to have a high intensity. The radius of the spot size increases by a factor of $\sqrt{2}$ and the intensity drops by a factor of 2 within the diffraction length defined as:

$$Z_R = \frac{\pi w_0^2}{\lambda}. \tag{2.34}$$

For a very non-linear wake in a low density plasma, L_{dp} and L_{pd} will both be much longer than the diffraction length. A natural process, called the relativistic self-focusing helps keep the laser guided for a length $> Z_R$. There are also methods to externally guide the laser pulse for a length $> Z_R$, for example via pre-ionized plasma in a capillary waveguide, where

the electron density is lower on axis. This density gradient corresponds to a higher refractive index near the axis; Thus, plasma acts to focus the beam (similar to a lens) and balances diffraction.

The most fundamental limiting case is the dephasing length, which is usually the assumed length for the calculation of the maximum energy gain. In the 1D linear case and the 3D non-linear case, the maximum energy gain estimated with L_{dp} is given by:

$$W_{max} = \frac{\pi}{2} m_e c^2 a_0^2 \frac{n_{cr}}{n_e}, \tag{2.35}$$

$$W_{max} = \frac{2}{3} m_e c^2 a_0 \frac{n_{cr}}{n_e}, \tag{2.36}$$

respectively.

2.6 Laser energy consideration with shorter wavelength

One way to increase the energy gain in a LWFA is by using a driver with a shorter wavelength.

Optical Laser (800 nm)	x-ray source (1 nm)
$n_c \sim 10^{21}$ cm^{-3}	$n_c \sim 10^{27}$ cm^{-3}
$n_e \sim 10^{18}$ cm^{-3}	$n_e \sim 10^{21}$ cm^{-3}
$n_c/n_e \sim 10^3$ cm^{-3}	$n_c/n_e \sim 10^6$ cm^{-3}
$\epsilon_e \sim 1$ GeV	$\epsilon_e \sim 1$ TeV

Table 2.1: Comparison of the energy gain in a LWFA driven by an 800 nm pulse versus a 1 nm pulse.

Optical photons have energies on the order of eV while x-ray photons have energies on the order of keV. If a_0 is kept constant[2], increasing the energy of photons by 3 orders of magnitude means increasing the electric field of the laser by 3 orders of magnitude, which

---

[2]assume $a_0 = 3$

also means that the intensity will increase by 6 orders of magnitude as shown here:

$$E_{optical} = a_0 \frac{m_e c}{e} \frac{2\pi c}{\lambda_{optical}} = 1.2 \times 10^{11} \text{ V/cm}, \tag{2.37}$$

$$E_{x-ray} = E_{optical} \times 10^3, \tag{2.38}$$

$$I_{optical} = \frac{\epsilon_0 c E_{optical}^2}{2} = \frac{\epsilon_0 c (1.2 \times 10^{11})^2}{2} = 1.9 \times 10^{19} \text{ W/cm}^2, \tag{2.39}$$

$$I_{x-ray} = \frac{\epsilon_0 c E_{x-ray}^2}{2} = \frac{\epsilon_0 c (E_{optical} \times 10^3)^2}{2} = 1.9 \times 10^{25} \text{ W/cm}^2. \tag{2.40}$$

Assuming a diffraction limited spot size of approximately $1\,\mu\text{m}$ and $1\,\text{nm}$ for the optical and x-ray driver respectively, we have:

$$Energy_{optical} = (1.9 \times 10^{19} \text{ W/cm}^2) \frac{\lambda_{optical}}{c} (\pi w_0^2) \approx 1.6 \text{ mJ}, \tag{2.41}$$

$$Energy_{x-ray} = (1.9 \times 10^{25} \text{ W/cm}^2) \frac{\lambda_{x-ray}}{c} (\pi w_0^2) = \frac{Energy_{optical}}{10^3} \approx 1.6\,\mu\text{J}, \tag{2.42}$$

This shows how the laser energy can be lower when a shorter wavelength is used for LWFA. The total laser energy scales with the wavelength of the laser and can be 1000x smaller for an x-ray pulse. The x-ray pulse we have used for simulations in chapter 4 ($\lambda = 10$ nm), assuming diffraction limited spot size focusing ability, would have about $19\,\mu\text{J}$ of energy. However, the energy might need to be higher realistically since focusing an x-ray pulse to its diffraction limited size will probably be more challenging than doing so for an optical pulse and considering the efficiencies in the process: RC is about 10% efficient in transmitting energy while TFC can be as efficient as 90%.

2.7 Radiation generation
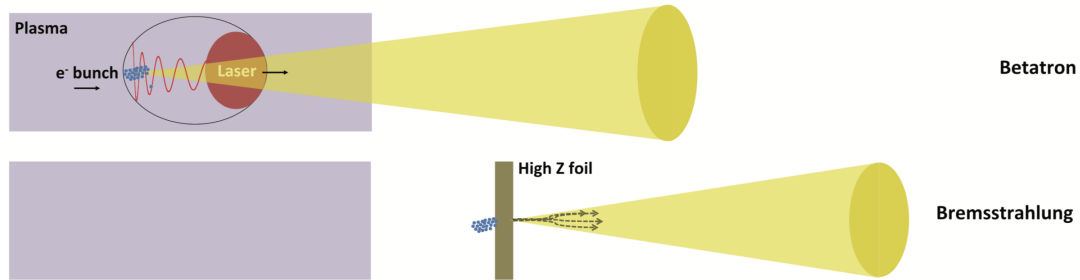
Figure 2.4: Cartoon of two principal LWFA-driven light sources. Top image: Betatron radiation is shown due to transverse motion of trapped electrons. Bottom image: Bremsstrahlung radiation can be produced when the electron beam is made to collide with a high Z material. Image credit: Albert (2016)

2.7.1 Betatron radiation

Electrons can get trapped in the ion cavity with a non-zero transverse momentum. Further, they get trapped away from the laser and plasma wave axis. Due to the transverse (Focusing) force inside the bubble and their non-zero transverse momentum, they continue to oscillate in the transverse direction and generate betatron radiation. The frequency of this oscillation, the betatron frequency, is given by $\omega_b = \omega_p/\sqrt{2\gamma}$. This happens strongly at the two turning points where bending and thus acceleration is at its maximum. This radiation is produced in a narrow cone with a direction tangent to the motion of the electron and is categorized into undulator and wiggler limits. If the maximum angle of the electron trajectory is smaller than the radiation cone angle, the electrons radiate in the same direction at all times, which describes the undulator limit with a narrow spectrum. On the other hand when the maximum angle for electron trajectory is larger than the cone angle, different parts of the trajectory will radiate in different directions and can be spatially decoupled [59]. This is the wiggler limit, which has a broad synchrotron-like spectrum. The characteristics of the radiation in

these different limits are discussed in more detail in [59].

The emitted intensity per solid angle per frequency can be written as:

$$\frac{d^2 I}{d\Omega d\omega} = \frac{e^2 \omega^2}{4\pi c} |\int_{-\inf}^{\inf} \vec{n} \times (\vec{n} \times \vec{\beta}) e^{i\omega(t - \frac{\vec{n}.\vec{r}}{c})} dt|^2, \qquad (2.43)$$

and can be simplified further as shown in [72] for the synchrotron asymptotic limit. The spectrum includes series of harmonics up to the critical frequency of ω_{cr}. The radiated energy decays exponentially for $E > E_{cr} = 3\bar{h} K \gamma^2 \omega_b$, where $K = \gamma r_b \omega_b / c$ is the strength parameter.

2.7.2   Bremsstrahlung radiation

The nucleus of an atom, specially a high Z atom, can deflect an incident electron due to the Coulomb force. Since energy must be conserved, the energy loss from the decelerating electron will be carried out with a photon. The highest possible energy of this photon is equal to the kinetic energy of the incident electron in the case where it comes to a complete stop. This is a continuum radiation and the energy of the incident electron beam determines the intensity and peak of the distribution.

Chapter 3

Methods and Capabilities

The experiments discussed in this thesis were conducted at a brand new laboratory at the University of California, Irvine (UCI) and at the HERCULES laser facility at the Gerard Mourou Center for Ultrafast Optical Science (CUOS) at the University of Michigan, Ann Arbor. This chapter describes the laser systems, experimental configurations, relevant diagnostic systems used for laser and target characterizations as well as computational modeling codes used to simulate laser-plasma interactions. The design and diagnostic systems for the LWFA experimental platform in UCI, which was built from scratch is explained in detail in this chapter.

3.1 CPA lasers

3.1.1 Solstice Ace laser system

The laser system at UCI is the commercial Solstice ACE one-stage amplification system in one compact assembly. The system is composed of four main units: A mode-locked

Ti:Sapphire pulsed laser to provide an ultra-short pulse (seed laser). A Q-switched frequency-doubled neodymium doped yttrium lithium fluoride (ND:YLF) laser to provide the optical energy for amplification of the seed laser in a regenerative amplifier. A regenerative amplifier and a stretcher/compressor unit implementing the CPA technique to produce an intense ultra-short laser pulse at a kHz repetition rate. This system has an $M^2 \sim 1.1$, very close to the theoretical Gaussian mode.
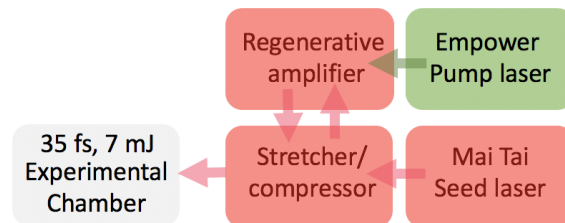
Figure 3.1: Schematic diagram of the commercially available Solstice Ace laser system from Spectra-Physics is shown.

3.1.2 HERCULES laser system

The HERCULES (High Energy Repetition CUOS LasEr System) is a Ti:Sapphire CPA laser system [73]. The system consists of an oscillator, pre-amplifier, stretcher, pulse cleaner, a regenerative amplifier, several multi-pass amplifiers and a compressor. The laser design has been discussed in detail in the following references [74, 75]. The oscillator produces 12 fs pulse with 0.5 nJ energy at a repetition rate of 75 MHz. The spectral bandwidth is ~ 50 nm at the central wavelength of 790 nm. The oscillator is pumped by a Spectra-Physics Millenia neodymium doped yttrium aluminum garnet (Nd:YAG) laser. The pulse is chirped after multiple reflections from the surface of a grating and is stretched to 500 ps. The fluence of the laser is then below the damage threshold of the amplifier. A regenerative amplifier amplifies the pulse to 1 mJ at 10 Hz. A series of multi-pass Ti:Sapphire amplifiers amplify the pulse to 0.6 J, 2 J and 18 J. The pulse is then compressed via reflections from a matched

grating setup in a "Treacy" configurations [76, 77].
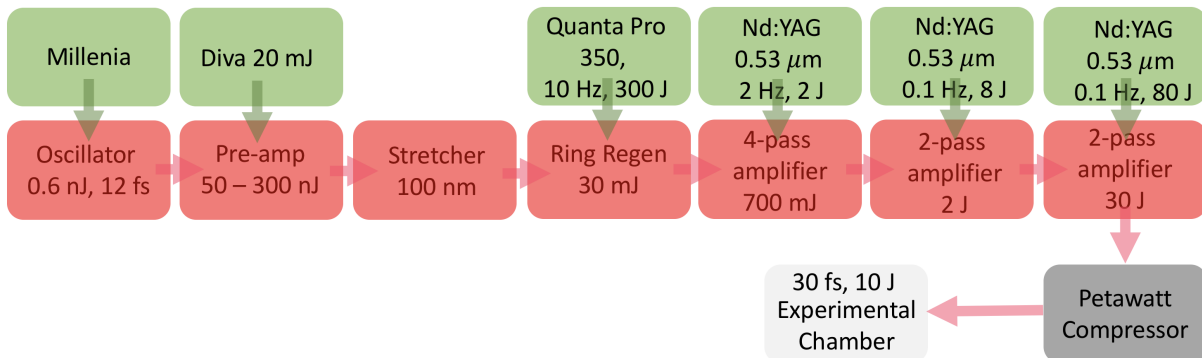
Figure 3.2: Schematic diagram of the HERCULES laser system at the University of Michigan is shown.

3.2 UCI LWFA experimental setup

Solstice output is a $\sim$ 6.75 mJ, 35 fs pulse with $\lambda = 800$ nm at 1 kHz repetition rate. The beam size is $\sim$ 11 mm when it exits the assembly box. The output laser pulse propagates through $\sim$ 3-4 m of air on the optical table and is directed into the experimental chamber by 4 dielectric mirrors and 1 silver coated mirror. Among these mirrors is a 2x telescope with a 1" silver coated convex mirror (ROC = +500) and a 2" dielectric concave mirror (ROC = -1000). The pulse enters a small (8×17 in) rectangular vacuum chamber through a B-coated BK7 window with a thickness of 3 mm. This is the post-compression box where the beam is reflected from a pair of negatively chirped mirrors (-250 fs^2) to compensate for the positive GDD from dispersion and SPM incurred in air and the glass window. The post-compression box is connected to the main experimental chamber (18×30 in) with vacuum components. The laser pulse stays under vacuum and is transported to the interaction region. A 1" gold coated f/2 off-axis parabolic (OAP) mirror is used to focus the beam to $\sim$ 2 μm spot size under a gas-jet with a continuous flow. The diagram of the setup is shown in Figure 3.3.

37
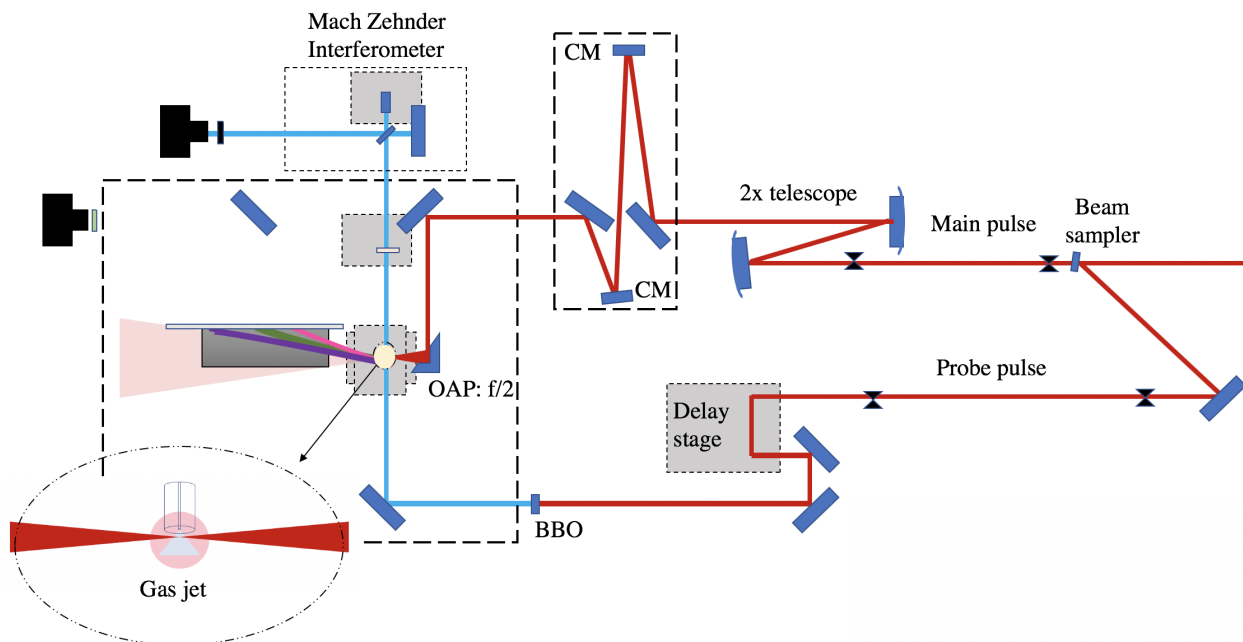
Figure 3.3: Schematic diagram of the experimental setup at UCI.

3.2.1 Laser diagnostics

Pulse energy

The pulse energy out of the box is 6.75 ± 0.10 mJ. A power meter was used to measure the pulse energy before and after each optic in the experimental setup. About 74% of the pulse energy remained in the beam after the focusing OAP. The energy loss due to scattering from the OAP was measured using a 50 μm pin-hole and a photodiode to be $< 1.5\%$. The energy within the Full Width Half Max (FWHM) was measured to be $\sim 30\%$ using a variety of Neutral Density (ND) filters to increase the dynamic range. ND filters are defined by their Optical Density (OD), which indicates the energy absorbed inside the filter. The energy transmitted through the filter is given by T(percent transmission) $= 10^{-\text{OD}} \times 100\%$. At $\lambda = 800$ nm, OD1 is 16% and OD2 is 5% transmissive. Figure 3.4 shows the focal spot images with a variety of OD filters. Energy in the FWHM can be improved using newer

optics with smaller surface roughness. The final energy within FWHM at the interaction region was estimated to be 1.75 ± 0.2 mJ.

(a)

(b)
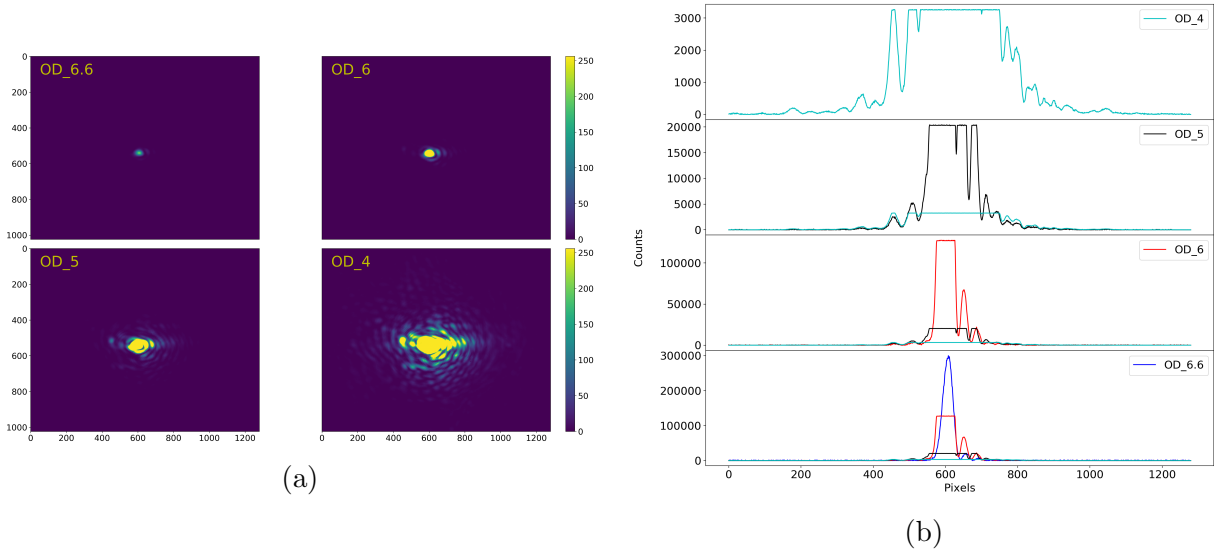
Figure 3.4: a) Focal spot images using a variety of OD filters are shown. The x and y axes show the pixel values and the colorbar shows detected counts with an 8 bit camera. A higher OD filter indicates a lower transmission while a lower OD filter transmits more light, saturating the FWHM region. b) Lineouts of the focal spot images with different ND filters after correcting for the absorption through the filter. This increases the accuracy of the energy measurement by increasing the dynamic range. An estimate for how much energy is contained within the FWHM, is given by the ratio of counts within FWHM to the total counts.

Pulse duration and shape

A home-built [78] Frequency Resolved Optical Gating (FROG) [79] was used to measure the pulse duration immediately outside the laser box and at the interaction region, after propagating through several meters of air and a 3 mm thick B-coated BK7 window. The pulse leaving the assembly is measured to be 36 ± 1 fs; however, it is measured to be ~ 60 fs inside the vacuum chamber, after optimization of the compressor setting using the second harmonic signal. This longer pulse duration is due to the combination of linear dispersion, which we can correct with adjusting the compressor, and the non-linear addition of phase due to SPM in the air and the BK7 glass window.

SPM adds a positive GVD to the pulse if $n_2 > 0$, which is the case for both air and BK7 glass medium. Dispersion in these medium also adds a positive GVD to the pulse. In order to have a short FTL pulse at the interaction region, we start with a positively chirped pulse coming out of the laser box. The chirped pulse has a lower intensity, which means SPM effect is somewhat reduced. In addition, a positively chirped pulse experiences spectral broadening, which means the FTL is reduced. The combination of dispersion and SPM, in the air and the vacuum window, adds positive chirp to the pulse. A pair of negative chirped mirrors $(-250$ fs^2) were used inside the vacuum chamber to compress the pulse down to its FTL value. The pulse propagates under vacuum thereafter. A small spectral broadening due to SPM in the air and BK7 glass window was observed and the final pulse duration at the interaction region was measure to be 30 ± 2 fs. Numerical simulation of light propagation in medium was also performed [Matthew Stanfield] using the Python Non-Linear Optics (pyNLO) code, a non-linear Schrodinger equation solver with a split step Fourier method, and the result was in agreement with the measured pulse duration.

FROG is a robust technique to measure the duration of femtosecond pulses. The schematic of a FROG setup is shown in Figure 3.5. The original beam is split into two identical beams, where one of the beams is made to travel through a delay stage. Both beams are overlapped inside a non-linear crystal (BBO). A second harmonic signal is present when the beams are overlapped in both space and time. The delay stage moves in ~ 1 μm steps and intensity and frequency information is recorded at each step. The intensity information alone can be used to calculate the pulse duration, when a pulse structure is assumed. The addition of spectrum data at each stage position, enables a complete characterization of the pulse intensity and phase structure without the need to assume a specific pulse shape. The second harmonic generation FROG trace is given by:

$$I(\omega, \tau) = | \int_{-\infty}^{+\infty} E(t)E(t-\tau)e^{-i\omega t} dt \, |^2 \, . \tag{3.1}$$

An iterative algorithm reconstructs the time-dependant electric field from the measured FROG trace.
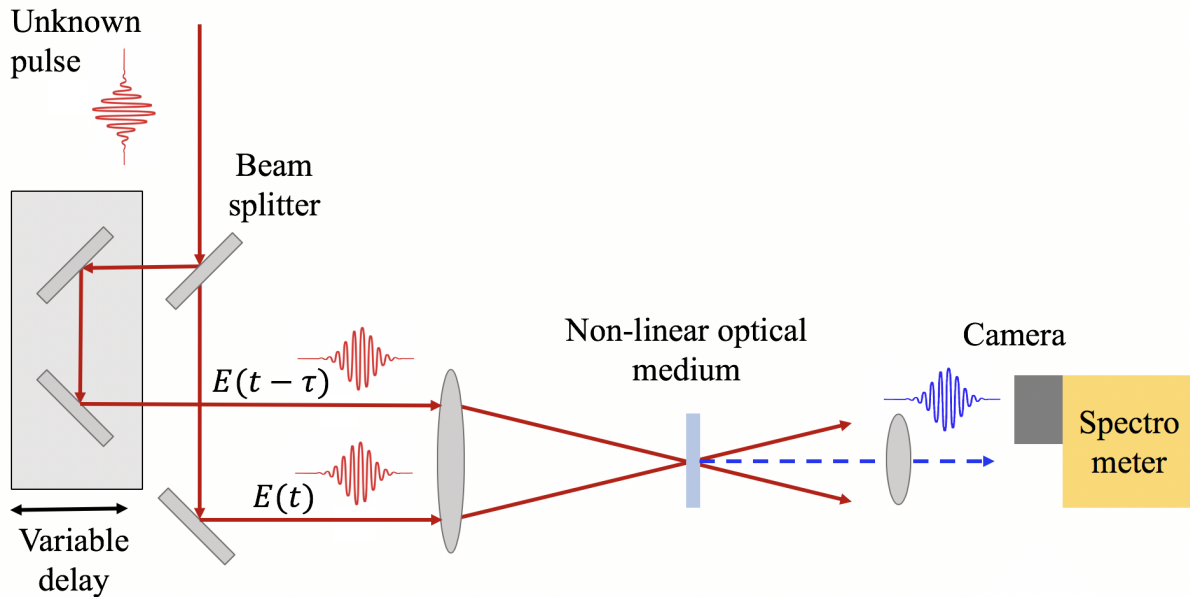
Figure 3.5: The basic geometry of a SHG-FROG is shown. Image credit: Rick Trebino

Laser focal spot

The laser focal spot is measured by a microscope objective lens and a BK7 plano-convex lens, which imaged the light from the objective onto the camera. The energy of the laser pulse was reduced before the objective lens, in order to avoid damaging it. This was done either by using 1-3 glass wedges positioned at 45-55 degrees, near the Brewster's angle, or by operating the laser at the "shuttered" mode. The latter method blocks the oscillator output from entering into the regenerative cavity and only the ASE signal is outputted from the laser box. The comparison of the two measurements were nearly identical. Magnification of the imaging system was calibrated by translating the objective lens $\sim 10 - 40\,\mu$m, recording multiple images and calculating the ratio of the distance moved in μm to the corresponding number of pixels. The OAP was manually aligned using this imaging system by correcting

astigmatism when moving through the focus. Figure 3.6 shows an example of the laser focal spot using an f/2 OAP. The OPA was aligned in air before the chamber was pumped down. The focal spot was stable during the pump-down (moving on the order of $< 1 - 2\,\mu$m in both x and y directions on the camera positioned about 1 m away from the interaction region). Further, the focal spot could be corrected for minor motion under vacuum by adjusting the last mirror before the vacuum chamber.
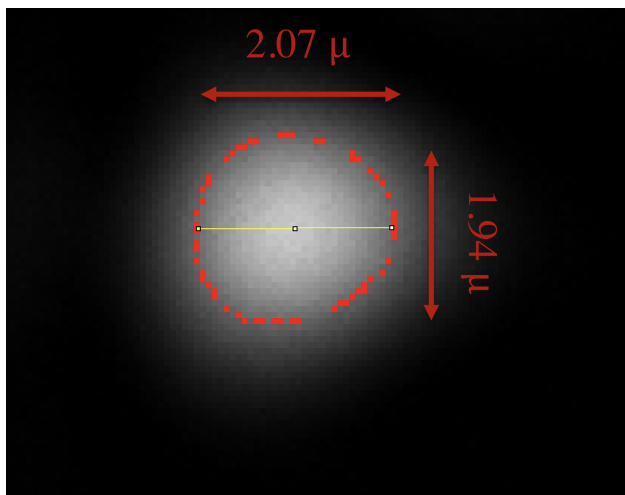
Figure 3.6: Image of a focal spot from an f/2 OAP. The FWHM is measured to be 2.07 × 1.94 μm.

3.2.2 Target

For the experimental setup at UCI, a continuous flow gas delivery system was designed inspired by the high performance liquid chromatography technology commonly used in chemistry. A 1 cm long capillary with inner diameter of 76 or 127 μm made from PEEK material, which are able to sustain high pressure (up to 10,000 PSI), is connected to a gas cylinder via 1/4" plastic and copper tubing. Plastic tubing was used inside the experimental chamber for ease of movement and control of the nozzle position. The nozzle was mounted on an XYZ stage and moved with a computer program. The connection for the gas system is made by appropriate Swagelok fittings and compatible ferules. The experimental chamber is pumped

by a turbomolecular pump (Pfeiffer's HiPace300) backed by a roughing pump (Pfeiffer's Adixen ACP28). The chamber can be pumped down to ~ 0.5 mTorr. The chamber pressure is increased to ~ 5 mTorr with a continuous flow of gas through the $127\,\mu$m nozzle backed by pressure of 350 PSI. Available target material included Argon, Helium and Nitrogen and the density was controlled by the backing pressure, which has a linear relation with the density.

Measurement of electron density

In the case where the magnetic field in the plasma is negligible, the refractive index is approximated by $\eta = \sqrt{(1 - \omega_p^2/\omega^2} = \sqrt{(1 - n_e/n_{cr})}$. Electron density of the plasma medium can be calculated from the measured refractive index of the plasma. Measurements of the refractive index of any medium is usually done by the technique of interferometry. An interferometer is a device where two or more beams are made to interfere with each other by the coherent addition of their electric fields. The modulated intensity pattern is then observed on the plane of a detector. For the experiments in this thesis a folded Mach-Zehnder interferometer, was used. The setup of our Mach-Zehnder interferometer on a removable 12×12 in breadboard is shown in Figure 3.7.

A probe pulse is picked from the main driver pulse by reflection from a beam sampler (10B20-01NC.2 from Newport or a $6\,\mu$m Mylar film from LGC). The probe pulse is steered towards the experimental chamber by several 1" diameter silver coated mirrors and a delay stage with ~ 125 ps temporal range and a BBO crystal ($12 \times 12 \times 0.2$ mm), producing a second harmonic signal with $\lambda = 400$ nm. The shorter wavelength probe produces thinner fringes, and the phase difference through the plasma is larger due to the inverse relation with the wavelength and the dependence of the refractive index on the wavelength. The probe pulse then enters the vacuum chamber through an uncoated BK7 window and is directed towards the interaction region (perpendicular to the main beam) by a 1" aluminum mirror. The probe beam illuminates the interaction region and the vertical plane located

43

at the main pulse propagation axis is imaged, through the interferometer, using a single lens imaging system (focal length = 10 cm, $f/8$). Interferogram data, providing spatial distribution information, is obtained by blocking one arm of the interferometer. Information on the temporal evolution of plasma is obtained by moving the delay stage. The total phase difference induced by the plasma is given by:

$$\Delta\phi(y,z) = \frac{2\pi}{\lambda} \int (1 - \eta(x,y,z))dx, \tag{3.2}$$

$$\eta = \sqrt{1 - \frac{n_e}{n_{cr}}}, \tag{3.3}$$

where λ is the wavelength of the probe beam and η is the refractive index of the plasma and it depends on both the electron density and the laser's critical density as in equation 3.3. To obtain the total phase difference, we integrate over the total length of the plasma that the probe pulse propagates through.
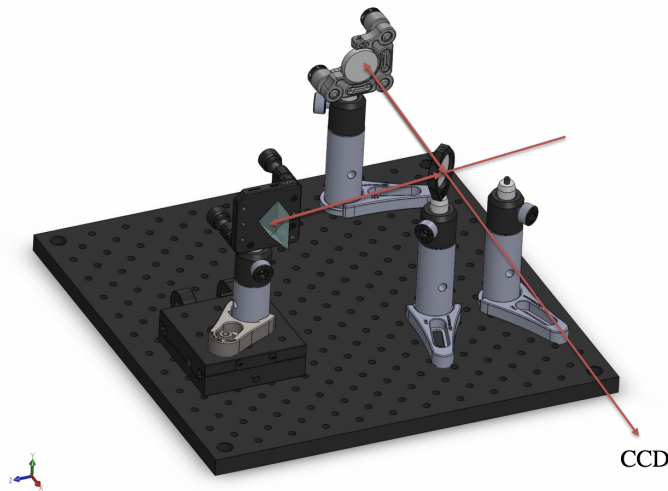
Figure 3.7: Schematic of a compact Mach-Zehnder interferometer using a roof mirror is shown. A roof mirror is used to flip one arm of the interferometer. When both arms overlap, the portion of the beam that has propagated through the plasma is overlapped with a reference portion of the beam, which has not propagated through the plasma. This is possible since the beam diameter (~ 11 mm) is much larger than the plasma region we are imaging (100s of μm).

44

Plasma density is not uniform through the entire length of the plasma. The laser pulse is more intense near the center; hence, more electrons are ionized near the laser axis and the density distribution has a Gaussian profile in x and y directions and it is assumed to be cylindrically symmetric. The flow from the capillary and expansion in the vacuum also gives a Gaussian profile to the target plasma in the z direction, the direction of laser propagation. The 2D projection of phase information, $\Delta\phi$, and the cylindrical symmetry of the plasma can be used to obtain a full 3D density map using the Abel inversion equation:

$$\Delta\phi(r, z) = \frac{1}{\pi} \int_r^\infty \frac{\Delta\phi(y, z)}{dy} \frac{dy}{\sqrt{(y^2 - r^2)}}. \tag{3.4}$$

Calculations of electron density via Abel inversion algorithm were performed using a code written in Python. In order to test the accuracy of the code, fringe shift data was simulated with varying densities and profile shapes. The error in calculation of electron density using this code was $< 2\%$ for noticeable fringe shifts, for example for $n_e = 5 \times 10^{19}\, \text{cm}^{-3}$. The error increased for negligible fringe shifts; it was $\sim 10\%$ for $n_e = 4.5 \times 10^{18}\,\text{cm}^{-3}$. An example of simulated fringe shift and a map of the density profile is shown in Figure 3.8.

Numerical modeling of the density profile through the nozzle was also performed using the COMSOL Multiphysics software and was in agreement with our measured data. Plasma densities up to $\sim 5 \times 10^{19}\, \text{cm}^{-3}$ with longitudinal Gaussian profiles of about 100-300 μm and transverse dimension of $\sim 60\, \mu m$ were produced with our experimental setup. An example of the experimentally observed fringe shift is shown in Figure 3.9.
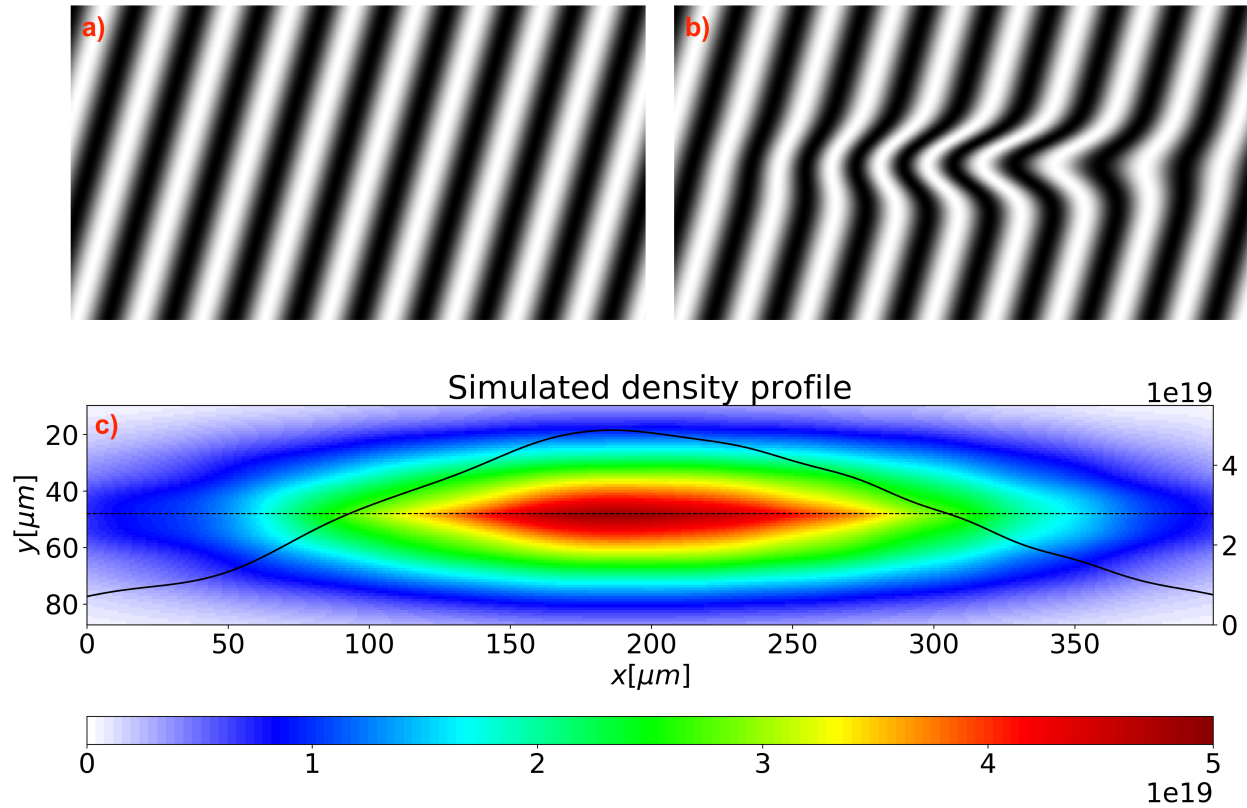
Figure 3.8: An example of simulated fringe shift and the obtained density profile via Abel inversion is shown. a) The simulated unperturbed fringe pattern when a beam of $\lambda = 800\,\mathrm{nm}$ is overlapped with itself through an interferometer is shown. The magnification was chosen to match our experimental imaging system. b) The simulated fringes shift due to propagating through a cylindrical plasma with peak density of $n_e = 4.95 \times 10^{19}\ \mathrm{cm}^{-3}$ and a Gaussian profile. c) The density profile obtained from simulated fringes via Abel inversion analysis.
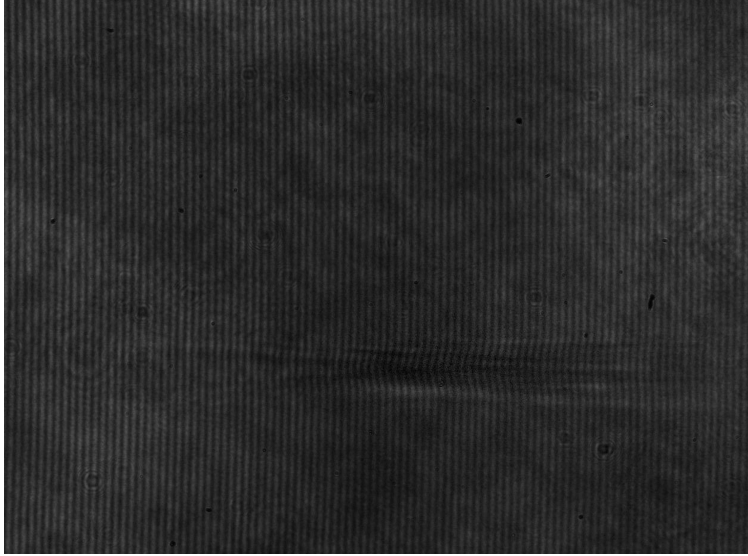
Figure 3.9: An example of the experimentally observed fringe shift due to a backing pressure of 200 PSI is shown.

An example of the experimentally measured density profile with a 76 μm capillary nozzle backed by 520 PSI is shown in Figure 3.10. The on-axis density profile is also shown (right axis) with a peak value of $n_e = 3.1 \times 10^{19}$ cm^{-3}. Peak electron density as a function of backing pressure for this capillary nozzle is shown in Figure 3.11, where the vertical distance from the focal spot to the orifice was ~ 100 μm for all data points.
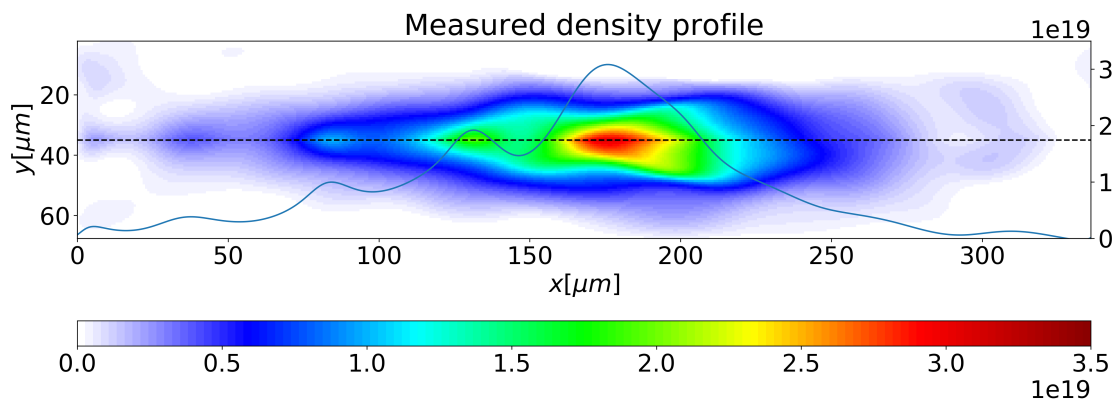
Figure 3.10: The full density profile for a 76 μm capillary nozzle backed by 520 PSI is shown. The laser focal spot is ~ 100 μm above the nozzle. The on-axis electron density profile is shown on the right axis. Peak inferred electron density from phase shift is $n_e = 3.1 \times 10^{19}$ cm^{-3}.
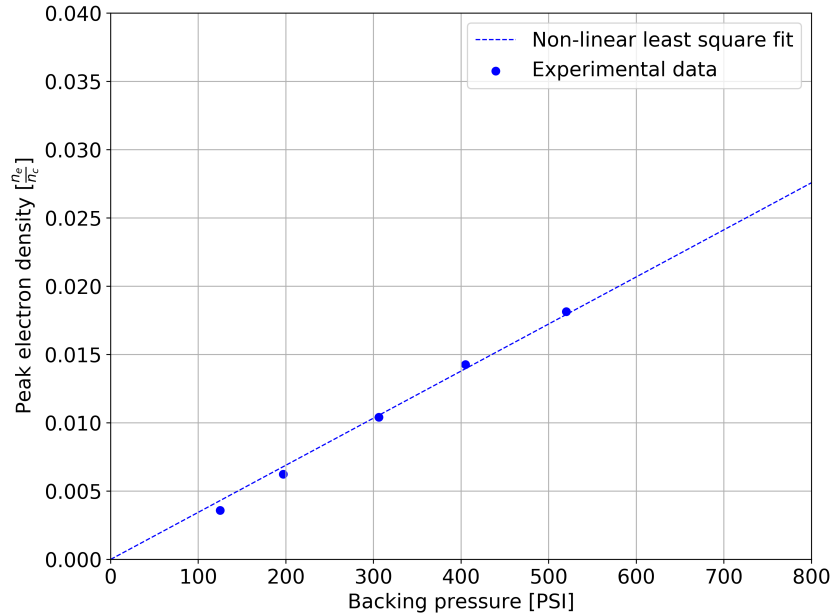
Figure 3.11: The peak electron density as a function of backing pressure is shown for a $76\,\mu$m capillary nozzle.

3.2.3 Detection

Electron detection

A scintillating screen paired with a dipole magnet is commonly used for electron detection. An electron spectrometer is composed of a dipole magnet and a phosphor screen. Our dipole magnet was built with two thin neodymium block magnets (a pair of either BZ0X82, BZX0X02, or BZ0X02 from K&J Magnetics was used) epoxied to blocks of acrylic. The design of the magnet as shown in Figure 3.12 allows for varying separation distance between 1 to 2.5" in order to control the magnetic field strength. The magnetic field was measured using a Gaussmeter and the measured magnetic field was used to model electron trajectories via COMSOL Multiphysics modeling software. The magnetic field map for a pair of BZ0X82

magnets at various distances are shown in Figure 3.13. Geometry of electron deflection in the magnetic field is shown in Figure 3.14. This geometry was used to calculated the range of electrons that would be detected on the screen. The actual magnetic field was used to model electron trajectories. The modeled electron trajectories are shown in Figure 3.15 where each color represents the path for a different energy electron beam.
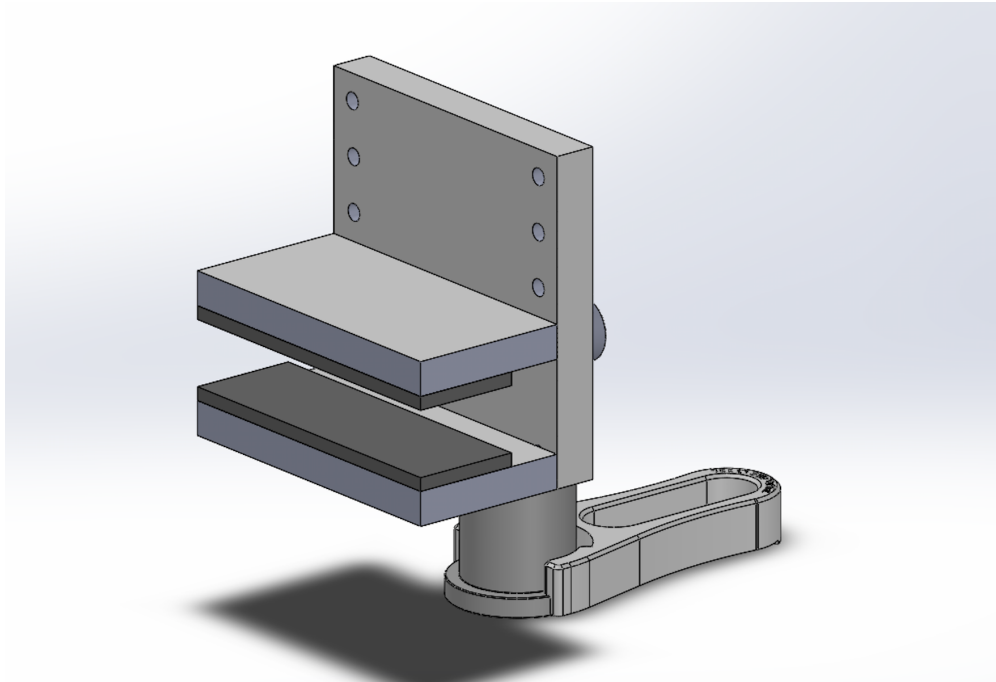
Figure 3.12: The dipole magnet with vertically adjustable mount allowing flexibility and control over the magnetic field strength and the range of electron energy to be detected.

We used Carestream LANEX fine screen, a phosphor screen that converts energetic electrons into green light. The composition of fine LANEX screen is $10\mu m$ of protective coating, $178\mu m$ of plastic substrate, $84\ \mu m$ of rare earth material, Gd_2O_2S, and a final $5\ \mu m$ of protective coating [80]. When energetic electrons interact with a phosphor screen, they excite electrons in the screen. The electrons decay to their ground state and emit radiation at a wavelength of $\sim 545\ nm$. LANEX screen is imaged by a camera through a BG-39 (Schott Glass) filter, which transmits light in 400-550 nm range.
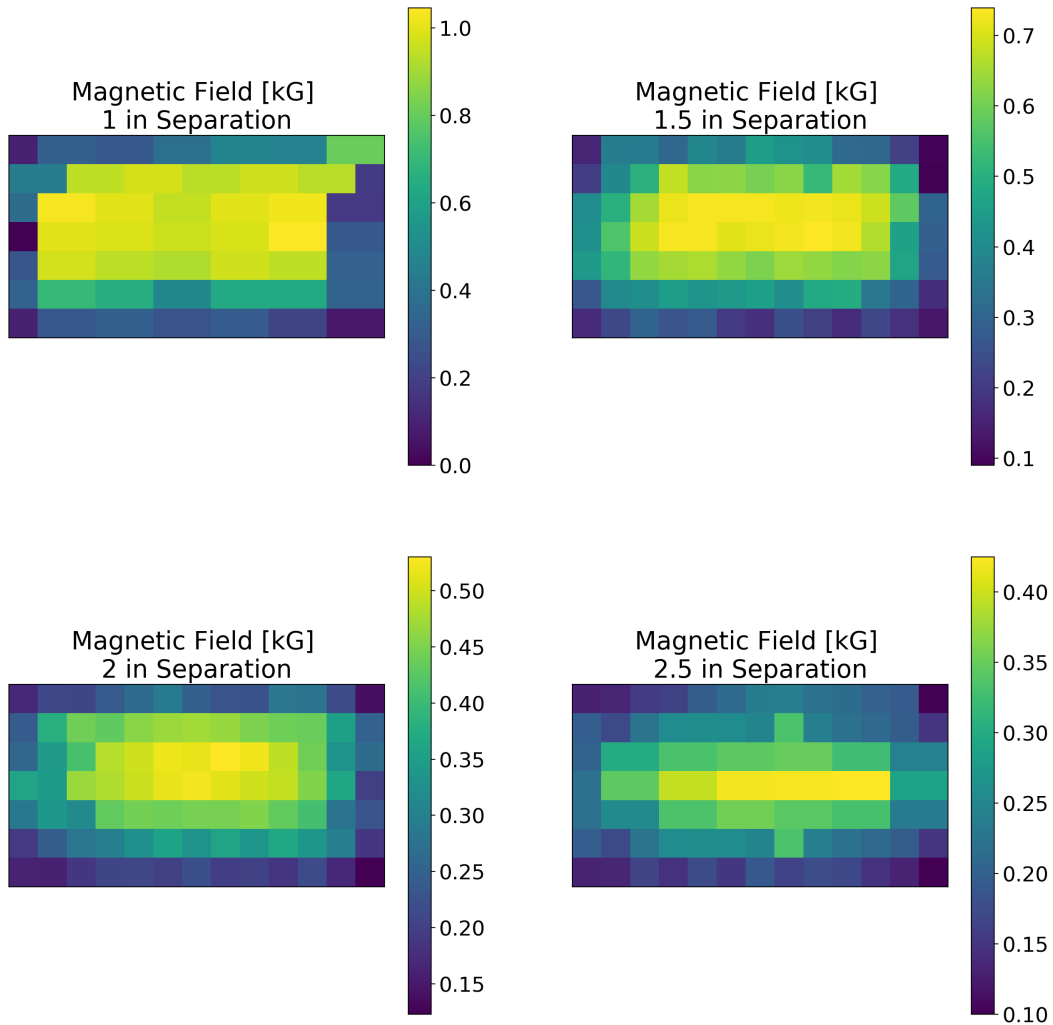
Figure 3.13: The measured B-field of a dipole magnet (a pair of BZ0X82 magnets) is shown at various magnet separation. The magnetic field is more uniform when separation is smaller. This measured field was used for modeling the trajectory of electron beams with different energy. At 1" separation, the range of electron energy is between 50 keV and 2 MeV.
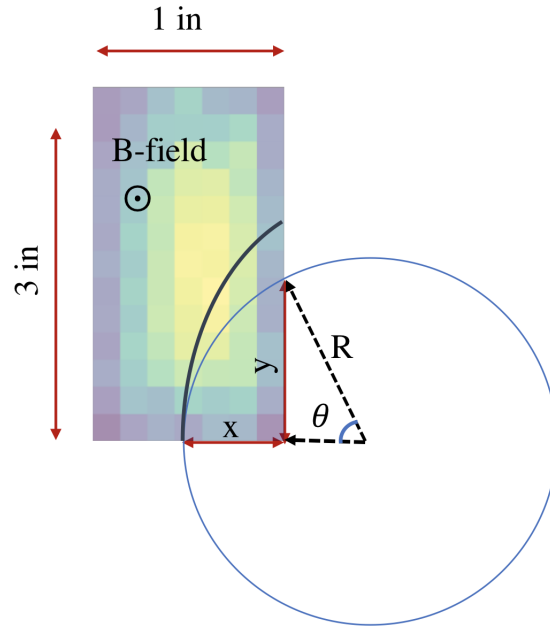
Figure 3.14: Geometry of an electron deflection in the spectrometer. The region with magnetic field is marked with colors. Electrons can enter this region through a 1 mm slit and are deflected according to $R = \frac{m_e c}{qB} \sqrt{\gamma^2 - 1}$.
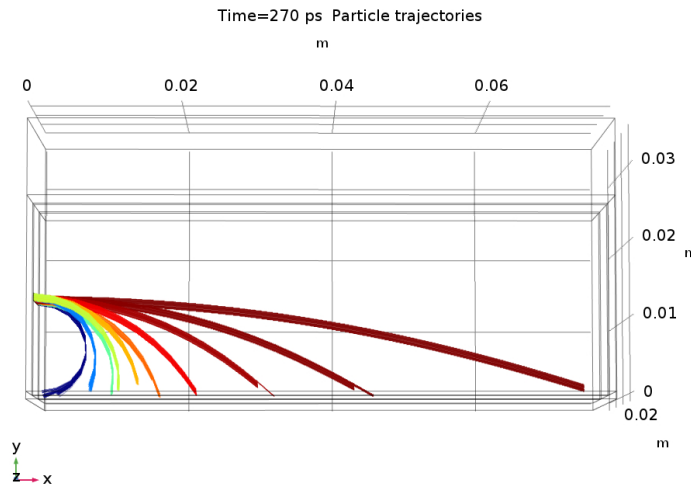
Figure 3.15: Particle tracking via COMSOL Multiphysics software. The range of electron energy shown here is between 2 and 16 MeV for a pair of BZ0X02 magnets at 1 cm separation.

3.3 HERCULES experimental setup

The laser pulse ($\sim$ 2 J, 35 ± 3 fs) propagates from the compressor to the experimental chamber under vacuum. The beam is a quasi flat top with a 4" beam size. The focusing optic is an f/20 OAP providing a $\sim$ 20 μm focal spot. The laser power is measured for each shot with a photodiode behind a dielectric mirror that leaks 1% of the beam through. Inside the experimental chamber, another leak through of the beam is imaged and used to correct the beam pointing. To image and correct the focal spot, a motorized stage moves two mirrors in the path of the focusing beam, which is then sent to an imaging system. After removing these mirrors, the laser pulse propagates to the target and is focused inside a variable length gas-cell. Gas-cells are used to provide a more uniform density profile and improve the stability of the produced electron beams[1]. To facilitate ionization injection, helium with a few % nitrogen is used where the density is controlled by the backing pressure. Parameters such as compressor setting, gas-cell position and backing pressure are scanned to optimize the produced electron beam. Target density is measured with a folded Mach Zehnder interferometry system. Electron energy spectra is measured with a 15 cm long, 0.8 T dipole magnet and a (regular) LANEX screen that is imaged through a BG-39 filter. Electron energy can be measured in the range of 40 to 600 MeV. The electron beam profile can also be measured with placement of a LANEX in front of the beam.

3.4 Numerical modeling

Numerical modeling has proven to be of utmost importance for both design of experiments involving laser-plasma interactions and understanding the result. These interactions involve millions of particles that will move self-consistently according to the electromagnetic field of the laser and plasma constituents. A true microscopic simulation for the motion of each

---

[1]Two stage gas-cells are specifically designed to separate the injection and acceleration stages.

particle or even a subset of particles is not possible; thus, models usually use simplified approximations. One of the most popular algorithms is the particle-in-cell (PIC) code. In this approach, a collection of true particles called macro-particles are used, and the focus is on the collective motion. Density and current are averaged over many particles, which allows collisions due to the Coulomb force to be ignored. The simulation window is divided into grids that must resolve the driving laser wavelength. The main code is a loop, shown in Figure 3.16. The charge distribution within each grid is first mapped onto the grid and is used to calculate the fields. The new velocity and position of the particles are then calculated based on these fields. This iteration continues until the maximum time for the simulation, set by the user, is reached. We have used the EPOCH and OSIRIS code for this work.

EPOCH [81] and OSIRIS [82] are both well-benchmarked relativistic electromagnetic PIC code [83, 84] which uses the finite-difference time-domain technique to numerically solve Maxwell's equations and the leap-frog method with Boris algorithm to update the velocities and positions of particles [85, 86]. They have 1, 2, and 3D simulation capability and are parallelized for efficiency.
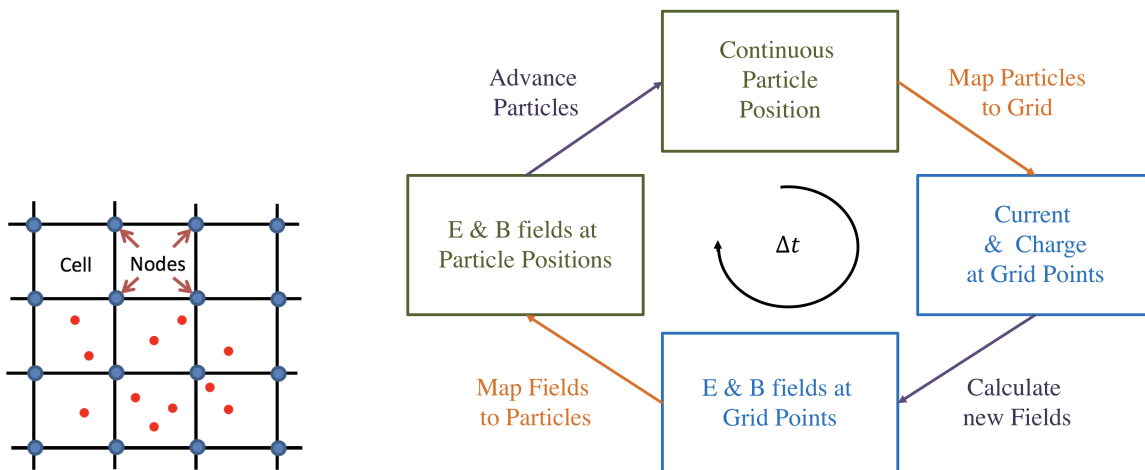
Figure 3.16: The main loop of a PIC code is shown. Initial particle position is scattered onto the grid and charge density is calculated. This is used to calculate the electric Potential (for example by the finite difference method). Electric field is then calculated and particles' velocity and position are updated according to the fields (for example by the leap frog method). Image credit: Douglass Schumacher

Chapter 4

x-ray driven wakefield acceleration in solid nanotubes

4.1 Introduction

The work presented in this chapter is motivated by the recent invention of Thin Film Compression (TFC) technique [27] for lasers, that enables compressing an ultra-intense pulse to as short as one optical cycle. This single cycle optical pulse can then interact with an overcritical surface to produce a single cycle x-ray pulse. This is known as the relativistic compression (RC) technique [28], which is based on the oscillating mirror model [29]. TFC has a few advantages for the application considered. This technique can compress a large energy pulse as high as 1 kJ to a few fs level in multiple stages. This is in contrast with the previous methods using single mode optical fibers or fused silica hollow core capillaries filled with noble gases. The latter technique is able to compress pulses on the order of a mJ. The other advantage is the fact that TFC is a very compact setup. Here, the broadening of the spectra due to SPM happens in a thin plastic medium $\sim 500\,\mu$m instead of few meters long

capillaries. Further, TFC has an overall efficiency > 50%.

As mentioned before, conventional particle acceleration technology uses excited radio frequency (RF) waves in vacuum surrounded by metal or dielectric waveguides and has an acceleration gradient limit of approximately 1 MeV/cm due to material breakdown. Thus, larger and more expensive accelerator facilities are necessary in order to obtain higher energy particle beams. It is not clear if we can afford to build these structures larger in terms of money and space. The alternative technique of LWFA, which uses plasma as the accelerating medium is capable of producing acceleration gradients three orders of magnitude higher compared to conventional accelerators since plasma does not suffer material breakdown and can sustain very large electric fields [12, 13]. More details on laser-driven plasma-based accelerators can be found in the following previously published review papers [62, 57, 58, 56]. In LWFA, the ponderomotive force of an intense laser pulse with the appropriate length moving through an under-dense plasma causes electrons to oscillate at the plasma frequency, $\omega_{pe} \propto \sqrt{n_e}$, and excites a plasma wave (plasmon) that co-moves with the laser pulse. Electrons trapped in this robust structure can acquire relativistic energies. Electron energy gain in 1D LWFA is given by:

$$\epsilon = 2a_0^2 m_e c^2 \left(\frac{n_{cr}}{n_e}\right), \tag{4.1}$$

The energy gain is proportional to the ratio of n_{cr}, critical density defined by the laser frequency, to n_e, the plasma or electron density. According to the above equation, the energy gain of particles is inversely proportional to the plasma density. Thus far, increasing the energy gain has been carried out by decreasing the plasma density [1]. However, the acceleration length is given by:

$$L_{acc} = a_0 \left(\frac{c}{\omega_{pe}}\right)\left(\frac{\omega_l}{\omega_{pe}}\right)^2 \propto \left(\frac{n_{cr}}{n_e^{3/2}}\right). \tag{4.2}$$

---

[1]There is also a limit to how low the density can be before the threshold for self-injection is reached ($\sim 10^{17}$ cm^{-3})

Hence, the acceleration length is inversely proportional to $n_e^{3/2}$ and will increase as well when n_e is decreased, an inconvenient outcome when attempting to increase the energy gain according to Eq. 4.1. Furthermore, when n_e is decreased, it is necessary to increase the laser energy as the volume occupied by the laser pulse increases proportional to the plasma skin depth, $(c/\omega_{pe})^3$ [13, 28].

Alternatively, energy gain may be achieved without decreasing the plasma density or even under the appropriate increase of density making higher acceleration gradients possible within more compact structures. This is possible by increasing n_{cr} through increasing the laser frequency. The original LWFA paper [13] assumed a laser technology that did not exist yet. A suitable x-ray source to drive a wake does not yet exist either but may be available in the future. For current optical lasers and gaseous plasmas, the typical n_{cr}/n_e ratio is 10^{21} cm$^{-3}/10^{18}$ cm$^{-3} = 10^3$. For an x-ray pulse with a wavelength of 0.1 nm and a solid density plasma, we could for example have $n_{cr}/n_e = 10^{29}$ cm$^{-3}/10^{23}$ cm$^{-3} = 10^6$, three orders of magnitude higher. This corresponds to a million times higher acceleration gradient compared to conventional accelerators and is a path towards TeV/cm accelerators.

Although x-ray acceleration had been considered before [87], the prospect for an adequate laser driver did not exist. Recently proposed technique of TFC [27] is enabling the generation of a suitable x-ray pulse by an optical laser in the single cycle regime. The RC method for conversion into the x-ray regime can then be employed [28]. This combination, if realized, enables both single cycle x-ray pulse and intense regimes. In TFC, the frequency bandwidth of the pulse is broadened by SPM inside a thin material such as plastic. The laser pulse is then compressed by chirped mirrors to its fundamental single cycle regime with nearly 10 times higher peak power. Multiple stages may be needed to achieve this. Up-conversion of this single cycle optical pulse to an x-ray pulse via compression processes in an over-critical solid target [28] provides an intense x-ray pulse. We note that single or sub-cyclic laser pulses have been realized in attosecond science (although not intense) [88, 89]. We also note that

a sub-cyclic particle accelerator has been explored [90].

These new advancements allow us to consider LWFA in the x-ray regime and with solid densities [87, 30, 34, 31]. Solid densities are under-dense for an x-ray driver and the higher density results in a higher electric field, and thus higher acceleration gradient. High energy x-ray photons can directly interact with free charged particles or electrons in the outer shells as if they are unbound or weakly bound electrons; therefore, solid materials such as dielectrics or metals can be regarded as metallic plasmas at solid densities as the intense ultra-short x-ray pulse passes through. To x-ray photons with keV energies, shallowly bound electrons in a solid material are effectively free electrons and the electron motion may be regarded as plasma-like in the timescale of the x-ray pulse (on the order of tens of attosecond) while more strongly bound electrons remain intact. Electrons oscillate a relatively small distance about their original location to produce the wakefield. If the wakefield reaches on the order of Tajima-Dawson field [13], some electrons will be freed from the atoms and will be accelerated. Furthermore, when we inject electrons into this structure in a controlled manner, the produced wakefield will accelerate the injected electrons.

In order to minimize collisions between the accelerated electrons within the wake structure and the electrons from the solid, it is suggested to use fabricated nanotubes [30]. Nanoporous alumina (or Carbon) structures can be fabricated on quartz crystals [91, 92, 93, 94]. The pore density and diameter of this highly regular pore structure can be controlled during the fabrication to match the laser parameters to produce an optimized wakefield structure. Figure 4.1 shows an example of this regular honeycomb channel structure and its dimensions [92].

Recently, Zhang et al. studied the x-ray driven WFA in a solid density nanotube and the appropriate scalings laws [32]. These simulations compared WFA driven by an x-ray pulse, $\lambda_l = 1$ nm, in a nanotube with wall density of $n_e = 5 \times 10^{24}$ cm^{-3}; with LWFA driven by an optical pulse, $\lambda_l = 1$ μm, in a nanotube with wall density of $n_e = 5 \times 10^{18}$ cm^{-3}. The
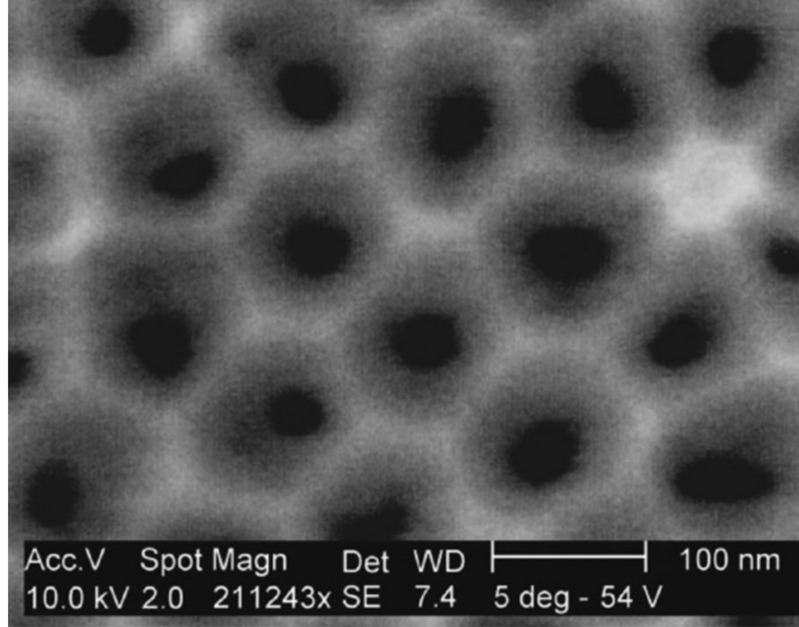
Figure 4.1: SEM image of the top surface of a porous alumina fabricated on a QCM. Image credit: Lazarowich (2007)

later case is not a physical nanotube since it has a lower density than solid material but for the purpose of a fair comparison, it was modeled as a nanotube with a central vacuum channel. In these simulations $a_0 = 10$ was kept constant. This translates to an intensity of 1.4×10^{20} W/cm^2 and 1.4×10^{26} W/cm^2 for the optical and x-ray pulse respectively. Diameter of these nanotubes were chosen to be $5 \times \lambda_l$ corresponding to 5 μm and 5 nm for the optical and x-ray case. These simulations confirmed an accelerating gradient of TeV/cm when wakefield is driven by an x-ray pulse in solid density compared to GeV/cm when it is driven by an optical pulse in gaseous material as shown in Figure 4.2. The wakefield structure is preserved as wavelength is decreased because the ratio of n_{cr}/n_e is kept fixed but the lengths are in nm instead of μm.
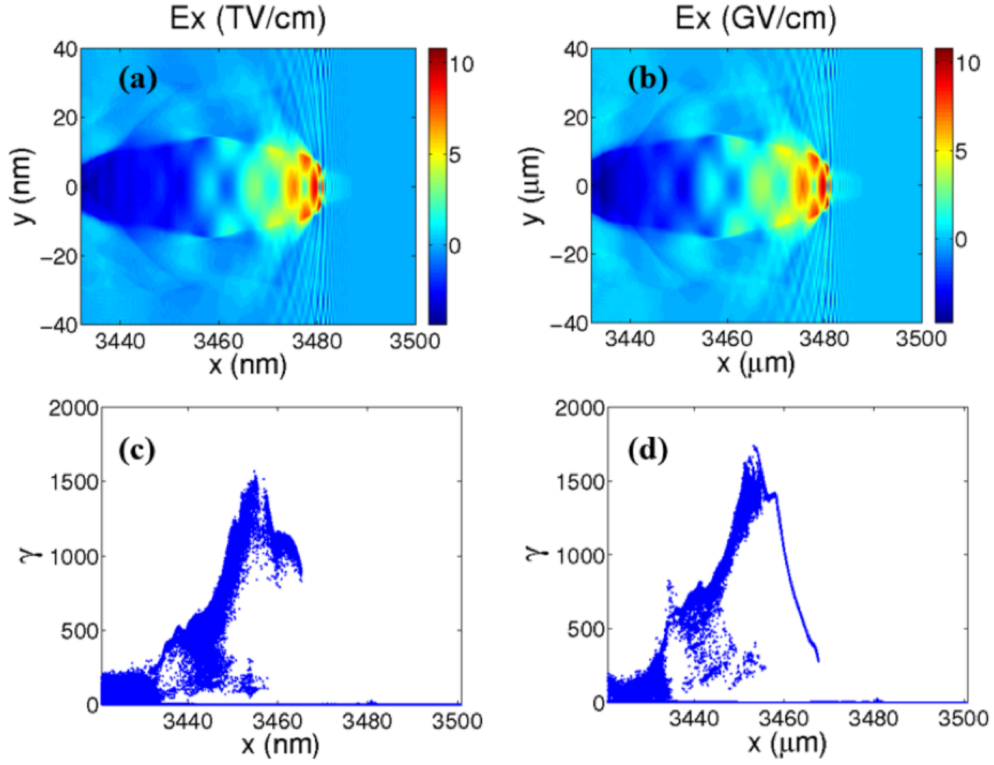
Figure 4.2: Comparison between the x-ray regime and optical regime. Distributions of (a) and (b) the longitudinal wakefield and (c) and (d) electron longitudinal momentum γv_x induced by (a) and (c) the x-ray pulse and (b) and (d) optical laser pulse in a tube when $a_0 = 10$. Image credit: Zhang (2016)

An additional set of simulations compared the x-ray, $\lambda_l = 1$ nm, driven WFA in a uniform solid density with a nanotube case modeled with a central vacuum channel and solid density walls [32]. In this case, $n_e = 5 \times 10^{24}$ cm^{-3} and $a_0 = 4$ corresponding to 2.2×10^{25} W/cm^2. Diameter of the nanotube was $5 \times \lambda_l = 5$ nm. The simulation results are shown in Figure 4.3, where the nanotube is seen to have a higher quality wake formation and the additional advantage of guiding the laser. Laser was guided for $4500 \times \lambda_l$ in the nanotube case whereas it was completely diffracted after $2000 \times \lambda_l$ in the uniform density case [32].
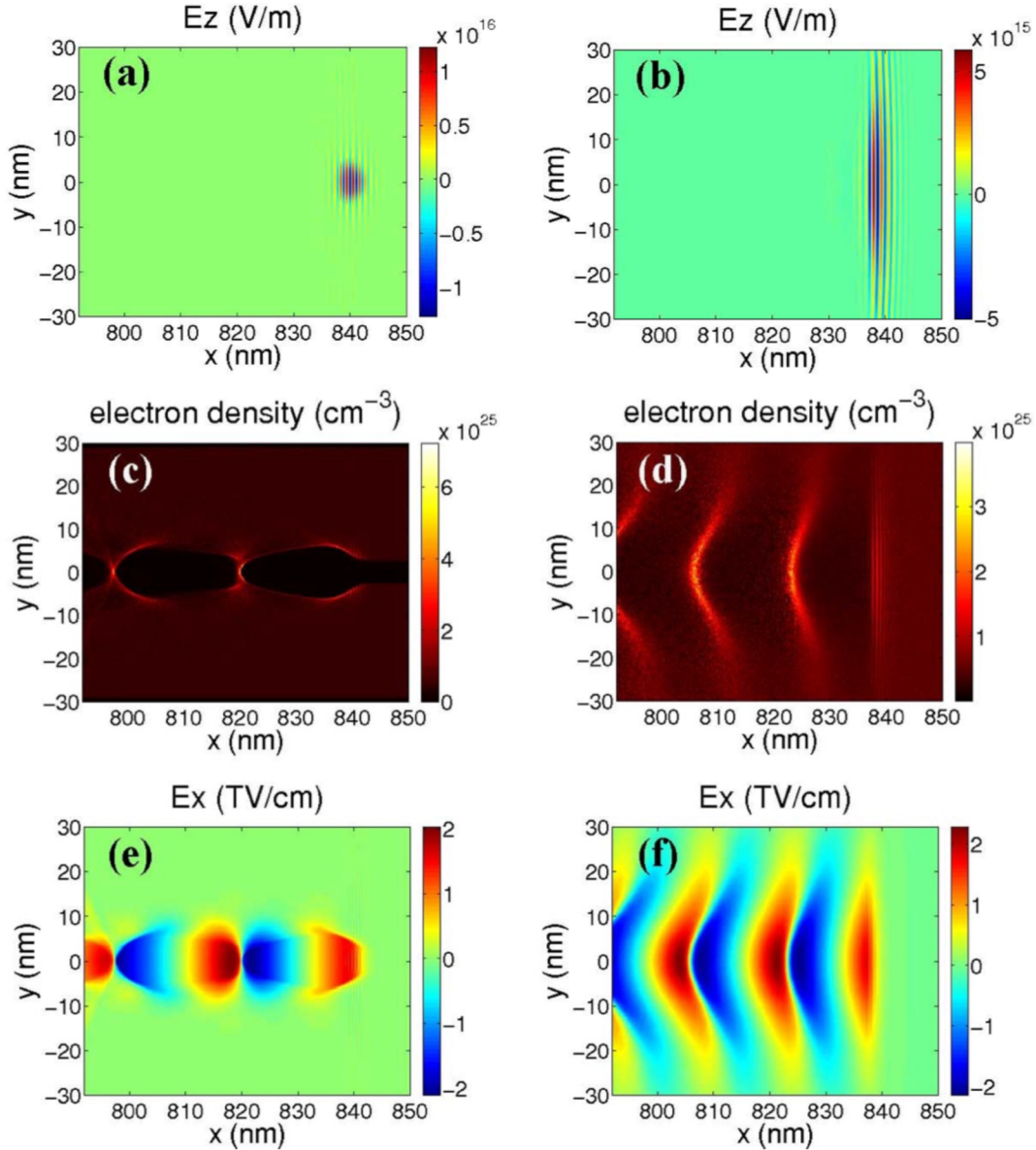
Figure 4.3: Comparison of x-ray pulse in a hollow tube versus a uniform density. Distributions of (a)(b) the laser field, (c)(d) electron density, and (e)(f) wakefield driven by an x-ray pulse when the target is a nanotube (a,c,e) or a uniform density plasma (b,d,f). Image credit: Zhang (2016)

An x-ray pulse can couple with ionic motions in solid material through optical phonon modes. In the following sections the solid state effects (polaritons) [95] are included.

A solid is composed of individual atoms. The oscillatory motion of these atoms about their

equilibrium position causes acoustical or optical lattice vibration. The present analytical model is based on the dispersion relation of the bulk system of coupled phonon-plasmon in solid state. The basic equations for this setup are the continuity and momentum equations for both species and Poissons equation:

$$\frac{\partial n_e}{\partial t} + \nabla \cdot (n_e(v_D + v_{Te})) = 0, \frac{\partial n_i}{\partial t} + \nabla \cdot (n_i v_i) = 0, \tag{4.3}$$

$$m_e n_e (\frac{\partial v_{Te}}{\partial t} + (v_D + v_{Te}) \cdot \nabla v_{Te}) = n_e q_e E - \nabla P_e, \tag{4.4}$$

$$m_i n_i (\frac{\partial v_i}{\partial t} + v_i \cdot \nabla v_i) = n_i q_i E - K_i (x_i - x_{i0}), \tag{4.5}$$

$$\nabla \cdot E = 4\pi e(n_i - n_e), \tag{4.6}$$

$$\xi_e = \frac{eE}{m_e \omega^2 - m_e k_x v_D \omega - \frac{k_x^2 \gamma T_e \omega}{\omega - k_x v_D}}, \tag{4.7}$$

$$\xi_i = \frac{-eE/m_i}{\omega^2 - \frac{K_i}{m_i}}, \tag{4.8}$$

where v_D, v_{Te} and v_i are the drift velocity of electrons, thermal velocity of electrons and ions respectively. E and P_e represent the electric field and electrons pressure and $\xi_\alpha(\alpha = e, i)$ are the displacements of charged particles. The lattice force is taken into account by addition of $K_i(x_i - x_{i0})$ term in the equation of motion for ions, where K_i is the effective spring constant. In a 1D framework, we use perturbation theory to write the equivalent 1st order equations and use Fourier theory, assuming $A = A_0 e^{i(kx - wt)}$ form for each perturbed quantity, to solve for the perturbed positions. Substituting into Poissons equation, gives the dispersion relation where $\epsilon(k, \omega)$ is the relative permittivity (setting $v_D = 0$),

$$\epsilon(k, \omega) = 1 - \frac{\omega_{pi}^2}{\omega^2 - \omega_{TO}^2} - \frac{\omega_{pe}^2}{\omega^2 - k_x^2 v_{Te}^2}. \tag{4.9}$$

Therefore, this model is capable of including the important effects of ionic motions such as the polaritons and collective modes at solid densities by including the transverse optical phonon frequency, $\omega_{TO} = \sqrt{K_i/m_i}$, in the dispersion relation [95]. In fact, this model was

previously applied to the plasmonic excitations such as plasmons and polaritons in the solid bulk as well as in the surface of these material [95, 96, 97, 98, 99] driven by a laser or an electron current. The solutions to Eq. 4.9 for a few different cases are shown in Appendix A.

In Sec. 4.2, we provide an overview of the code and the modifications to model ionic motion, we explain the initial setup and parameters of the LWFA simulations and present the results indicating no noticeable deleterious effect or instability arising from the addition of ionic lattice force. In Sec. 4.3, we use this modified code and present simulations of a current driven instability in different regimes of high and low ionic frequency having distinct behaviors. In Sec. 4.4 we discuss a few applications related to these findings and Sec. 4.5, contains concluding remarks and a discussion of extension of this work in the future.

4.2 Wakefield simulations

We investigate the WFA process driven by an x-ray source onto solid density materials. A 1D simulation is performed of a high frequency laser, which interacts with a high density plasma consisting of free electrons and a lattice of ions that feel the vibrational force from their neighbor ions. We assume an isometric lattice structure and focus on the regime where the laser pulse is within the accelerating region of the wake. We also assume that the laser spot width is far greater than the x-ray pulse length. Therefore, we can perform the simulation and analysis in 1D where the theory and scaling laws are very well known for the purpose of benchmarking and further analysis. Our first goal is to study the ionic mode in order to see if it has any affects on the wakefield formation or electron acceleration in the longitudinal direction.

4.2.1 Introduction of ionic motion at the solid density

Simulations for this work are conducted using the 1D version of the EPOCH particle-in-cell (PIC) code [81] with the second order field solver. We modify several subroutines in this code in order to manually load particles in a structured lattice and also include the effects of the lattice force [100]. Major modifications happen in EPOCH's pusher, where velocities of particles are updated, by including the second term in the following equation in order to model the lattice force,

$$\frac{dv_n}{dt}\hat{x} = \frac{q}{m}(E + v_n \times B)\hat{x} - \frac{K_i}{m}(x_n - x_{n0})\hat{x}, \tag{4.10}$$

where x_{n0} is the initial position of the particle at $t = 0$ and x_n is its position at the current iteration. This new term only affects the advancement of positive charges, and K_e is set to be zero for negative charges at all times.

Table 4.1: Summary of LWFA simulation parameters

plasma density	n_e	10^{23}	cm^{-3}
laser wavelength	λ_l	10^{-6}	cm
laser intensity	a_0	3	-
FWHM	$\lambda_{pe}/4$	2.65×10^{-6}	cm
grid size	δx	10^{-8}	cm
δt	$\delta x/0.95c$	3.5×10^{-19}	s

The initial setup is composed of ions loaded uniformly into an ordered lattice structure and of particles with negative charge loaded randomly. One positive ion is positioned exactly at the center of each cell while multiple particles with negative charge, with the appropriate charge (and mass) weight to ensure the overall charge neutrality, are distributed throughout

each cell. Plasma density is $n_i = n_e = 10^{23}$ cm^{-3} and $\omega_{pi}/\omega_{pe} = \sqrt{m_e/m_i} \approx 1/43$. Particles are interpolated to the grid using a third order b-spline shape function. The simulation domain is 1D in space ($\hat{x}$-direction) with periodic boundaries at both ends. Each cell is 1 Å in size similar to the average spacing in solids. Temperature is set to zero for both species. A Gaussian electromagnetic wave-packet, polarized in the y-direction, with a FWHM equal to $\lambda_{pe}/4$ and $a_0 = 3$ is initialized and set to propagate through the initial plasma in the $\hat{x}$-direction. The carrier frequency of the pulse is 30 PHz ($\lambda_l = 10^{-6}$ cm) corresponding to ≈ 125 eV photons. The ratio of laser frequency to plasma frequency is $\omega_l/\omega_{pe} = \sqrt{n_{cr}/n_e} = 10.5$. We collect data every $\lambda_{pe}/2c$ step until the electron energy saturation is observed. Table 4.1 provides a summary of the parameters used in the simulation.

4.2.2   x-ray driven wakefield excitation in the solid

We conduct simulations with the specified parameters for several different values of effective spring constant. The initial simulation sets $K_i = 0$ and is predicted to show a typical wakefield evolution. We benchmark the modified code by comparing the result from this run with another simulation conducted using the original code where lattice force was not yet introduced [2]. Figure 4.4 shows the results from this initial run. We are showing the laser pulse as it travels through the plasma and the wakefield structure that forms behind it (longitudinal electric field) at times $5\lambda_{pe}/c = 1.76$ fs, $9\lambda_{pe}/c = 3.17$ fs and $11.5\lambda_{pe}/c = 4.05$ fs. Phase space is also shown for both species. Electric fields E_x and E_y are normalized by the Tajima-Dawson field [13] $E_L^{cr} = m_e\omega_{pe}c/e$, momentum is normalized by m_ec and position is normalized by λ_{pe}. As the pulse moves through the plasma, it expels electrons out of its way and creates a region with positive charges; this region is approximately $\lambda_{pe}\sqrt{a_0}$ wide as seen in Fig 4.4. The excited longitudinal electric field is seen to attain amplitude on the order of E_L^{cr}, consistent with the theory. This electric field results in an accelerating gradient

---

[2]The modified code was also benchmarked with well known examples such as two stream and Buneman instability.
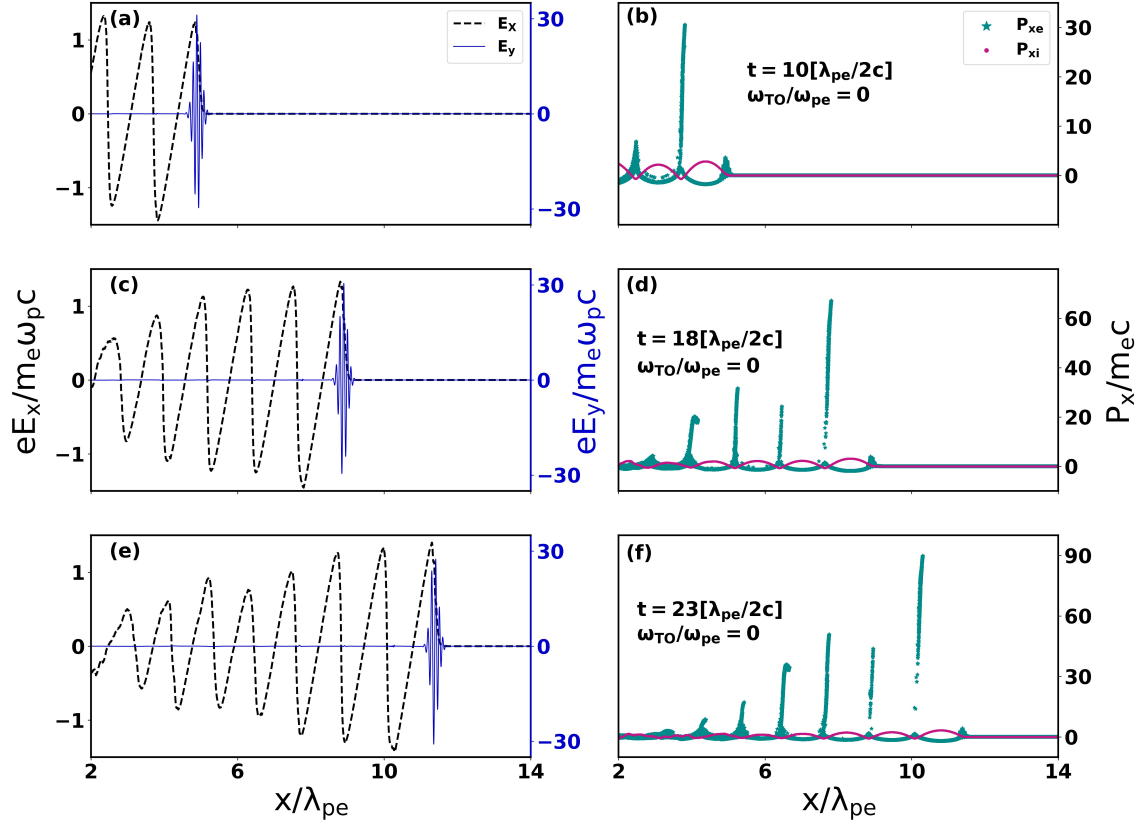
Figure 4.4: Evolution of LWFA with $\omega_{TO} = 0$ at $t/[\lambda_{pe}/2c] = 10$ (panels a and b), $t/[\lambda_{pe}/2c] = 18$ (panels c and d) and $t/[\lambda_{pe}/2c] = 23$ (panels e and f) are shown. Panels (a), (c) and (e) show electric field of the laser pulse, E_y, shown by blue solid line (right axis) and longitudinal electric field, E_x, shown by black dashed line (left axis) normalized by E_L^{cr}. Panels (b), (d) and (f) show the phase space for each species. Green stars represent simulation particles with negative charge and red dots represent simulation particles with positive charge. Momentum (right axis) is normalized by $m_e c$, and position is normalized by λ_{pe}. Image credit: Hakimi (2018)
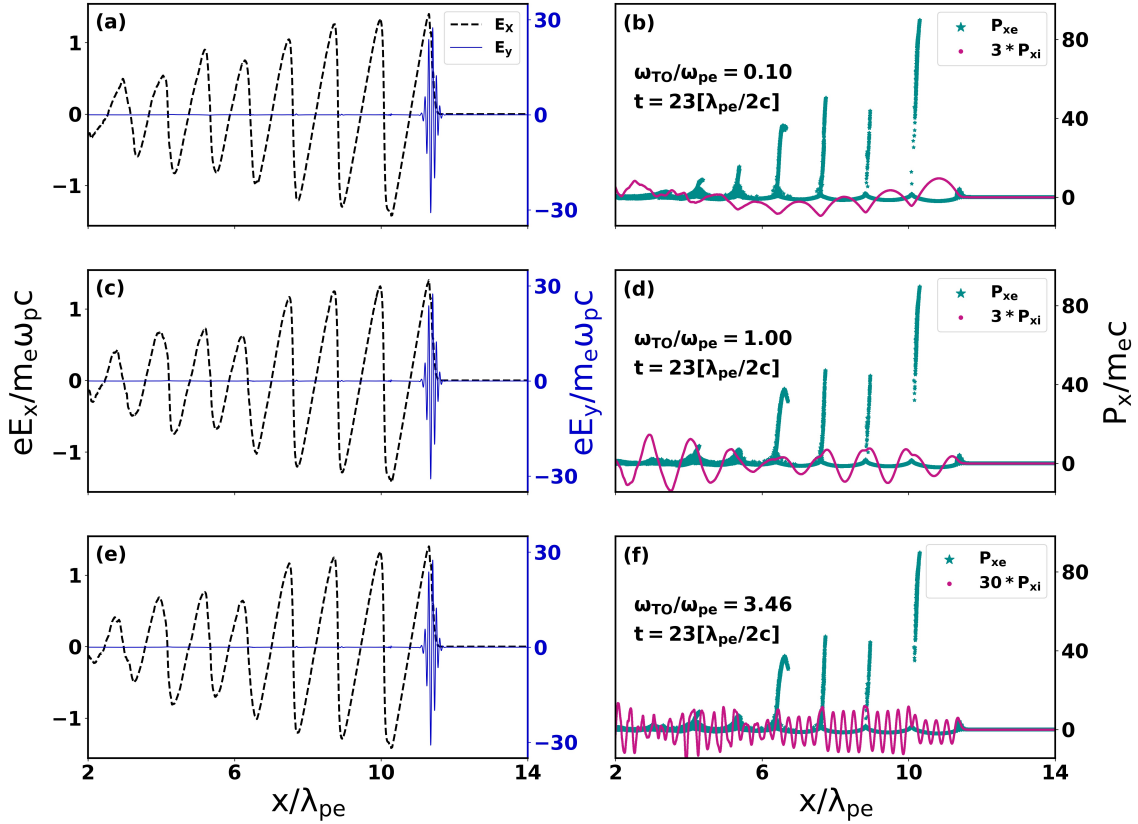
Figure 4.5: Comparison of different lattice force strengths is shown at $t/[\lambda_{pe}/2c] = 23$ for $\omega_{TO}/\omega_{pe} = 0.10$ (panels a and b), $\omega_{TO}/\omega_{pe} = 1$ (panels c and d) and $\omega_{TO}/\omega_{pe} = 3.46$ (panels e and f). Organization and normalization is the same as described in Fig. 4.4 while the amplitude of the ion mode is increased (by a factor of 3 in panels b and d and by a factor of 30 in panel f) with the intention to display it clearly. Image credit: Hakimi (2018)

of $eE_L \approx 1.4eE_L^{cr} \approx 0.4$ TeV/cm in the wakefield, which matches the theoretical prediction of $eE_L^{cr} = 0.3$ TeV/cm. It is shown that electrons at the end of each bubble continue to gain energy as the wakefield evolves and the pulse moves through the plasma. This is the limit of plasma waves (plasmon) dominated regime of the collective modes in the solid state plasma. The observed electron energy gain (even for the case of $\omega_{pe} < \omega_{TO}$, shown in Fig. 4.5(e,f)) is $\epsilon \approx 100m_ec^2 \approx 50$ MeV while the 1D LWFA theory predicts the maximum energy gain of ≈ 900 MeV. Maximum electron energy is observed to be ≈ 340 MeV in later stages of the simulation and is limited by the pump depletion length.

We then vary the strength of the lattice force by changing the effective spring constant. We calculate the value of the spring constant, K, based on the relative strength of the transverse optical phonon frequency compared to plasma frequency. For the case of $\omega_{TO}/\omega_{pe} = 0.1$, $K = 5 \times 10^6$ g/cm^2 if $m_i = 1837 \times m_e$. The value of K for Carbon atoms linked to their neighbors by covalent bonds in the diamond structure is calculated to be 1.3×10^6 g/cm^2 [100]. Table 4.2 summarizes the different ratios we use to simulate these distinct cases. Figure 4.5 shows the result of several simulations when transverse optical phonon frequency is less than, equal to, and greater than the electron plasma frequency. We are showing the result of each simulation at $t = 11.5\lambda_{pe}/c = 4.05$ fs. These figures can also be compared with Fig. 4.4(e,f), corresponding to the case of $\omega_{TO}/\omega_{pe} = 0$ at this exact time. It is observed that the wakefield or longitudinal electric field is not affected by the presence of ion modes and negative charges bunched at the end of each bubble continue to gain momentum and energy comparable to the base case with $K_i = 0$. A noticeable difference in these cases compared to the base case is the presence of an ion mode related to the lattice frequency, but the fundamentals of the LWFA is unaffected. Thus we show that the basic wakefield (plasmons excited by the mechanism of the wakefield [13]) is only slightly affected by the size of ω_{TO}/ω_{pe}. This is thus consistent with the earlier model of the wakefield formation through solid densities [32].

Further modification to the 2D EPOCH code confirms these phonon modes do not alter the electron acceleration process [101] in a wakefield as shown in Figure 4.6 for t ∼ 2 fs. In this simulation, an x-ray pulse $\lambda = 10$ nm, with $a_0 = 3$ is traveling through a uniform plasma with a density of $n_e = 10^{23}$ cm^{-3}. The ratio of $\omega_{TO}/\omega_{pe} = 3.46$ and lattice force is only acting in the x-direction (direction of propagation of laser). Figure 4.6 (c) can be compared to Figure 4.3 (e,f) to see that in both 1D and 2D cases with the addition of lattice force in x-direction, we observe TV/cm wake formation and an acceleration gradient of ∼ 0.5 TeV/cm.

Table 4.2: Different cases of LWFA simulation

Case	$\frac{\omega_{pi}}{\omega_{pe}}$	$\frac{\omega_{TO}}{\omega_{pe}}$
1	1/43	0
2	1/43	0.10
3	1/43	1
4	1/43	3.46

4.3   Simulation of beam-driven instabilities

Similar plasmons and polaritons (electron plasma waves and ionic plasma modes) can be excited in a solid plasma system with the presence of an electron current. The dispersion relations of the bulk modes with current and surface polaritons have been studied previously [95]. We confirm the existence of the bulk modes excitation via simulations using the same modified PIC code described above. More information on the theory behind these modes can be found in references such as [100, 96, 97, 98]. If we assume that electrons have a constant drift velocity and are moving through a 1D lattice of ions, Eq. 4.9 will be slightly modified
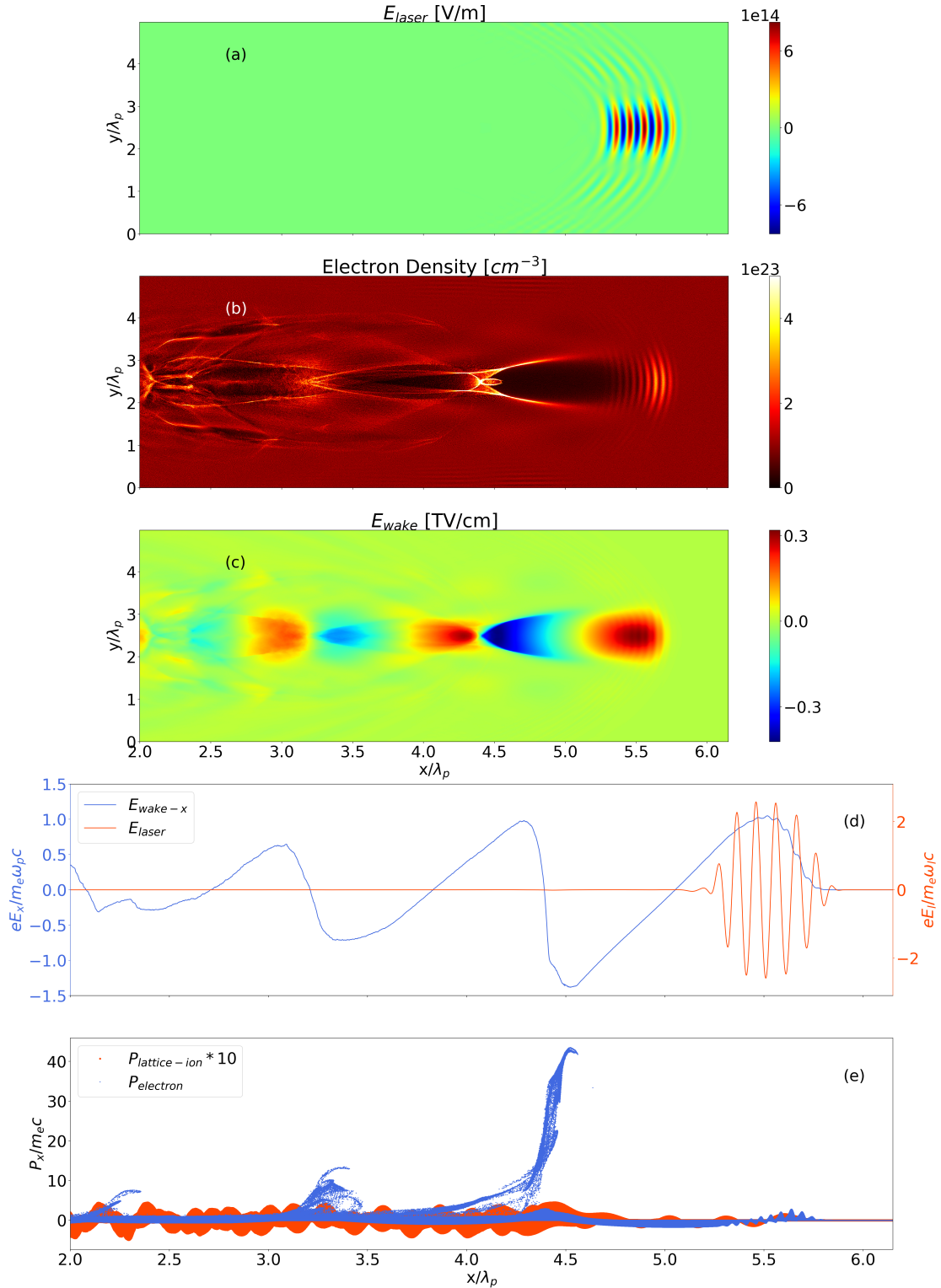
Figure 4.6: 2D LWFA simulation with lattice force turned on in the x direction, the direction of laser propagation. Here $\lambda_l = 10$ nm and $a_0 = 3$, $n_e = 10^{23}\,cm^{-3}$, $\omega_{TO}/\omega_{pe} = 3.46$. Electric field of the driving laser is shown in (a), electron density distribution is shown in (b) and wakefield is shown in (c). Lineouts of the laser and wake fields are shown in (d) and phase space for both species is shown in (e). Image credit: Hakimi (2019)

[95] to:

$$\epsilon(k, \omega) = 1 - \frac{\omega_{pi}^2}{\omega^2 - \omega_{To}^2} - \frac{\omega_{pe}^2}{(\omega - k_x v_D^2)^2 - k_x^2 v_e^2}. \tag{4.11}$$

The initial setup for the simulation is similar to the previous section. Positive ions are manually positioned at the center of each cell while negative charges are loaded randomly throughout each cell. Plasma density is slightly higher, $n_i = n_e = 10^{24} \text{cm}^{-3}$. The simulation window is 450 $\mathring{A}$ wide with 450 cells. Temperature is set to zero for both species. Electron drift velocity is varied and the case of $v_D = c/2$ is presented here. The modified code was also benchmarked against the well-known Buneman case when $K_i = 0$. Here we show simulation results from two distinct cases with different sets of parameters as summarized in Table 4.3.

Table 4.3: Different cases of beam-driven instability simulation

Case	$\frac{\omega_{pi}}{\omega_{pe}}$	$\frac{\omega_{TO}}{\omega_{pe}}$
high ionic frequency	1/2	3.46
low ionic frequency	1/63	0.11

4.3.1 High ionic frequency modes (polariton)

Equation 4.11 has four different solutions, two of which may be complex conjugate solutions with one unstable solution. In the first case we study the ratio of $\omega_{pi}/\omega_{pe} = 1/2$ and $\omega_{TO}/\omega_{pe} = 3.46$. This means that the frequency of the transverse optical phonon is much greater than that of the plasmon. This is a low density regime and polaritons are destabilized in this regime. All four solutions of the linear dispersion relation with these specified parameters are plotted in Fig. 4.7 using a polynomial solver. Real frequency versus the

70
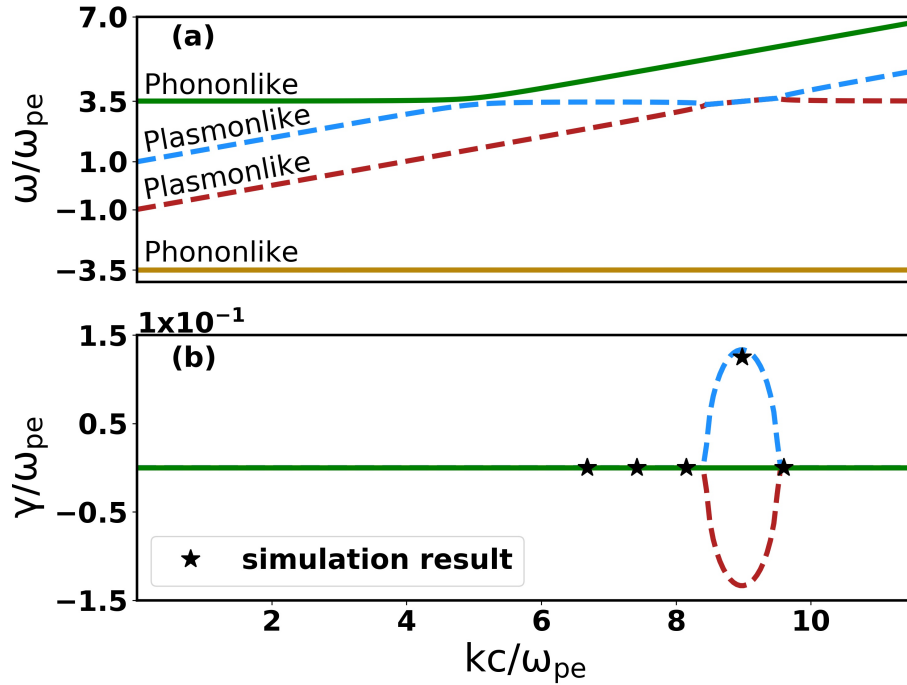
Figure 4.7: Dispersion relation of the bulk modes with current, (low density case). $\omega_{pi}/\omega_{pe} = 0.5$, $\omega_{TO}/\omega_{pe} = 3.46$, $v_D = 0.5c$. Panel (a) shows the normalized real frequency, ω/ω_{pe}, vs. normalized wavevector, kc/ω_{pe}. The top and bottom branches are phonon-like and the two middle branches are plasmon-like at lower wavevectors. The instability occurs when forward propagating phonon branch crosses the negative energy plasmon branch. Panel (b) shows the normalized growth rate, γ/ω_{pe}, vs. normalized wavevector. The stars mark the values of the growth rate found from the simulation data for several modes. Image credit: Hakimi (2018)
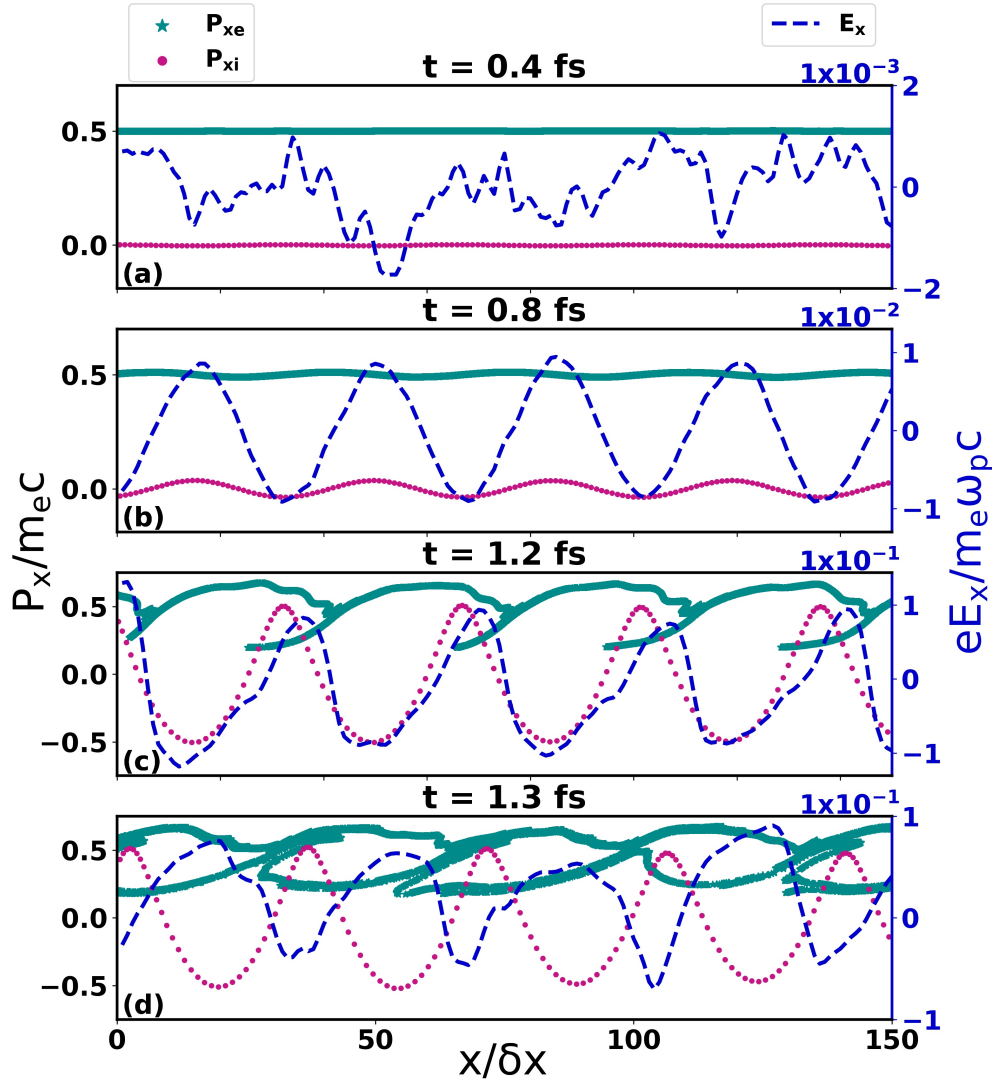
Figure 4.8: Time evolution of the unstable mode from simulation data for the case of high ionic frequency is shown. Phase space for each species is shown where momentum is normalized by $m_e c$ plotted on the left axis. Horizontal axis shows the position of particles in the simulation window normalized by the simulation grid size, $1 Å$. Green stars represent simulation particles with negative charge and red dots represent simulation particles with positive charge. The blue dashed line represent the longitudinal electric field plotted on the right axis and normalized by E_L^{cr}. Image credit: Hakimi (2018)

wavevector is shown in Fig. 4.7(a) and the growth rate versus the wavevector is shown in Fig. 4.7(b). The real frequency and growth rate are normalized by ω_{pe} and the wavevector is normalized by ω_{pe}/c. The top and bottom branches are phonon-like branches in the positive and negative frequency. The middle two branches are plasmon-like at the lower wavevector range. The instability is due to the charge bunching mechanism and occurs when the forward propagating phonon branch meets the negative energy plasmon wave [95]. The unstable wave has wavelength, $\lambda = 2\pi/k = 37 \times 10^{-8}$cm where $k = 4.46\omega_{pe}/0.5c = 8.9\omega_{pe}/c$ as seen in Fig. 4.7(a). Figure 4.8 displays the result of the simulation, studying their nonlinear behavior, with the observed wavelength of the unstable mode being 35×10^{-8} cm matching the predicted wavelength (within 5 percent). The measured growth rate for this mode matches the dispersion relation solution and is marked on Fig. 4.7(b). The growth rate is measured from the slope of the logarithm of a Fourier component of the electric field in time. We are showing the evolution of this instability and growth of this mode into a nonlinear phase. We observe that the instability picks up growing linearly, Fig. 4.8(b), and eventually is non-linearly modulated to form trapped electron orbital characteristic, Fig. 4.8(c), while ions display a more harmonic behavior throughout. In the latest nonlinear stage, Fig. 4.8(d), electrons show nearly closed trapped orbitals. The electron nonlinearities are similar to gas plasma electron dynamics (with less chaotic elements), but ions do show a more harmonic behavior. At the saturation, Fig. 4.8(c), acceleration gradient is $eE_x \sim 0.1eE_L^{cr} \approx 100\text{GeV/cm}$ at $t = 1.2$ fs.

4.3.2   Low ionic frequency modes (polariton)

In the second case we study the ratio of $\omega_{pi}/\omega_{pe} = 1/63$ and $\omega_{TO}/\omega_{pe} = 0.11$. This is a high density regime. Solutions of the dispersion relation with these parameters are plotted in Fig. 4.9. The real frequency versus the wavevector is shown in Fig. 4.9(a) and the growth rate versus the wavevector is shown in Fig. 4.9(b). Normalization is the same as
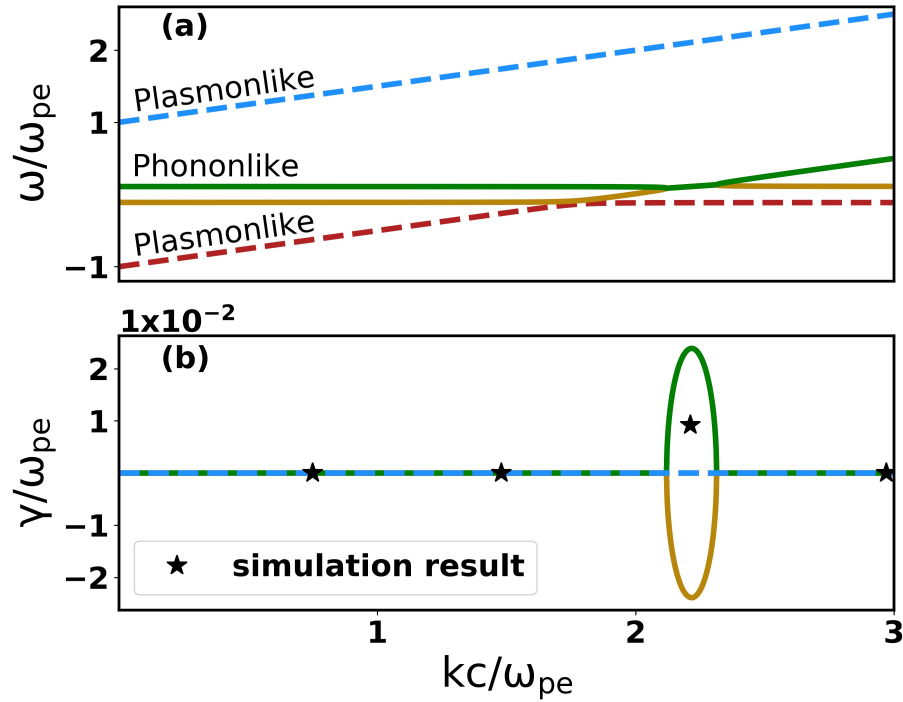
Figure 4.9: Dispersion relation of the bulk modes with current, (high density case). $\omega_{pi}/\omega_{pe} = 0.016$, $\omega_{To}/\omega_{pe} = 0.11$, $v_D = 0.5c$. Panel (a) shows the normalized real frequency, ω/ω_{pe}, vs. normalized wavevector, kc/ω_{pe}. The top and bottom branches are plasmon-like and the two middle branches are phonon-like at lower wavevectors. The instability occurs when forward propagating phonon branch crosses the negative energy plasmon branch. Panel (b) shows the normalized growth rate, γ/ω_{pe}, vs. normalized wavevector. The stars mark the values of the growth rate found from the simulation data for several modes. Image credit: Hakimi (2018)
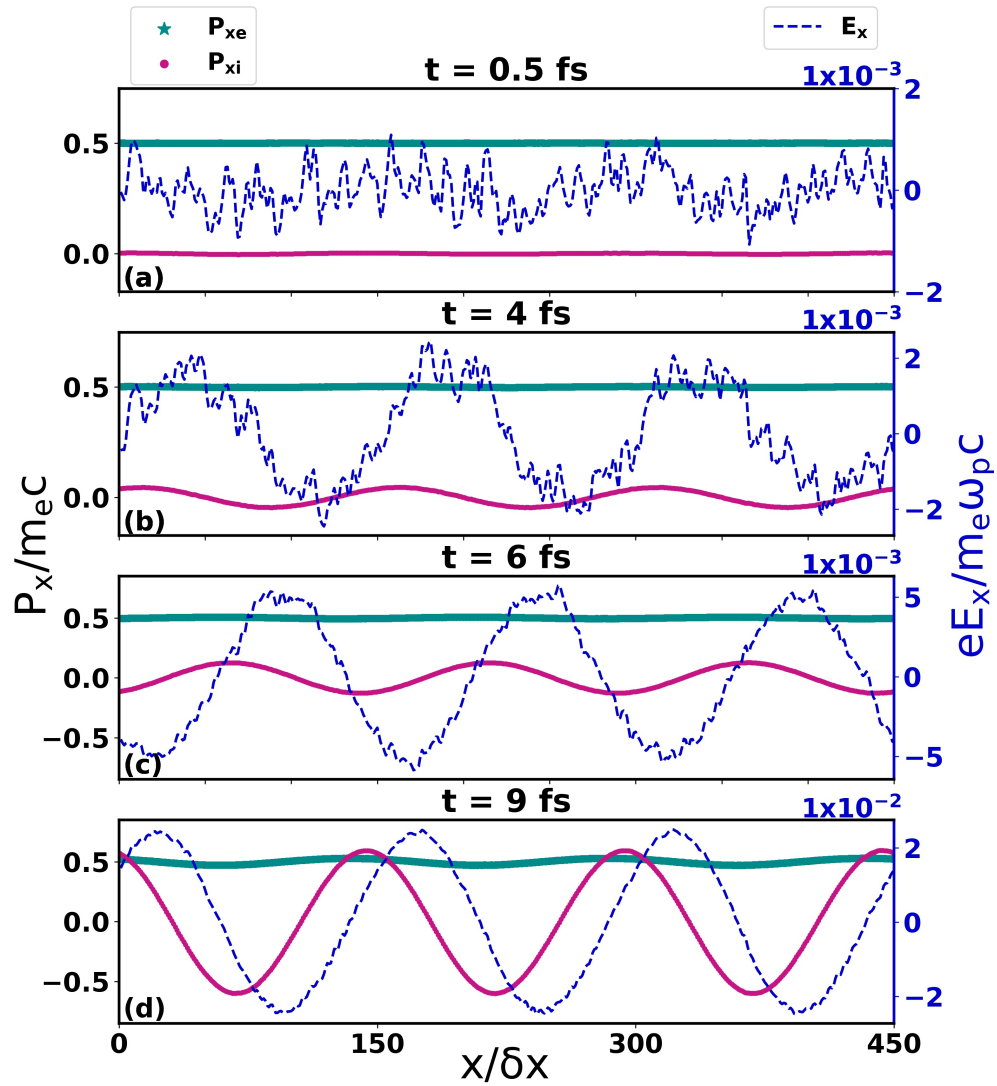
Figure 4.10: Time evolution of the unstable mode from simulation data for the case of low ionic frequency is shown. Organization and normalization is the same as described in Fig. 4.8. Image credit: Hakimi (2018)

the previous case. In these plots, the top and bottom branches are plasmon-like and the middle two branches are phonon-like at the lower wavevector range. The instability is again due to charge bunching and occurs at the crossing of the optical phonon and the negative energy plasmon branch. The unstable wave has wavelength, $\lambda = 2\pi/k = 152 \times 10^{-8}$ cm where $k = 1.1\omega_{pe}/0.5c = 2.2\omega_{pe}/c$ as seen in Fig. 4.9(a). The simulation result, Fig. 4.10, shows the observed wavelength of the unstable mode having $\lambda = 150 \times 10^{-8}$ cm matching the predicted wavelength (within 2 percent) and the measured growth rate is on the same order of magnitude as Eq. 4.11 suggests, marked on Fig. 4.9(b). We are showing the evolution of this mode; however, this instability is so weak that we observe no electron trapping phenomena similar to what has been observed in Fig. 4.8 or in the laser wakefield case, Fig. 4.4 and 4.5. Simulations for both cases were conducted with varying velocities including lower velocities, for example $v_D = 0.07c$, showing the same typical results as discussed here.

4.4   Discussion

These x-ray driven wakefield accelerators at the solid density have been considered for future high energy accelerators for electrons and perhaps ions [30, 34]. These works are further extensions of laser wakefield toward future high energy electron accelerators [102, 46, 103, 104, 105, 106, 107, 108]; however, for the application to a high energy electron accelerator [57], we suggested the adoption of nanotube materials to avoid high energy electrons scattering from the electrons in the solid [109, 110, 111]. Using solid material has the advantage of being compact and designed for controlled acceleration. Zhang, et al. have shown that the wakefield in a nanotube is reasonable for electron acceleration [32]. In fact, the nanotube wakefield is more ideal as its transverse structure is confining the laser energy and is more regulated, and subsequent betatron motions are cleaner and thus provide superior beam quality [32]. In addition, the nanotube structure is great for guiding and the repetitive

honeycomb structure of these materials such as alumina nanotubes makes it possible to raster repetitive pulse injection. It is evident that the present x-ray acceleration regime has far higher accelerating gradients than that of the dielectric x-ray acceleration [112], this is because the present x-ray can operate in the "plasma regime" (i.e. above the ionization fields).

Further, we note that the timescale of the present ultrafast x-ray pulse (nearly one-cycle regime) and its interaction with the plasmon (at the solid density) wakefield immediately following the laser pulse occurs in a matter of hundreds of attoseconds. The above field ionization and subsequent lattice movement time scales (such as potential melting) are far longer than the physics we have discussed [113]. There is also a possibility of atom stabilization due to the rapid laser oscillations [114].

The plasmon and polariton excitations in such a solid state materials by either an x-ray source or drifting electrons should be of interest to recent plasmonics applications [115, 116, 117, 118, 119]. There is also an interest to use x-ray lasers as probes to time resolve surface features in plasmonics [120, 121]. Earlier studies such as [96, 97, 98, 99] laid the foundation of these developments. Particularly, the surface excitations [95] may be applicable to these modes and their localized and controlled excitation with high intensity and ultrafast time scales. The surface wake excitation in the above nanotube is also related to the surface mode excitation and to the dielectric wakefield accelerator scheme [122, 123]. Their applications to bioinspired nanomaterials (such as nano-capillaries) [124, 125, 126, 127, 92] may also be of interest for our future investigations of excitation and monitoring of ultrafast modes in bioinspired nano-capillaries, if these modes may be signals to diagnose what is happening.

Acceleration in a crystal channel was studied previously [110], although at that time it was purely a theoretical consideration. In the light of recent realization of TFC and RC, we are reconsidering this novel regime with a technology-based new entry. In fact experimental pursuit of this route to x-ray pulse has already begun [128, 129]. Further, we can visualize

solid state fabrication technology of these nanostructures as well. We note that beam-driven solid-state tube acceleration is currently being studied as well [130].

The x-ray driven LWFA in solid nanotubes described here is a scheme for an ultra-compact accelerator with an acceleration gradient nearly 6-7 orders of magnitude larger compared to traditional accelerators. This is an improvement of 3 orders of magnitude compared to the current LWFA with gaseous targets, a route toward a "TeV on a chip". Multiple stages of this TeV/cm chip can result in an even larger energy gain in a table top accelerator. This could be an alternative and compact route to a TeV linear collider in the future. It is worthy to consider a conceptual scheme of collider path based on this concept.

It is well known that accelerated electrons in a wakefield structure oscillate in the transverse direction and produce x-ray and gamma radiation [72, 58, 131]. While electron acceleration is scaled from optical to x-ray case, the radiation generated in these different regimes are quite different as QED effects need to be considered. Photon emission is scaled with the real electric field and can be 2-3 orders of magnitude higher in the x-ray case. Previous simulations [32] show photon emission of hundreds of keV to MeV for the optical case and hundreds of MeV in the x-ray case as shown in Figure 4.11. Nanotubes with periodic characterizations (in the direction of propagation of the laser) could also serve as nano-undulators to control the produced radiation. For example, we can envision a specific superlattice period for a particular electron energy to produce a certain energy γ-photons as designed. Such a design may be employed to test the hypothesis of 17 MeV observed γ-photon to be part of the "fifth force" investigation [132, 133]. These nanostructures with additional periodicity may be possible by methods such as superlattice of nanomaterial. It should be noted that present day semiconductor technology enables the fabrication of these structures layer-by-layer as specified by design. In this case, the nanotube is doing both the electron acceleration and undulation and there is no need for a superconducting magnet or its cooling systems. Therefore, x-ray driven WFA could be a new x-ray or gamma radiation source, far more

compact in size and greater in photon energy compared to other schemes.
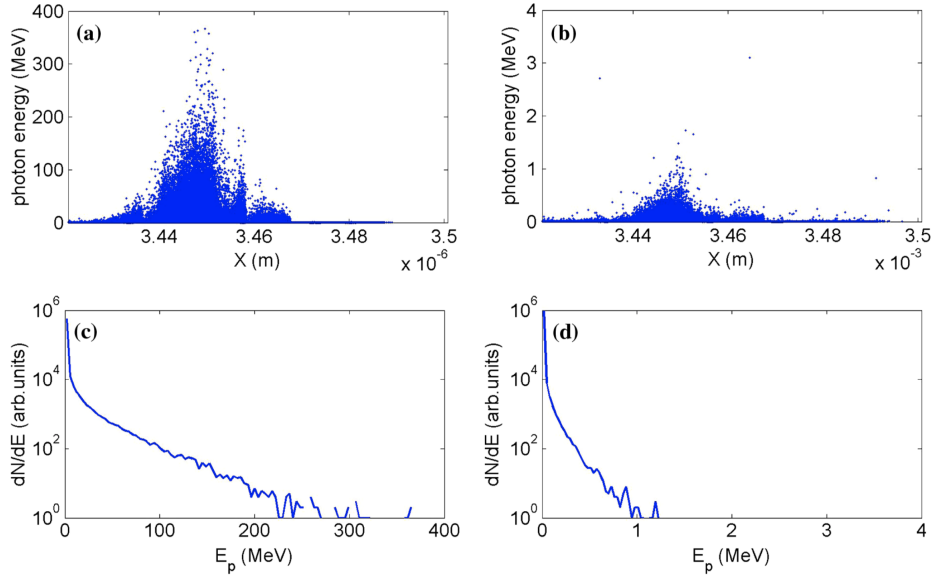
Figure 4.11: The energy spectrum and spatial distribution of photon emitted from the wakefield driven by x-ray pulse and optical one. (a) and (b) Photon energy distributions and (c) and (d) photon energy spectrum in the (a) and (c) x-ray driven case and (b) and (d) 1 eV optical laser driven case in a tube. Image credit: Zhang (2016)

It is fascinating to think about the broad range of future applications beyond the high energy physics collider and high energy x-ray FELs on a compact chip or chips. The conversion efficiency of this scheme is not yet known and requires experimental investigation in the future. Applications include: (i) the non-luminosity paradigm not resorting to the colliding beam to detect high energy physics phenomena; (ii) a candidate for muon source and acceleration [134]; (iii) Cancer radiotherapy using nanostructures as the accelerating medium [135]. For example, one of the "non-luminosity paradigm" [136, 137] has been proposed to test the texture of the vacuum in ultra high energy γ-photon. In that paper it was assumed to employ the largest energy laser available (Mega Joule lasers) for electrons to be accelerated by LWFA toward PeV. High energy (PeV) γ-photons from these electrons may be used to probe a possible deviation of photons in its ultrahigh energy limit due to the superstring theoretic prediction of the vacuum texture being stringy. Now that the present x-ray acceleration

in nanostructures allows TeV on a chip conditions, we imagine the proposed scheme may become more affordable.

4.5   Conclusion

We have carried out simulations and analysis of an x-ray pulse interacting with solid state media to elucidate the wakefield excitation process in this novel regime. This is an extension of a previous suggestion [30] and the earlier simulation [32] by explicitly including the ionic motion in these solid state materials. The present work validates the earlier work [32] by showing the central wakefield dynamics has not been altered by adding the ionic kinematics in terms of the wakefield of interest. In addition we have also investigated the collective modes associated with these ionic dynamics such as polaritons and its surface analogue modes [95], which may be excited either by a laser or by an electron current. The new laser compression technique [27] along with the relativistic laser compression technique [28] can provide a suitable x-ray source for this regime [30, 138] of wakefield acceleration [87, 109, 110, 111]. A similar concept in wakefield acceleration in nanomaterials driven by beams has also been suggested [138, 139]. We have shown that such an x-ray pulse, if realized by TFC and the RC, can in fact excite good quality wakefield and this is true even in the presence of the lattice force. Once we enter this regime, of attosecond x-ray pulse, we anticipate the discovery of the modes of the collective motion coupled with the laser. We can accordingly manipulate these modes with such a laser pulse in a novel way.

This scheme has a wealth of applications in addition to producing high energy electrons from a super compact accelerator such as muon accelerators [134] and endoscopic oncology [135]. Photon emission in this regime is in a much higher energy range [32] and could amount to a compact and specifically designed radiation sources as well.

The future high energy accelerator applications using nano-capillaries driven by an x-ray pulses may become an attractive possibility. The developments should also open up new applications to plasmonics and bioinspired nanomaterials research.

Chapter 5

Wavelength Scaling of Laser Wakefield Acceleration

5.1 Introduction

The main promise of LWFA is the reduction of size (and cost) of accelerators. This is possible since the acceleration gradient is orders of magnitude higher compared to the conventional accelerators. In LWFA, the length of the plasma (accelerating medium) is on the order of millimeters to centimeters. The majority of laser systems used for LWFA so far, have been large systems with a number of regenerative and multi-pass amplifiers. These systems take several rooms of space (not exactly aligned with the idea of a compact accelerator yet). They usually have a low repetition rate anywhere between one shot in every few hours to a few shots per minute [1]. This is because the energy delivered is on the order of tens of Joules and it takes time for the heat absorbed in the crystal to be removed. Commercial laser systems with sub-TW power have recently become available. The peak intensity of

---

[1]New PW systems such as HAPLS have higher repetition rate of up to 10 Hz.

these systems can be $> 10^{18}$ W/cm^2 when focused with a small f# focusing optic. These are tabletop systems ($\sim 2 \times 4$ ft) and can fit in a small space. These systems have milli-Joules of energy and operate at a high repetition rate[2] with nearly a perfect mode ($M^2 \sim 1.1$). Using a commercial laser systems is a more affordable[3] way to make 100s of keV to 10s of MeV energy electron beams for various applications in material science (e.g. ultrafast electron diffraction imaging requiring 50-100 keV electron beams) and medicine (e.g. medical linacs requiring 5-25 MeV energy electron beams). This could revolutionize particle accelerators overnight when a robust way to generate electron and x-ray beams with control over their parameters is demonstrated.

35 fs
7 mJ
1 kHz
$M^2 \sim 1.1$

4 ft

2 ft
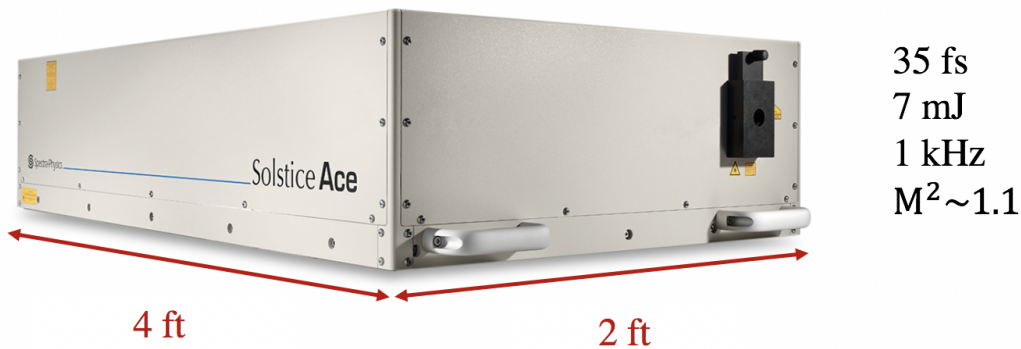
Figure 5.1: Solstice Ace High-Energy, Industrial one-box Ultrafast Amplifier produced by MKS.

Operation of a LWFA at kHz repetition rate can have several advantages such as better statistics, high signal-to-noise ratio, and improved shot-to-shot stability. The latter results from the laser operating at a thermal steady state and being more stable. The energy stability of the commercially available Solstice ACE system is less than 0.5% rms according to its specifications. This can be compared to the HERCULES laser with energy stability of 5-10% [140]. In addition, optimization of the outcome (electron or x-ray beams) is possible at

---

[2]on the order of a kHz

[3]A compact wakefield accelerator with a commercial laser system might cost about $500k, whereas a medical linac costs on the order of several millions.

kHz repetition rate via active feedback control systems [141, 142]. Furthermore, a continuous electron beam or a high flux is needed for many potential applications of LWFA, which requires the repetition rate of the pulse to be increased.

One important characteristic of these lasers is their small beam size. In CPA systems, the beam size is increased before the compression stage. For lasers with Joules of energy, the beam size is on the order of 10s of cm whereas for milli-Joule systems, it is on the order of 10s of mm. For example, the Solstice ACE system, shown in Figure 5.1, has a beam size of 10-12 mm. This enables the use of non-linear optics such as a BBO crystal[4] to produce double frequency (2ω) and triple frequency (3ω) pulses with shorter wavelengths. As mentioned in the previous chapter, simulations have shown advantages such as enhancement of betatron radiation as the laser wavelength is decreased [32]. For example, the (3ω) of an 800 nm laser generates a more intense wakefield and increases the photon energy by at least a factor of 2 [32]. Experimental verification of such phenomena as well as a thorough study of wavelength scaling (towards shorter wavelengths) of LWFA is possible with these commercial systems.

Generation of a near single cycle pulse via TFC has also been achieved [143] with the Solstice system, making a suitable x-ray pulse for WFA in a nanotube a possibility in the near future. As shown in Figure 5.2, the 35 fs output of the Solstice system was compressed to 7 fs after 2 compression stages and it could be further compressed to 4 fs with a third stage and broader bandwidth chirped mirrors [143]. The quality of the original beam was maintained with only $\sim 7\%$ drop in fluence per stage, which could be further improved with higher quality optics [143].

---

[4]The maximum size of a BBO crystal is 1 in
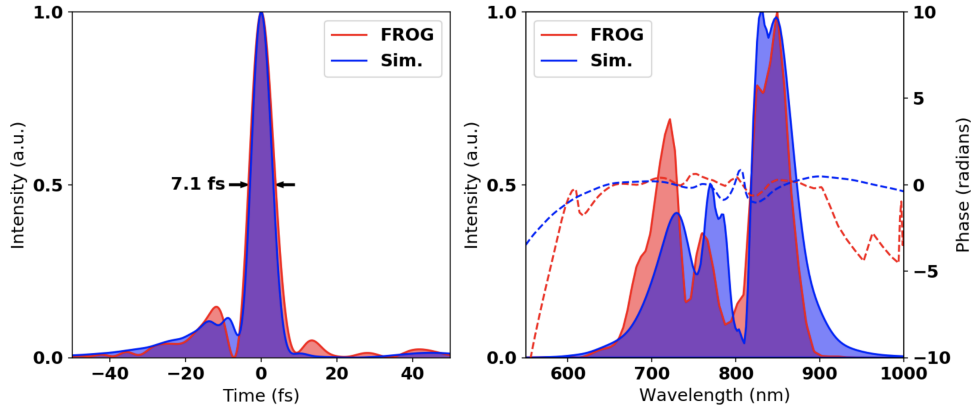
Figure 5.2: a) TG-FROG measurement after two stages of compression, with a pulse duration of 7 fs, (2-3 cycles), compared to the predicted pulse duration of 6.5 fs. b) Power spectrum and spectral phase of the reconstructed pulse. The additional phase oscillations are explained by the phase oscillations introduced by the chirped mirrors. Image credit: Stanfield (2020)

5.2 Current progress on LWFA at kHz repetition rate

Home-built mJ laser systems have already been used to demonstrate the scaling of LWFA to mJ regime [144, 145, 146, 147, 103, 148]. The energy of the produced electron beam could be 100's of keV to 10's of MeV, which is suitable for applications with moderate energy requirements such as ultrafast diffraction imaging [149] and radiolysis [150]. The original work [144, 145] in this regime (less than 10 mJ energy and kHz repetition rate) was done by rigorous parameter scanning and was followed by optimization of the electron beam by genetic algorithms [141]. Electrons were injected in the wakefield by the density down-ramp mechanism and acquired sub-relativistic energy and the beam had a low charge, $\sim$ fC. Subsequent work [146, 147] demonstrated up to 10 MeV and higher charge electron beams by using a near-critical density target in the self-modulated LWFA regime.

Another approach to increasing the electron energy from sub-relativistic to MeV range is by using short pulses of near single cycle and simultaneously increasing the plasma density [103, 148]. This is because the scaling law of the bubble regime requires that both pulse duration and plasma wavelength be decreased by a factor of 10 when the laser energy is

reduced from J to mJ scale. In this case, the wakefield can be operated close to the bubble regime and produce good quality electron beams of approximately 10 MeV. In this regime, the laser carrier envelope phase and group velocity dispersion inside the plasma become important. A review of this can be found at [151, 152].

Since mJ lasers need to be focused tightly in order to reach $> 10^{18}$ W/cm^2, the Rayleigh length is very short ($\sim 16 \, \mu$m) and for an optimized coupling of the laser and plasma, the density profile should be designed with caution. For example, ionization-induced defocusing could be detrimental if the density gradient is greater than the Rayleigh length [148]. Clever designs that offer stability and long-term operation have been studied [153].

None of the mentioned experiments were performed with a commercial laser system. Commercial systems that are capable of producing the same parameters are now available and can be used for generation of a wakefield and production of electron and x-ray beams. This chapter discusses preliminary results showing evidence of electron acceleration via detection of bremsstrahlung radiation. This was done in a brand new laboratory at UCI and with the Solstice ACE commercial laser system. Future work related to this project is briefly discussed at the end.

5.3 Simulation results

PIC simulations of the interaction show production of a low charge beam ($\sim 1 - 10 \, \text{fC}$) with a maximum energy ~ 500 keV as shown in Figure 5.3. Simulation parameters were chosen to match the experimental values with a 30 fs, 2 mJ laser pulse and a focused spot size of $2 \, \mu$m corresponding to an $a_0 = 1$. The laser pulse propagates through $\sim 200 \, \mu$m of plasma with a peak electron density of $3 - 8 \times 10^{18}$ cm^{-3}.
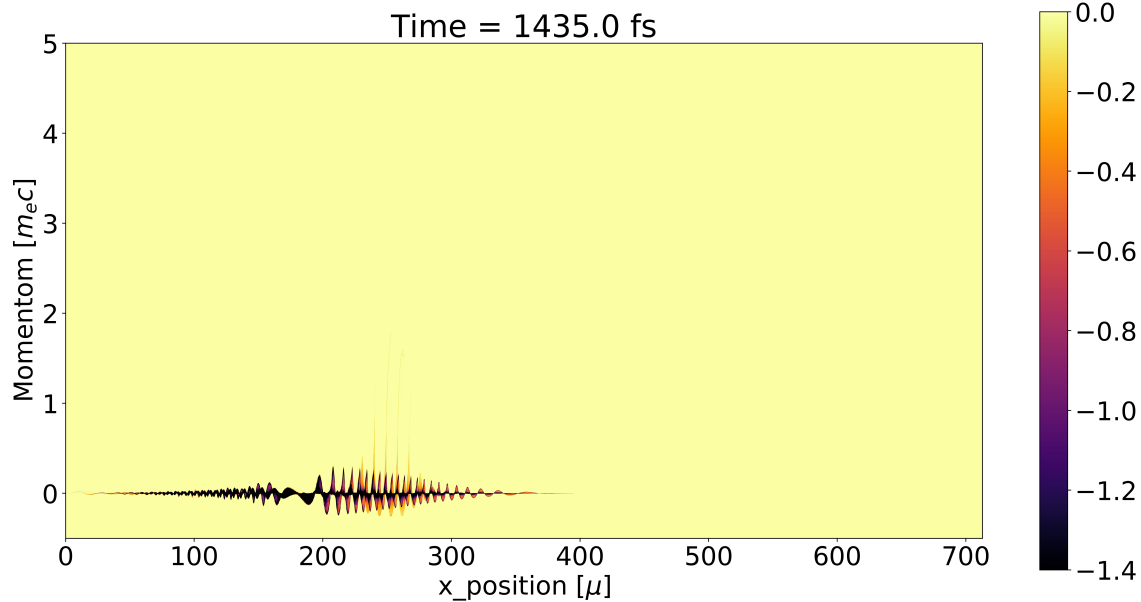
Figure 5.3: Plot of electron momentum versus position at t = 1435 fs. Peak plasma density is 8×10^{18} cm^{-3}. A small number of electrons are trapped and accelerated to ~ 500 keV.

5.3.1   Monte Carlo simulations

TOPAS MC simulation code wraps and extends the GEANT4 simulation toolkit, which is specifically used to study the passage of particles through matters for HEDP, nuclear physics, accelerator physics, space science and medical science applications. TOPAS was used to model the passage of an electron beam through the combination of an aluminum foil and the LANEX fine screen[5]. Two $2 \, \mu$m aluminum foils were used to block any residual 800 nm light from reaching the LANEX screen. Although one $2 \, \mu$m aluminum foil would be sufficient to block the laser light, two were used in order to block any existing pinhole. The LANEX fine screen is made of several layers of scintillating material, plastic substrate backing and a protective coating on either side. The exact composition and density of each layer can be found in references such as [80]. The plastic substrate backing is the thickest layer and an electron beam has to propagate through this layer before reaching the scintillating portion and producing a signal.

---

[5]This is the thinnest LANEX available for purchasing.

The geometry of the simulation is shown in Figure 5.4. The entire simulation box is a cube of $50 \times 50 \times 50$ cm and the source of the electron beam is positioned at an arbitrary surface (the left side as shown in Figure 5.4). The first foil, from left to right, is a 4 μm aluminum and the second foil is a 140 μm carbon to model the plastic substrate backing of a fine LANEX screen. The third medium is a virtual scorer. The red color is the trace of each individual electron and the green color is the trace of secondary particles, which are photons produced from electrons colliding with the material. The angular distribution of the beam was chosen to fit the simulation box and it does not match the expected electron beam parameters from the LWFA setup.

The transmission rate for a 150 keV electron beam is 12% and it decreases with the energy of the electron beam as shown in Figure 5.5. For the expected $\sim$ 100 keV electron beam, the transmission is less than 1%. This low transmission rate, in addition to quantum efficiency of the LANEX screen, collection of green emission and camera sensitivity, necessitate a more sensitive method of electron detection.

5.4   Experimental setup

The experimental setup at UCI is explained in detail in ch. 3. Here, one point of caution to note is the use of a post compression system to ensure the pulse duration is minimized at the interaction region. In contrast with other laser systems that have a larger beam diameter after the telescope in the compressor, our laser pulse has a diameter of $\sim$ 10 mm when it exits the assembly. This is a sub-TW pulse and it experiences non-linearity as it propagates through air and the glass vacuum window. For higher power laser systems, the laser beam is kept under vacuum after the final compression stage. The combination of dispersion and non-linear SPM increases the pulse duration from 35 fs exiting the laser box to $\sim$ 60 fs at the interaction region. As mentioned in ch. 3, this was corrected by adjusting the compressor
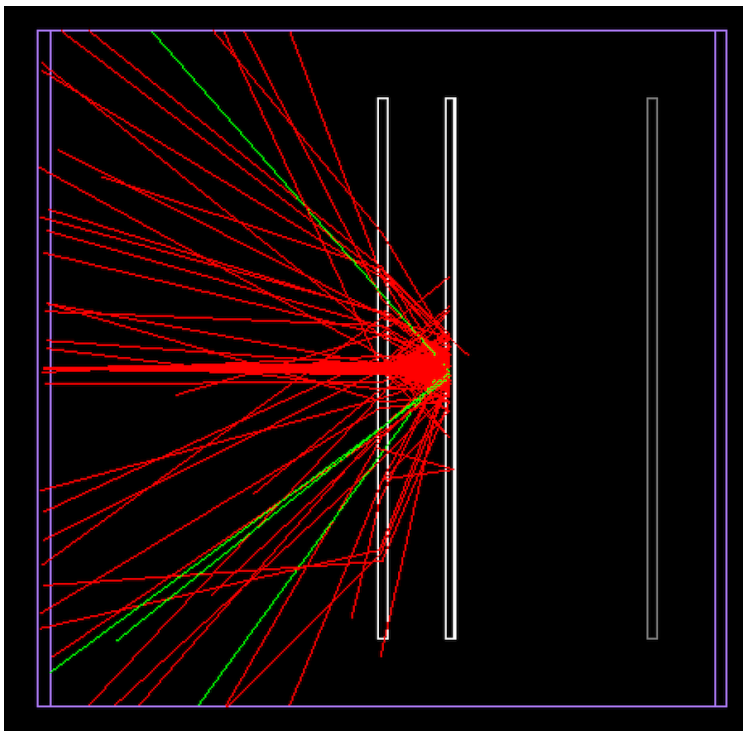
Figure 5.4: Geometry of the Monte Carlo simulation. The source is an electron beam with peak energy of 100 keV and a 10% energy spread with a total of 100 electrons. The foils are a $4\,\mu$m aluminum and a $140\,\mu$m carbon modeling the plastic backing in the LANEX. In this case none of the original electrons reach the virtual scorer positioned on the right edge of the simulation box.
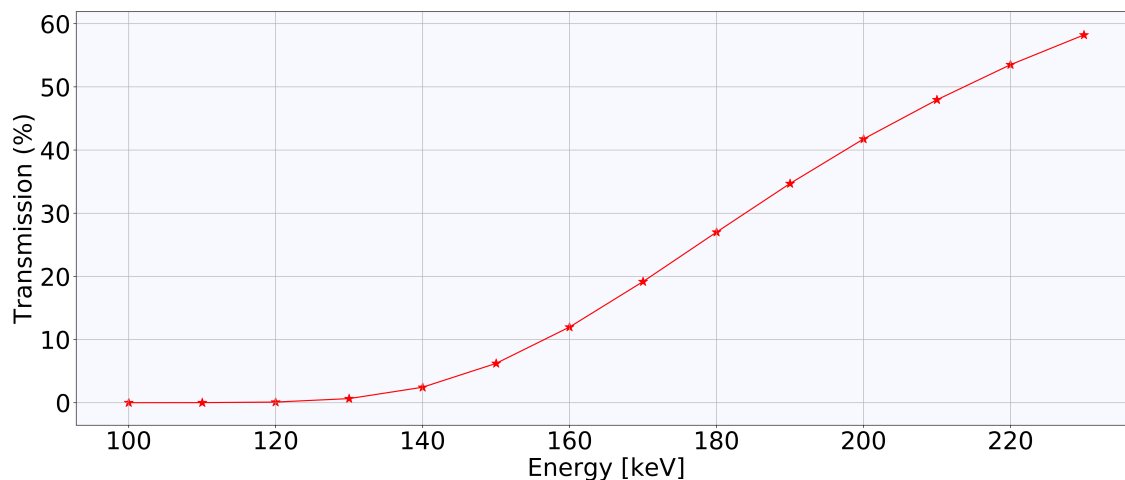
Figure 5.5: Transmission of electrons through a $4\,\mu$m aluminum filter and a fine LANEX scintillating screen, modeled as $140\,\mu$m of carbon, as a function of electron energy. The original beam has a 10% energy spread and a total of 1000000 electrons. Each point represent the result of a separate simulation with the specified peak electron energy.

setting so that the pulse leaving the laser box is positively chirped. Both the dispersion and SPM in air and the glass window add positive GVD to the laser pulse, which is later corrected inside the vacuum chamber with a pair of negative chirped mirrors. This setup produces a slightly shorter pulse duration of 30 ± 2 fs over the gas-jet due to a small spectral broadening experienced by the positively chirped pulse.

5.5 Optimization of the gas-jet location with a PIN diode

Silicon atoms in a PIN diode are connected to their neighbors by 4 electrons with covalent bonds. Atoms of a different species can be added to silicon crystal as an impurity. If for example these atoms have 5 electrons, one of the electrons is free to move and the atom left is positively charged. This is an n-type doped material because it has negative charges freely moving around. If the impurity is of a type with 3 electrons, one of the covalent bonds is broken and represents a hole that can move from atom to atom. The atom is negatively charged. This is a p-type doped material. When n and p type material are put together, a p-n junction is formed. The free electrons from the n-type material move into the p-type material and holes from p-type material move into the n-type material. This creates a neutral region in the middle, known as the intrinsic or depletion layer. The ionized atoms in the p and n type material will slowly set up an electric field that opposes the motion of electrons and holes. An external electric field can be applied to reduce or increase the internal electric field. If a positive voltage is applied at the p-type end, the electric field is reduced and free charges can move again (current will flow in this configuration). If the positive voltage is applied to the n-type end, the electric field is increased and no current will flow. This is the reverse biased configuration as shown in Figure 5.6. In a reverse biased configuration, the depletion layer is large. When energetic photons or electrons hit the PIN diode (if they have

enough energy to reach the depletion layer), they break the electron-hole pairs and current will flow. This makes a PIN diode a sensitive detector capable of producing a signal from a low current electron beam.
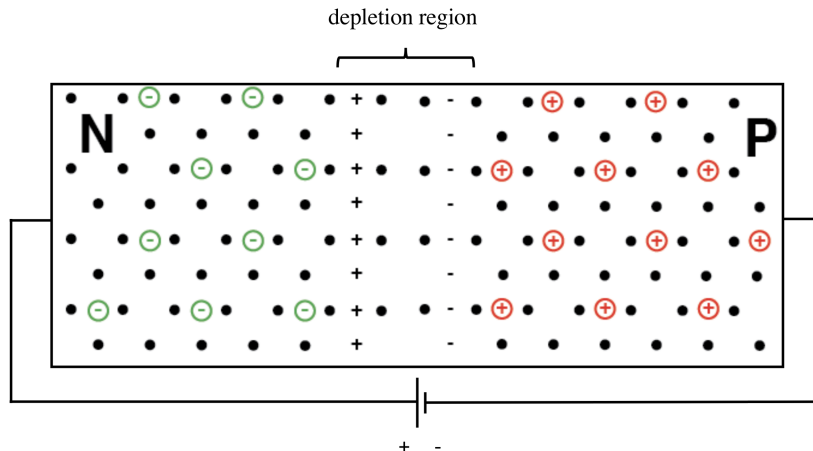
Figure 5.6: Cartoon of p-n junction diode cross section operating under reverse biased configuration showing how the intrinsic layer is formed.

The signal from PIN diode in a reverse bias configuration was used to optimize the gas-jet's location relative to the focused laser spot. To operate the PIN diode inside the vacuum chamber, a custom circuit was built with connections through a KF pin feedthrough. The circuit diagram is shown in Figure 5.7 and was based on circuit examples of OSI Optoelectronics products. The diode is biased with 32 V. An RC low-pass filter exists to clean the bias voltage. The signal from the diode is amplified by the charge sensitive pre-amplifier. We use OP913WSL PIN diode and NTE858M op-amp in this circuit. The output voltage pulse has a decay constant of $\tau = R_f C_f = 10\,\mu s$. The output voltage depends only on the charge detected and the value of C_f, as $v_{out} = -Q/C_f$ for a charge sensitive pre-amplifier. For example if 250 electrons hit the detector, a voltage reading of $0.04\,\mathrm{mV}$ should be observed. In silicon, an energy of about $3.6\,\mathrm{eV}$ is needed to free an electron-hole pair and an incident energy of $\sim 1000\,\mathrm{eV}$ is needed to free 250 electron-hole pairs. In other words the sensitivity of the entire system, $S = V_{out}/E = \frac{e}{C_f \delta}$, is $0.04\,\mathrm{mV}$ per keV of energy incident on the diode.
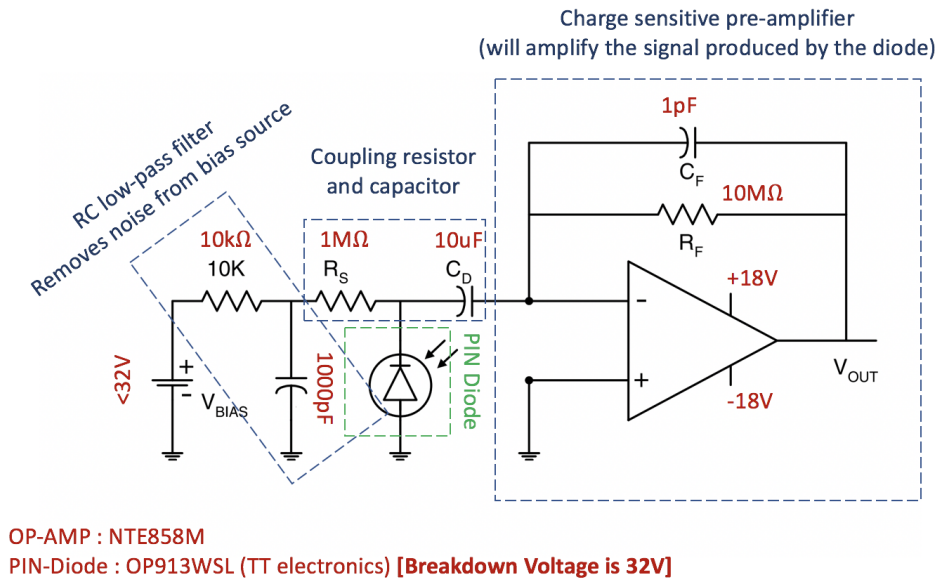
Figure 5.7: A home-built circuit with a charge sensitive pre-amplifier, operated in a reverse bias configuration for a PIN diode.

5.6 Bremsstrahlung detection as evidence for electron beam generation

The generation of an electron beam from this LWFA setup was confirmed by the detection of bremsstrahlung radiation with an Andor x-ray camera. The camera and a plot of its quantum efficiency curve is shown in Figure 5.8. An aluminum or a steel[6] puck were used as the converter of electrons into bremsstrahlung photons. This is a highly sensitive indirect electron detection method as the x-ray camera is capable of detecting a small number of photons when it is properly light shielded.

A thorough scan of relevant parameters was performed. These included the gas-jet density controlled by adjusting the backing pressure, the laser compressor setting that adjusts the compressor grating position and modifies the pulse duration, the Ascend pump laser setting,

---

[6]Higher Z material would have been more desirable but not available at the time of this experiment.
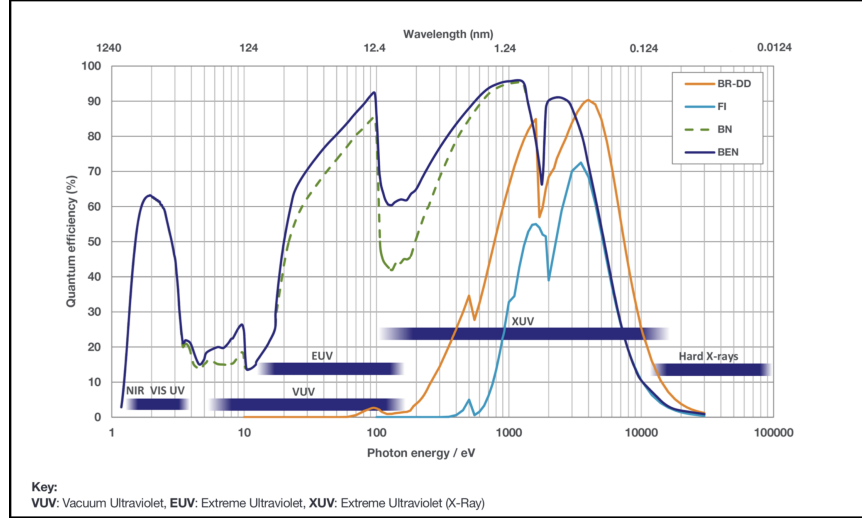
Figure 5.8: An iKon-M Andor camera was used to detect bremsstrahlung photons produced by the LWFA electron beam. The quantum efficiency of the camera is shown on the right, where the dashed green line (BN) corresponds to the camera used for this setup.

which changes the energy of the laser and the position of the gas-jet in x, y, and z directions (x and y are the transverse directions and z denotes the longitudinal direction or the direction of the laser propagation). A few example images are shown in Figure 5.9, where the density has changed. The top image corresponds to the optimized density for this setup $n_e = 6 \times 10^{18} \text{cm}^{-3}$ and the bottom image corresponds to a situation where the density is not enough to produce a wakefield. The optimized signal from the PIN diode and the x-ray camera were in agreement.

A summary of this parameter scan is shown in Figure 5.11. The counts in the vertical axis refer to the number of pixels with counts above a certain threshold averaged over 3 shots with the same conditions. The optimized density of $n_e = 6 \times 10^{18} \text{cm}^{-3}$ matches with the resonant condition, $\tau = \frac{1}{2}\lambda_p$, and previous experiments in this regime [149], where an electron beam was observed at a density range of 4-9$\times 10^{18} \text{cm}^{-3}$.

The optimized compressor setting corresponds to a pulse duration of 30 ± 2 fs, the shortest pulse duration, which was also verified by the second harmonic signal of a BBO and FROG measurements. The energy scan shows an increase in the signal as the laser energy is increased and suggests the need for higher quality focusing optic to minimize energy loss.
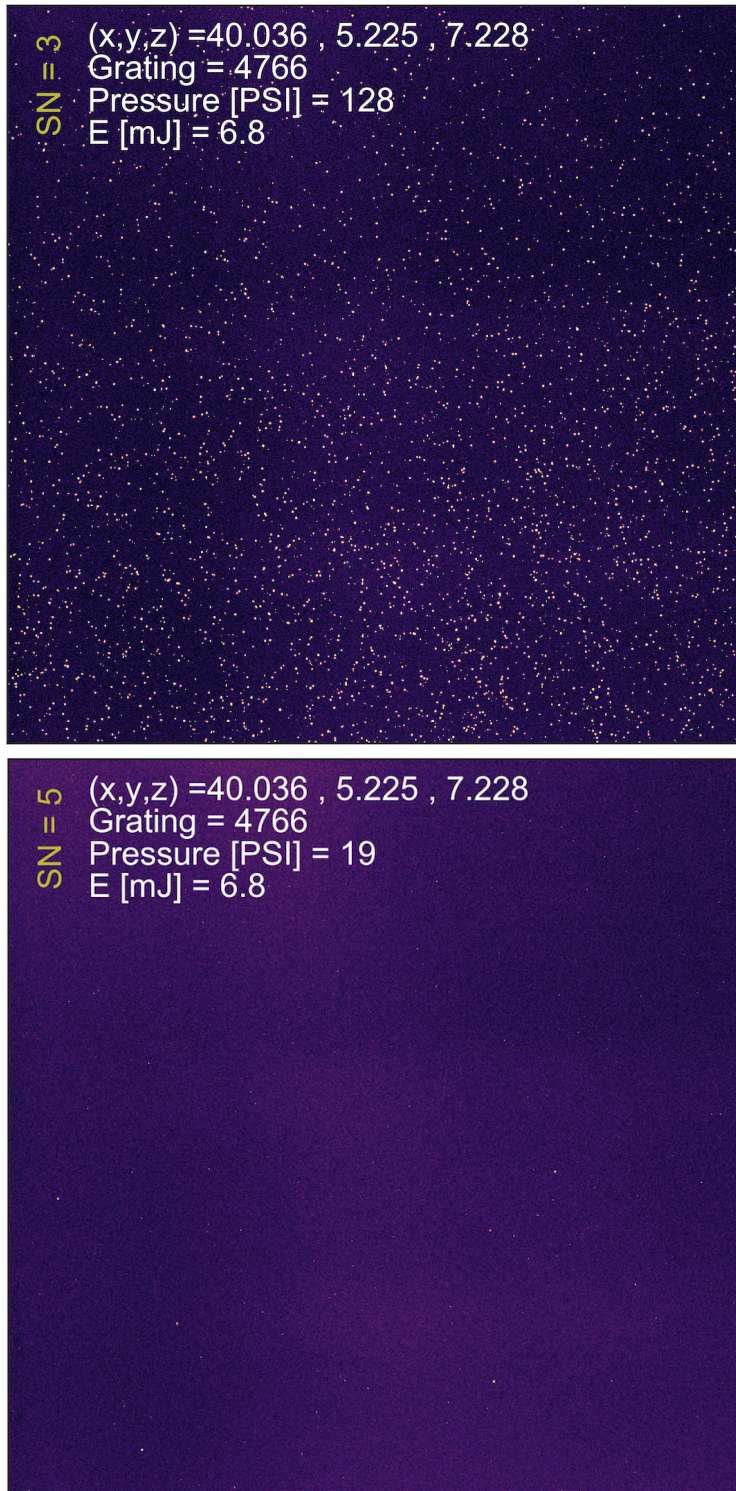
Figure 5.9: Images taken by the Andor camera during a pressure scan. The top image is from a case where density is optimized for LWFA conditions and the bottom image is from a case where plasma density is not sufficient to generate an electron beam.
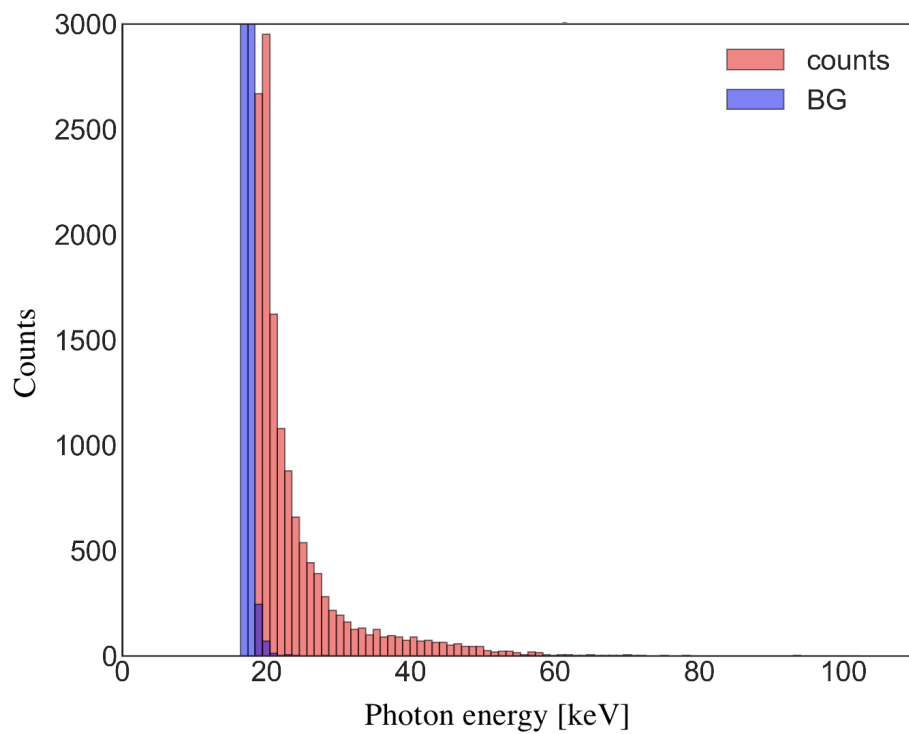
Figure 5.10: A histogram of the bremsstrahlung photon counts is shown. The x axis is 100 evenly spaced bins indicating photon energy in keV and y axis is the number of photons observed at these energies.
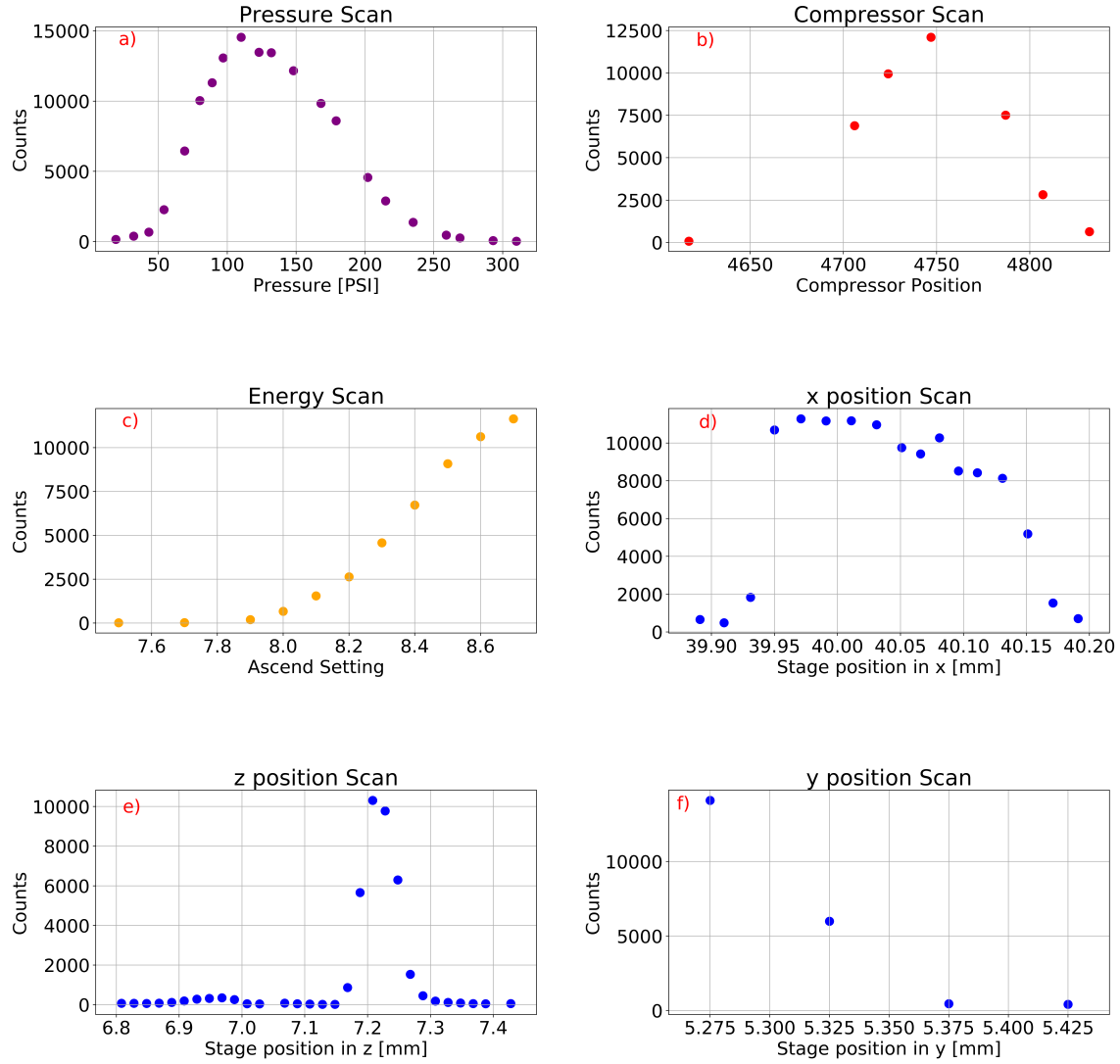
Figure 5.11: Optimization of the bremsstrahlung signal with various parameters is shown. a) Scan of backing pressure, which relates to the plasma density. The peak is at 128 PSI, corresponding to a plasma density of $6 \times 10^{18} \mathrm{W/cm^2}$. b) Scan of compressor position, relating to the pulse duration. Optimized location corresponds to the shortest pulse duration at the interaction region, which is ~ 30 fs. c) Scan of Ascend pump laser setting, relating to the pulse energy. d-f) Scan of nozzle position in 3 dimensions. Signal is optimized when the the nozzle is positioned at the down-ramp of target's Gaussian profile.

Position scan shows a narrow peak where the nozzle is positioned at the down-ramp of target's Gaussian profile. This is also in agreement with the wakefield theory and previous experiments [149]. Signal drops at a larger distance above the nozzle since the density is decreased but it is not very sensitive to the transverse position in x direction.

A histogram of the data for an optimized case is shown in Figure 5.10. The x axis is 100 evenly spaced bins indicating photon energy in keV and y axis is the number of photons observed at these energies. Photons with 20-80 keV energy were observed; however, the efficiency of the x-ray camera is less that 5% for 20-30 keV photons. The efficiency data for higher energy photons is not available. We infer that detecting any photons in this energy range means that we are producing sufficient number of these photons corresponding to electrons with 50 to 100 keV energy.

5.7 Conclusion

An experimental setup to study LWFA was designed and developed in a new lab at UCI. The driving laser is a commercial system with mJ energy and a kHz repetition rate. This regime of operation can have advantages such as shot-to-shot stability and high flux electron beams and is gaining attention in the community. The laser and target diagnostics were developed as well as electron and x-ray detectors. We were able to confirm generation of a sub-relativistic electron beam by detecting bremsstrahlung radiation in the range of 20-80 keV.

The experimental platform is developed and several studies are planned for the future. In order to improve the current setup and reduce energy loss, higher quality optics with smaller surface roughness should be used. An obstacle may be added in front of the nozzle to improve injection due to a high density gradient (shock injection) [154]. Target density

97

profile manipulation (e.g. double capillary nozzle) may be explored further in the future as well as development of small gas-cells to improve the stability of the electron beam.

The newly achieved compressed pulse of 7 fs (via two stages of TFC) with nearly 4 times higher intensity can be used for future LWFA experiments at UCI. If this compressed pulse is used with a higher density target $\sim 10^{20}\,\mathrm{cm}^{-3}$ (The highest density achieved at the lab is $6 \times 10^{19}\,\mathrm{cm}^{-3}$ and is currently limited by the maximum delivery pressure of the regulator), we could operate near the bubble regime and generate a mono-energetic electron beam with 5-10 MeV energy. Betatron radiation has not been investigated in this regime. With manipulation of the parameters, we could generate betatron radiation in the range of 1-150 eV.

This 7 fs pulse can be further compressed with a third stage of TFC to near a single cycle pulse, which can then interact with an over-critical target to produce an intense single cycle x-ray pulse. This will enable the experimental study of x-ray driven WFA in crystals and nanotubes as discussed in the previous chapter. The ultimate goal is to use an x-ray pulse; however, we can start to conduct proof of principle experiments to study the scaling laws as laser wavelength is reduced with use of a non-linear crystal to produce 400 nm and 267 nm wavelength from the current 800 nm laser pulse at UCI. Betatron generation can be enhanced with these shorter wavelengths [32]. This may be a simple way of increasing the radiation energy for various applications. For example, the above photon energy may be enhanced to ~ 300 eV, which is in the water window range and is useful for imaging organic molecules.

Chapter 6

Plasma Temperature Correlation with Electron Acceleration Processes in LWFA

6.1   Introduction

In LWFA, in the bubble regime, the ponderomotive force of the laser pushes electrons away from the regions of highest intensity and creates a bubble of positive charges called an ion cavity. Some of these electrons travel to the back of the bubble and are pulled back into it by the attractive Coulomb force of the ions. If these background electrons gain enough velocity ($\geq v_{ph}$) to slip across the electron sheet and into the bubble, they are self-injected into the accelerating part of the wakefield structure. The threshold for injection depends on the normalized vector potential of the laser and on the wake velocity [155], $v_{ph} = c\sqrt{1 - n_e/n_{cr}}$. Assuming a fixed laser wavelength, decreasing the electron plasma density increases the wake's velocity, thus making it more difficult for the electrons to be self-injected. On the other

hand, energy gain in the bubble regime is inversely proportional to the density. Lowering the self-injection threshold by a novel method is a straight forward way of achieving a higher energy gain in a single stage of a laser-plasma accelerator. Various injection schemes based on shaping the density profile [156, 157, 158, 154, 159, 160, 161], ionization [162, 163, 164], multiple laser pulses [165, 166, 167, 168, 169, 170, 171, 172, 173, 174, 175] and even magnetic field control [176] have been suggested.

Self-injected Electrons have a non-zero transverse momentum and they continue to oscillate transversely as they are longitudinally accelerated. This leads to the betatron motion of electrons and betatron radiation; thus, LWFA is also known to be a promising novel light source. The produced radiation has a high brightness and short duration [177] with a variety of applications [72] in high resolution imaging [178], radiation therapy [179, 180] and cargo scanning [181]. The critical photon energy is related to the maximum energy of electrons and is given by $E[\text{eV}] = 5.24 \times 10^{-21} \gamma_e^2 n_e [\text{cm}^{-3}] r_\beta [\mu\text{m}]$, where γ_e is the Lorentz factor for accelerated electrons, n_e is the background electron density, and r_β is the amplitude of the betatron oscillation, which can be approximated by the bubble radius, $r_b = 2\sqrt{a_0}/k_p \sim 1/\omega_p$ [43]. The wavelength at which these particles radiate is given by $\lambda = 2\pi c/\gamma_e^2 \omega_b$, where $\omega_b = \omega_{pe}/\sqrt{2\gamma_e}$ is the betatron frequency.

The hot electron temperature in the plasma can be approximated by the experimentally obtained scaling law [182, 183, 184] to be $T_e[\text{eV}] = 0.01 \times (\frac{I\lambda^2}{10^{15} \frac{\text{W}}{\text{cm}^2} \mu\text{m}^2})^{0.30 \pm 0.05}$ for $I\lambda^2 \geq 10^{15} \frac{\text{W}}{\text{cm}^2} \mu\text{m}^2$.

Presented in this chapter is a study of xuv radiation from a LWFA. Plasma conditions and signature of the bubble formation are imprinted in the xuv data and we can potentially use an xuv spectrometer to diagnose how well laser energy is coupled into the wake. We see that by increasing the density, coupling and wake formation changes. Experimental results and further simulations that discuss the influence of the laser polarization on the LWFA dynamics [185] are also discussed. The ponderomotive force responsible for generation of the

wake is polarization independent; however, the ionization dynamics and injection process is affected by the polarization of the laser pulse. The use of a circularly polarized pulse is shown to reduce the self-injection threshold by approximately 20 %. The total beam charge is enhanced by an order of magnitude due to ATI heating and the higher temperature is confirmed by the soft x-ray spectra of the plasma emission [185].

6.2 Experimental setup

These experiments were performed at the HERCULES laser facility [186, 75, 73] at the Center for Ultrafast Optical Science (CUOS) at the University of Michigan. The laser pulse with $\lambda = 800$ nm, pulse duration of 35 ± 3 fs and an average power after compression of $P_L = 50.4 \pm 5.4$ TW, where the error represents the standard uncertainty combining the uncertainties in laser energy and pulse duration, was focused onto a 3D printed gas-cell with variable length [187] filled with Helium + 3% Nitrogen to enable ionization injection [164]. The laser pulse was focused by an f/20 OAP focusing optic to a spot size of $26 \pm 0.8 \, \mu$m, at $1/e^2$ in intensity, providing a peak intensity of 6.5×10^{18} W/cm^2 at the interaction region. This intensity corresponds to a normalized laser intensity $a_0 = 1.8$ for the linearly polarized laser pulse, while a_0 is a factor of $\sqrt{2}$ smaller for circularly polarized pulse at the same intensity. To switch between linear and circular polarization, a $1/4 \, \lambda$ mica wave-plate of thickness $40 \, \mu$m was placed into the beam path before the OAP. By rotating the axis of the plate, the polarization can be switched without affecting the laser intensity and focus quality.

The plasma density was characterized using a Mach–Zehnder interferometer. The plasma density is calculated from Fourier Transforms method [188] and Abel inversion technique and can be expressed as $n_e[10^{18}$ cm$^{-3}] = 0.05 \times P[\text{PSI}] - 0.16$, where P is the backing pressure and was varied between 10 and 80 PSI.

Relativistic electrons generated from the interaction are deflected by a dipole magnet (15 cm, 0.8 T) onto a LANEX screen imaged by a CCD camera through a BG-39 bandpass filter. The dispersion of the electron spectrometer was determined by a particle tracking code using the measured magnetic field [189]. To determine the electron beam charge, the LANEX signal was calibrated by using a Fuji BAS-MS image plate [190] which gives 2.9×10^{-6} pC/count [191]. The schematic of this setup is shown in Figure 6.1.

XUV detector

Radiation produced from the interaction travels straight and into an xuv spectrometer box [192] consisting of a gold-coated concave diffraction grating and an x-ray camera. The grating is a Hitachi aperiodic 1200 l/mm flat-field concave with variable line spacing to diffract and focus the radiation onto the camera (1024×1024 pixel chip of size 25×25 mm). The detector chip is planar but the image plane is circular. This results in a spectral broadening of less than one third of a pixel for $5 < \lambda < 35$ nm . The camera can be moved to intercept the image plane at different locations in order to detect a different range of wavelengths. The gating angle can also be adjusted by a couple degrees to vary the range of wavelengths detected. The grating and associated filters are positioned in a light tight housing and the zeroth order light is blocked. This xuv spectrometer is suitable for detection of soft x-ray and ultraviolet radiation in the range of $5 - 100$ nm ($12 - 250$ eV) from a hot plasma. The resolving power of the spectrometer is approximately 1100 in the region of interest around 50 eV. Two 200 nm aluminum filters were used to block the residual 800 nm light from reaching the camera. This filter also blocks some of the xuv radiation as shown in the Figure 6.3. The desired location of the camera was calculated with the grating equation, $n\lambda = d(\sin\theta \pm \sin\theta')$, where n is an integer representing the order of diffraction, λ is the diffracted wavelength, d is the distance between slits, θ is the angle of the incoming light relative to the normal of the grating and θ' is the reflected angle. This geometry is shown in Figure 6.2.
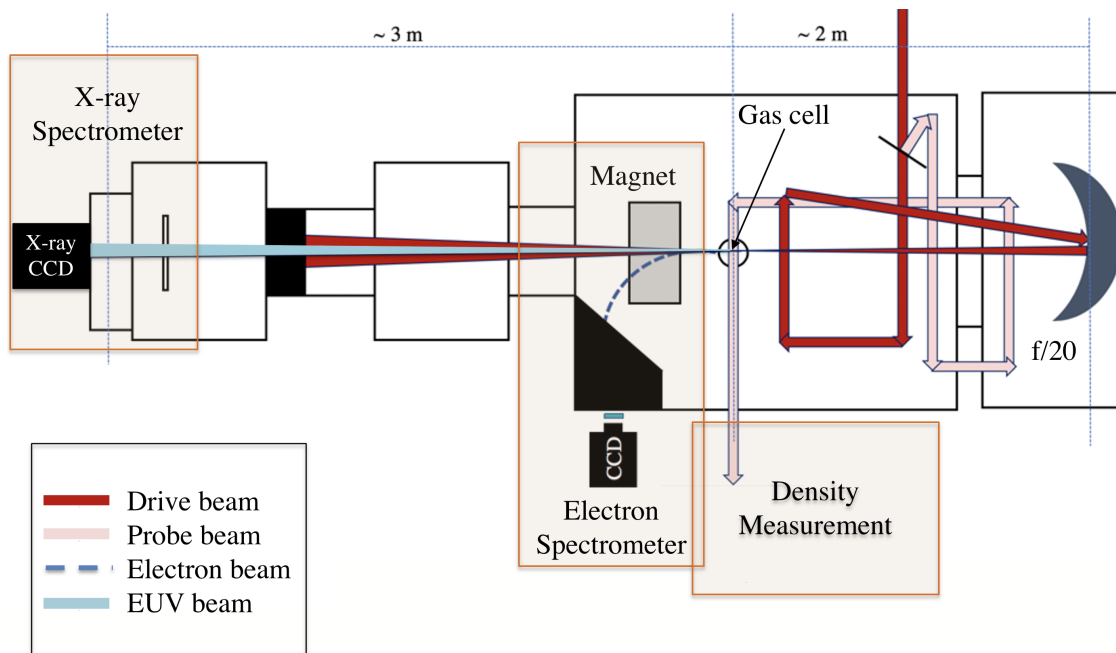
Figure 6.1: Schematic diagram of the HERCULES LWFA experimental setup. The main pulse is focused with an f/20 OAP onto a gas-cell. 4% of the main pulse is reflected from a pellicle and used to measure the density with an interferometer. Electrons are deflected toward a LANEX by a dipole magnet and the produced radiation propagates forward to an xuv spectrometer.
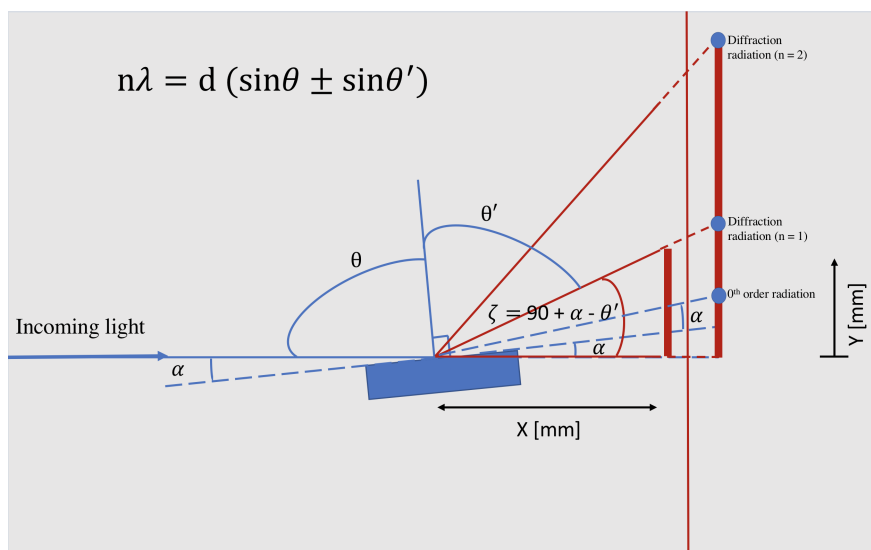
Figure 6.2: The grating equation was used to calculate the first order angle of diffraction for a range of wavelengths and determine the camera position. The grating angle, α, was set to 4 degrees. The actual image plane was circular.

Al Density=2.6989 Thickness=0.4 microns
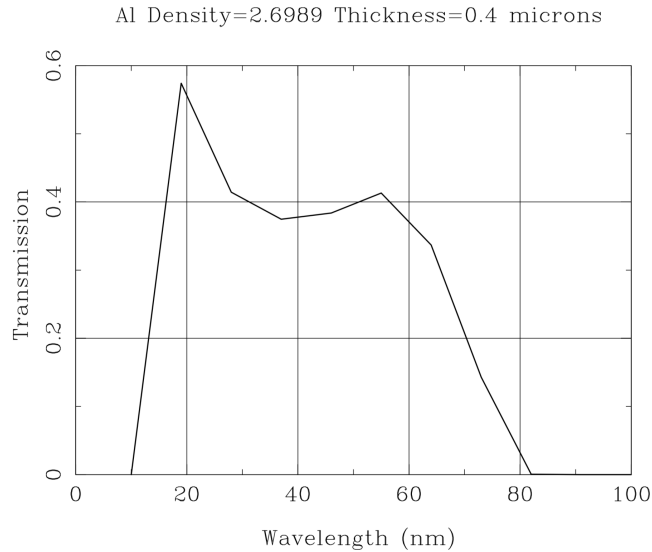
Figure 6.3: Filter transmission curve for a 400 nm aluminum filter in the wavelength range of $5 - 100$ nm from the CXRO database.

6.3   Experimental Result

After scanning various input parameters to optimize the electron beam, electron energy spectra and xuv spectra were collected as the density was varied. Xuv spectra reveals three distinct categories. Bright emission lines and a continuum are observed at the low density regime with an increase in brightness when an electron signal is present. Emission lines and a noticeable slope near $\lambda = 23$ nm are observed at the intermediate density regime. A continuum is observed at the high density regime with a correlation to the electron signal. Figure 6.4 shows examples of these xuv spectra at various densities. To identify the observed emission lines and estimate the temperature of the plasma left behind after the interaction, FLYCHK code was used to reconstruct the spectra of the target gas for a range of temperature and density values. Figure 6.5 shows a series of these simulated spectra for helium, nitrogen, carbon and oxygen. Carbon and oxygen are found in the walls of the gas-cell.

Figure 6.6 shows correlated electron and xuv spectra data from 80 shots as a function of density. The vertical bands represent a different shot where the top panel shows electron

104
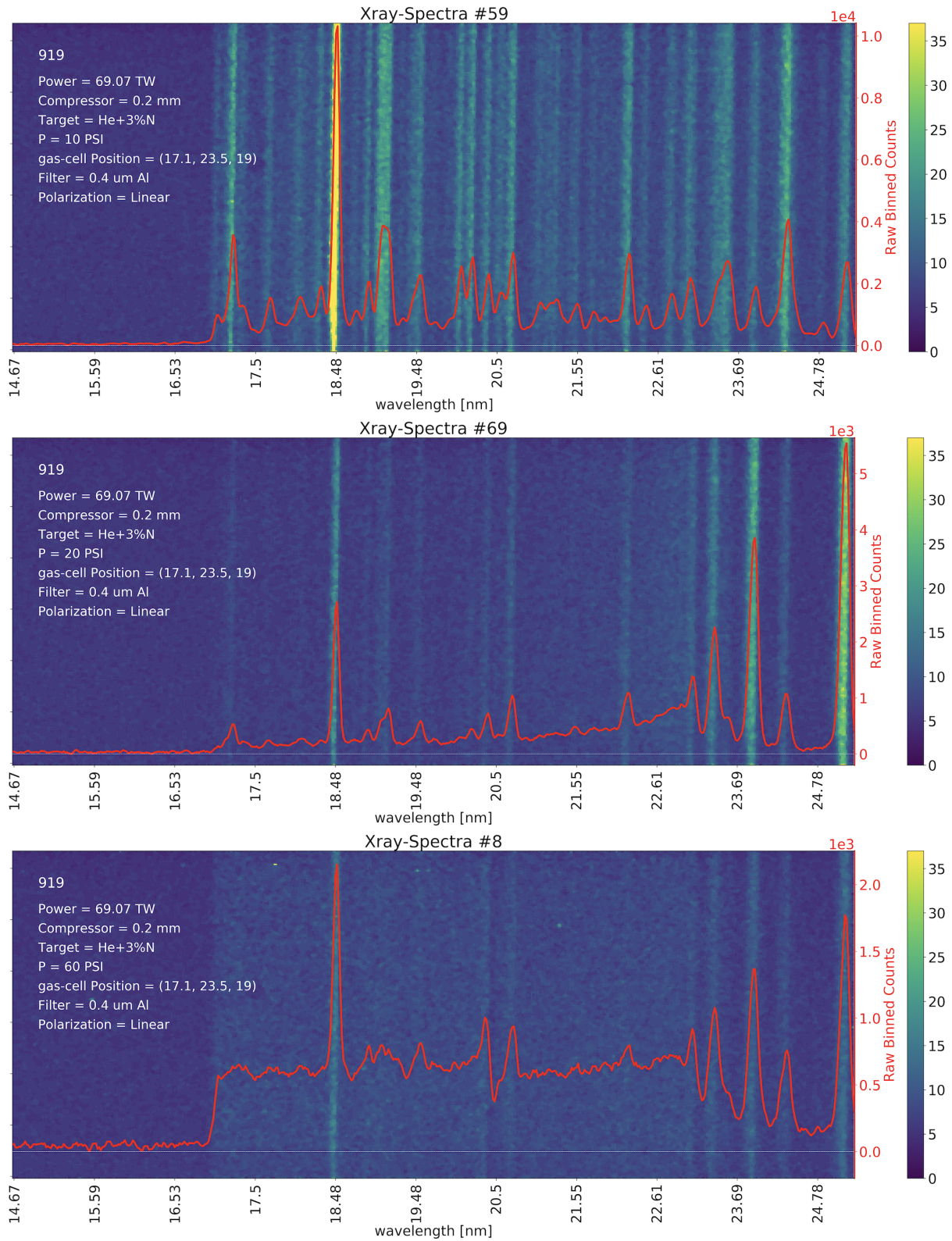
Figure 6.4: Example xuv spectra are shown at different densities of 3.4×10^{17} cm^{-3}, 8.4×10^{17} cm^{-3} and 2.8×10^{18} cm^{-3} from top to bottom. Plasma emission lines disappear and a continuum appears as density is increased. The overlying line in red is the vertically binned counts before correcting for filter, grating and camera efficiencies.
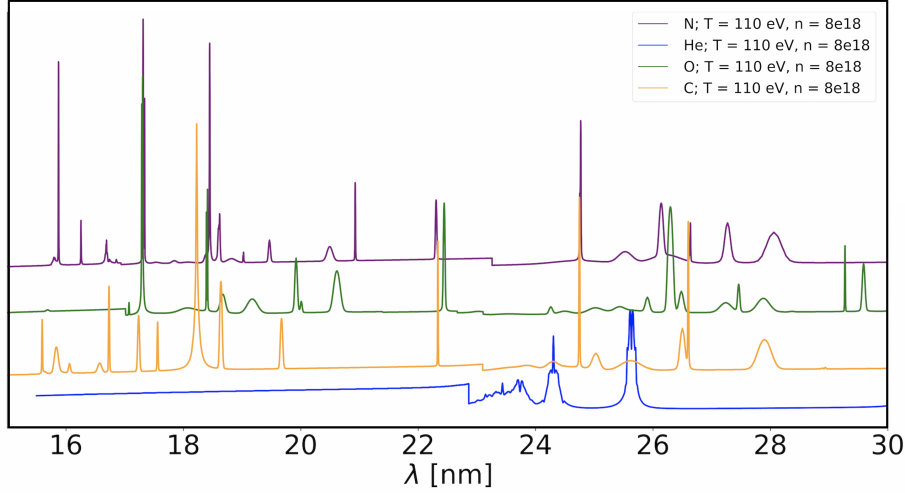
Figure 6.5: Simulated spectra of N, He, O, and C at T = 110 eV and $n = 8 \times 10^{18}$ cm^{-3} using FLYCHK. The target gas was helium with 3% added nitrogen. Carbon and oxygen are found in the walls of the gas-cell. These simulations were used to identify the observed emission lines.

spectra and bottom panel shows xuv spectra for the same shot. The density is increasing from left to right by adjusting the backing pressure. The data is separated into 3 sections of low density backed by $10 - 20$ PSI, intermediate density backed by $20 - 40$ PSI, and high density backed by $40 - 80$ PSI. The high density section corresponds to the conditions for the bubble regime where the pulse duration is less than half of the excited plasma wavelength.

As the plasma density at the interaction region is increased, a transition into the stable bubble regime is observed. Here, a stable bubble regime refers to the regime where the wakefield or the bubble is formed consistently. This is a clear, yet abrupt transition from the linear to the non-linear regime of LWFA. This transition is present in the xuv spectra, where the low density shots clearly show a different signature compared to the high density shots. The xuv spectra from the low density shots are dominated by line emission. At this density regime, only about 20% of the shots produced a measurable electron beam. These shots have xuv spectra with a higher photon count. It should be noted that the lower limit of the electron spectrometer is 40 MeV and an electron beam with lower energy

could be generated but not observed on the LANEX. At the intermediate density regime, $\sim 3.5 \times 10^{17} - 2 \times 10^{18}\,\mathrm{cm}^{-3}$, the plasma emission lines are suppressed and an electron beam is present in nearly 40% of the shots. At even higher densities, $\sim 2 - 3 \times 10^{18}\,\mathrm{cm}^{-3}$, an electron beam is consistently measured with a peak energy of $\sim 150 - 250\,\mathrm{MeV}$ and a beam charge on the order of 10s of pC. The xuv spectra shows a broad continuum from the 17 nm aluminum edge to $\lambda = 23$ nm.
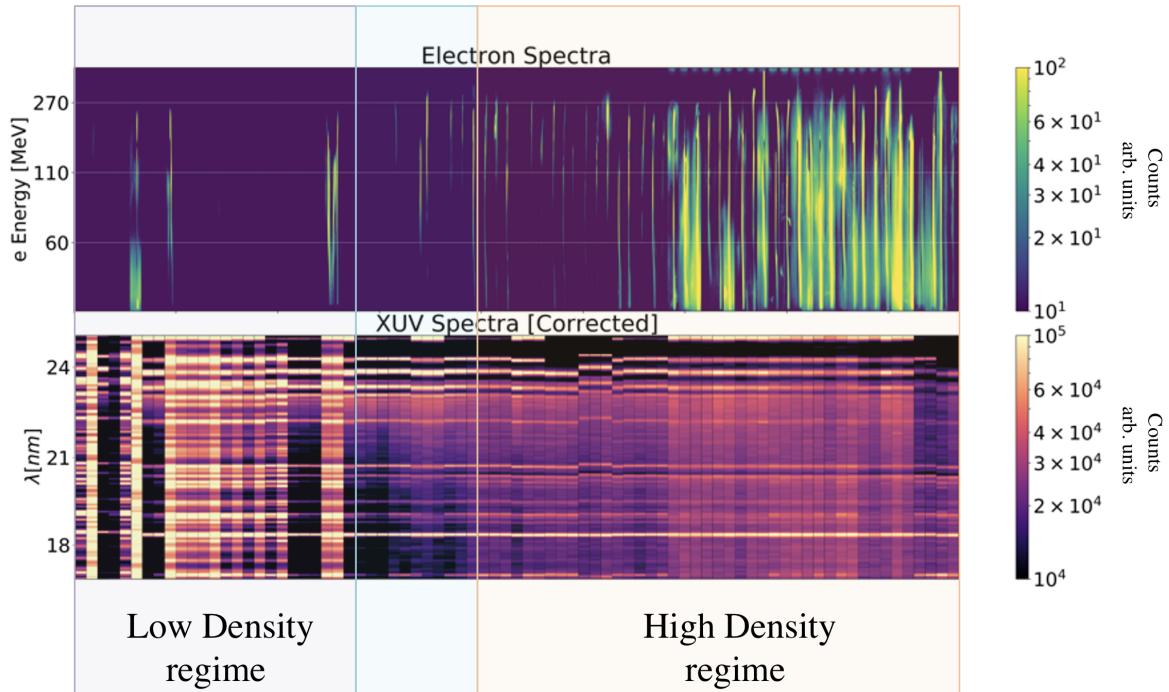
Figure 6.6: Experimental result from different shots with similar parameters is shown. The density of the target is increasing from left to right. In low density shots, the number of photons are increased when an electron beam is present. Plasma emission lines are suppressed as the density is increased. The high density regime corresponds to the bubble regime condition and produces an electron beam consistently. The xuv spectra shown is corrected with filter, grating and camera efficiencies.

6.3.1 The effect of laser polarization on the LWFA dynamics

Electron beam charge as a function of density for both cases of a linearly polarized pulse (LP) and a circularly polarized pulse (CP) at the same laser power are shown in Figure 6.7
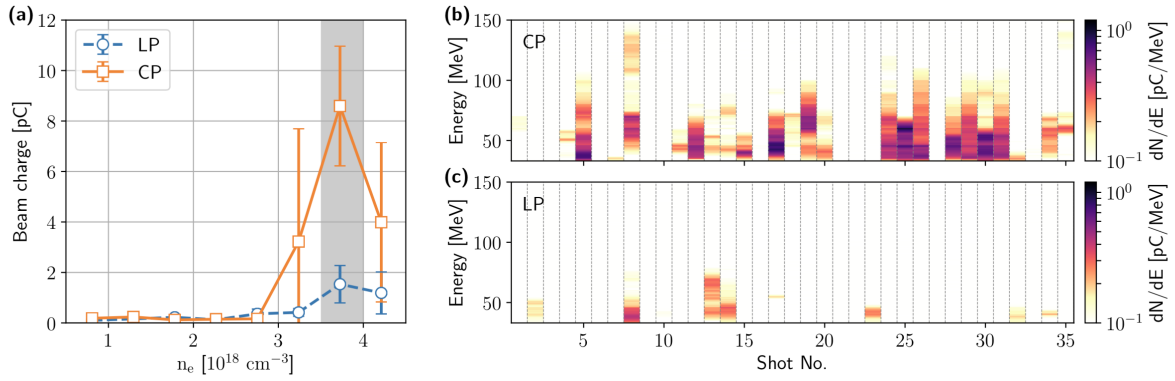
Figure 6.7: (a) Electron beam charge as a function of plasma density with LP (blue circles) and CP laser (orange squares) with the same power $P = (50.4\pm5.4)$TW. Error bars represent the 2σ uncertainty. (b),(c) Spectra of 35 consecutive shots at $n_e = (3.8 \pm 0.4) \times 10^{18}$cm^{-3} [shaded region in (a)] for CP and LP, respectively. Image Credit: Ma (2020)

a. In these shots, the target gas was pure helium. The self-injection threshold density is 3.2×10^{18} cm^3 for LP and 2.7×10^{18} cm^3 for CP. This means the threshold ratio of laser power to critical power for self-guiding, P/P_{cr}, is lowered from 5.5 for LP to 4.6 for CP, where $P_{cr} = 17.4(n_{cr}/n_p)$ [193]. The electron spectra for 35 consecutive shots with CP and LP is also shown in Figure 6.7 b,c for an electron density of $(3.8 \pm 0.4) \times 10^{18}$ cm^{-3}. A comparison of Figure 6.7 b,c shows that for a CP case, reproducibility of an electron beam, the electron beam charge and energy are higher, which suggests a dependence of trapping threshold on the polarization of the pulse.

6.4   Discussion

A clear transition from a region that does not satisfy the wakefield conditions into the stable bubble regime is seen in the xuv data. The spectra are dominated by plasma emission lines at the low density regime, indicating a lower plasma temperature, and transition into a broadband spectra. The disappearing of emission lines may indicate that electrons are freed; however, the more likely case is that because of the higher temperature and the

more efficient coupling of the laser energy into the plasma wave, electrons are excited to higher energy states and the emission lines have moved to a different wavelength range. The broadband xuv spectra at the high density range indicates the regime of bubble formation and self-injection. The intermediate density regime may correspond to the stable bubble regime where a wakefield structure capable of accelerating electrons is formed. A stable bubble formation is independent from self-injection of electrons into the bubble. An xuv spectrometer may be used as a diagnostic to identify when a stable bubble is formed. This could potentially be very useful for designing staged accelerators where the secondary stages should operate at the lowest density in order to have higher energy gain and without further injection of electrons.

There is evidence of betatron radiation generation as well. This is specially noticeable in the lower density regime as shown in Figure 6.8 where presence of an electron beam leads to a brighter xuv spectra. The reason this is not noticeable in the higher density regime could be due to the fact that higher density plasma quickly becomes opaque to radiation in this regime. At plasma density of $n_e = 2.8 \times 10^{18}\,\mathrm{cm^{-3}}$, 55-71 MeV electrons would produce betatron radiation between 24.8 and 16.9 nm (50.1-73.2 eV). Electrons of this energy range were detected as seen in Figure 6.6 at these plasma densities and it is likely that the detected continuum is betatron radiation [194]. Higher energy electrons (175-270 MeV) would produce betatron radiation in the water window range (282-533 eV). These high energy electrons were also detected; however, the xuv spectra was not aligned to detect this wavelength range.

The correlation between electron and xuv spectra shows that plasma conditions and the signature of the bubble formation are imprinted in the xuv data and an xuv spectrometer may diagnose how well the laser energy is coupled into the wake. This was shown in studying the effects of laser polarization in LWFA dynamics [185].
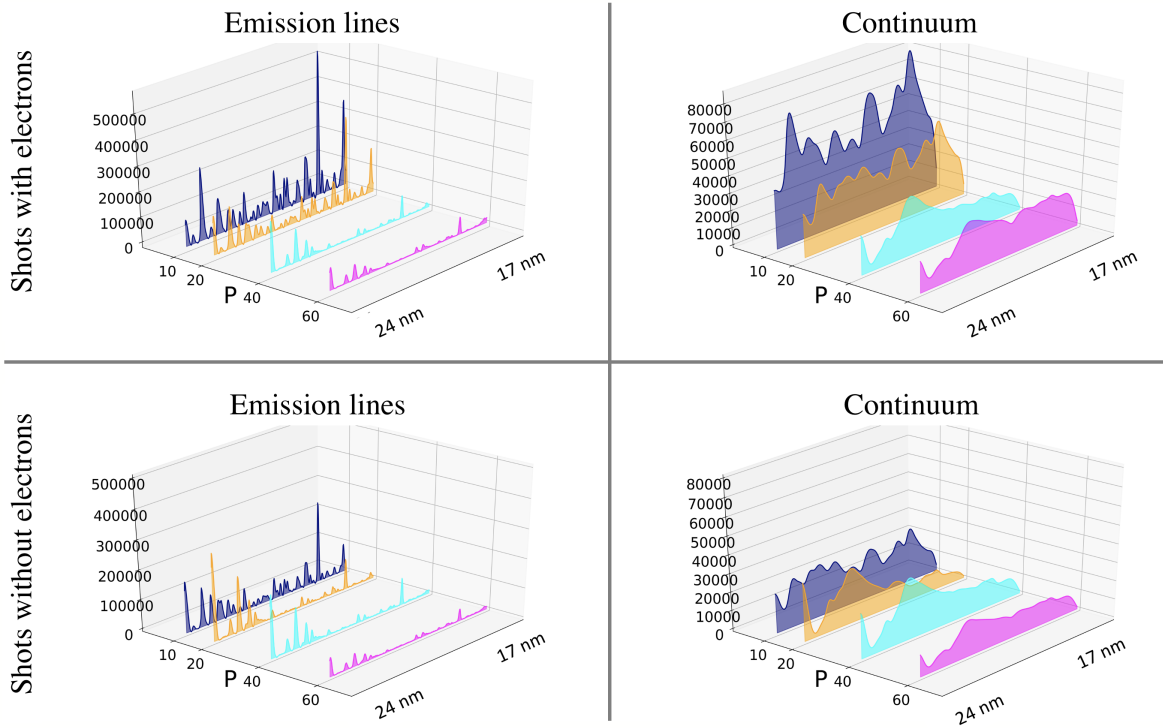
Figure 6.8: A summary of the xuv spectra is shown. The underlying continuum and the emission lines are separately plotted. The x axis is the backing pressure, which determines the target density. The y axis is the wavelength range from 17-24 nm and the z axis is the photon counts after correcting for the filter, grating and camera efficiencies. The top row shows xuv spectra from shots that generated an electron beam and the bottom row shows xuv spectra from shots that did not generate an electron beam. The xuv spectra plotted at each pressure is an average of multiple spectra from shots with the same experimental conditions. The main observations are the higher counts in the continuum when an electron beam is present, which is more noticeable at low backing pressure, and the suppression of emission lines as the backing pressure is increased.

6.4.1   Self-injection enhancement with a circularly polarized pulse

In a strong laser field, ionization happens through the ATI mechanism [195]. Electrons gain residual transverse momentum, $\boldsymbol{p}_\perp = m_e c \boldsymbol{a}_i$, as well as longitudinal momentum, $\boldsymbol{p}_\parallel = m_e c \boldsymbol{a}_i^2$, where $\boldsymbol{a}_i$ is the normalized vector potential at the moment of ionization [196, 197, 198]. This initial momentum gain at the time of ionization (before the peak pulse arrival) is the reason

for the observed difference between the LP and CP case.

Electric field and vector potential of a laser pulse, are related by $\vec{E}(\vec{x}, t) = -\frac{\partial \vec{A}(\vec{x}, t)}{\partial t}$. The electric field for an LP and CP laser propagating in the z direction can be written as:

$$\vec{E}(\vec{x}, t)_{LP} = E_0(z) cos(kz - \omega t)\hat{y}, \tag{6.1}$$

$$\vec{E}(\vec{x}, t)_{CP} = E_0(z)[\frac{1}{2}cos(kz - \omega t)\hat{x} + \frac{1}{2}sin(kz - \omega t)\hat{y}], \tag{6.2}$$

producing the following vector potential for LP and CP lasers:

$$\vec{A}(\vec{x}, t)_{LP} = \frac{E_0(z)}{\omega}sin(kz - \omega t)\hat{y}, \tag{6.3}$$

$$\vec{A}(\vec{x}, t)_{CP} = \frac{E_0(z)}{\omega}[\frac{1}{2}sin(kz - \omega t)\hat{x} - \frac{1}{2}cos(kz - \omega t)\hat{y}], \tag{6.4}$$

In the LP case, ionization dominantly happens when the electric field is at or near the maximum. At this time, the normalized vector potential is nearly zero, which leads to vanishing residual momentum and energy at the time of ionization for the LP case. In contrast, for the CP case, the amplitude of the electric field is constant and follows the pulse envelope with components in both x and y directions. The electric field continuously ionizes the neutral target gas and the magnitude of the normalized vector potential is non-vanishing, leading to a significant momentum and energy gain at the time of ionization in the CP case. A simplified plot showing the relation between $\vec{E}$ and $\vec{A}$ for both LP and CP cases is shown in Figure 6.9 leading to a difference in the initial momentum and energy gain of electrons.

Electrons that are freed by ATI at the front of the laser pulse, flow along the bubble sheet. If the longitudinal velocity of an electron near the back of the wakefield structure is larger than the phase velocity of the wake, it can be trapped and accelerated by the wakefield. The small initial transverse momentum from ATI can slightly alter the trajectories of electrons around the bubble sheath and introduce an asymmetry to their orbits. Some electrons, which
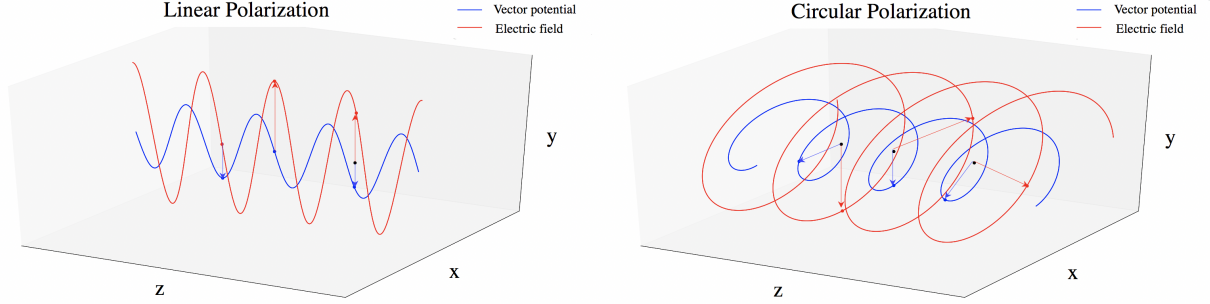
Figure 6.9: The $\vec{E}$ and $\vec{A}$ for both LP and CP cases are shown. In the LP case, when the electric field is at a maximum, $\vec{A} = 0$. Electrons are ionized with vanishing momentum gain. In the CP case, $\vec{E}$ follows the pulse envelope and $\vec{A} \neq 0$ and electrons are ionized with a non-vanishing initial momentum gain.

start at the correct azimuthal angle where the laser vector potential points inward, will be trapped more easily [185].

The initial position of trapped electrons was studied with 3D PIC simulations [185] shown in Figure 6.10 a. In the CP case, trapped electrons originate from a spiral structure at the evolving ionization front and the projection in the transverse plane is a ring with a width of approximately 1 μm. In the LP case, trapped electrons originate from only two specific angles in the polarization plane. Figure 6.10 b shows at a certain time, the initial positions of the trapped electrons are all located within a small azimuthal angle where the vector potential points toward the axis.

The difference of the residual momenta, and hence kinetic energies with different laser polarization, will eventually lead to higher plasma temperatures for CP [199, 200]. Measurements of the time-integrated xuv spectra, shown in Figure 6.11 a, and atomic physics simulations with the code SCRAM [201], shown in Figure 6.11 b, confirm higher plasma temperature by increased emission in CP case. The SCRAM calculations used a thermal plasma that was allowed to cool by radiative emission, with the initial temperature corresponding to the same average energy per electron as the LP and CP distributions. The decrease of measured emission as the gas pressure increases is thought to be due to the reduced transmission of
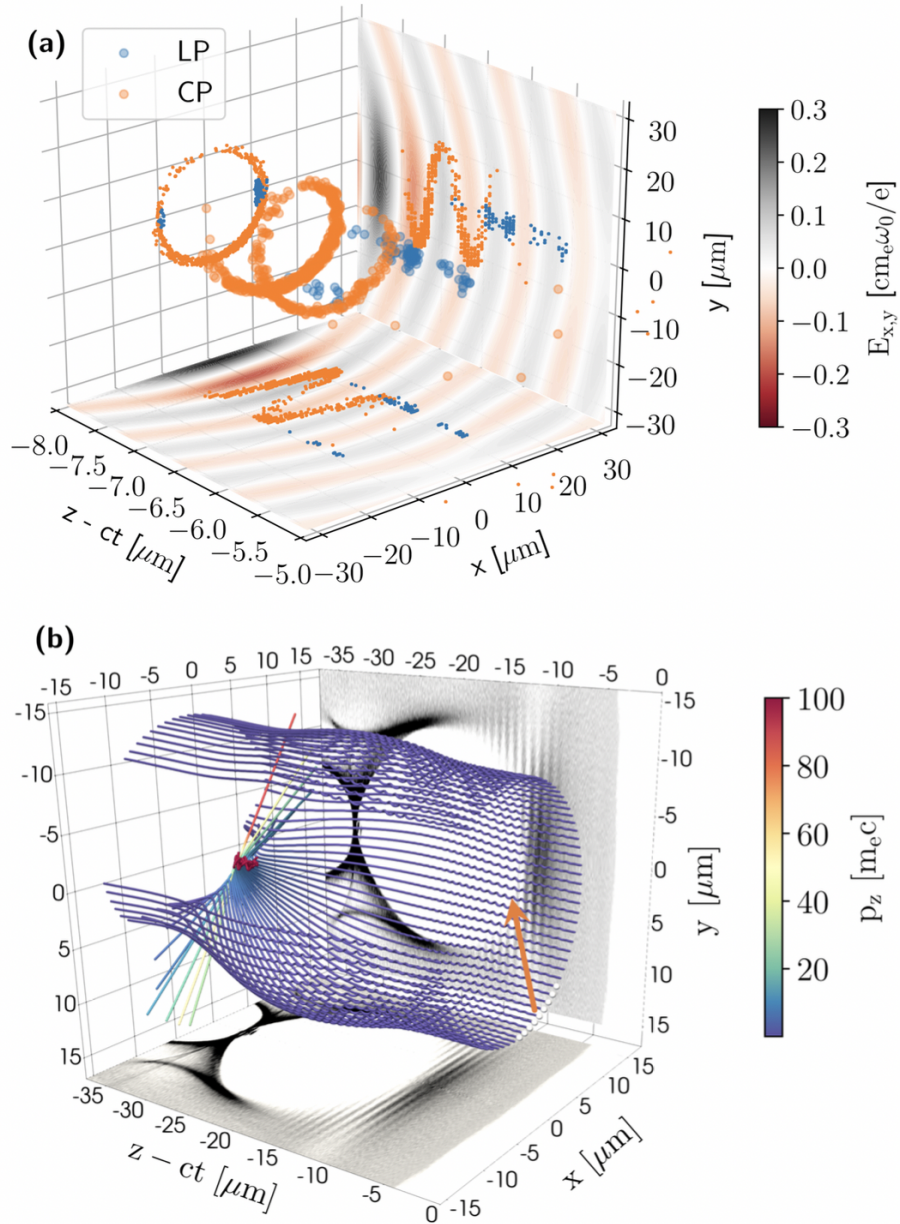
Figure 6.10: (a) Ionization location of injected electrons in the comoving frame. For a CP laser, electrons born at any phase in the ionization front can be injected if the laser vector potential points toward the beam axis. For an LP laser, only those born in the polarization plane can be injected. The color map represents the transverse laser field of E_x in the (x, z) plane and E_y in the (x, y) plane, respectively. (b) Particle tracking with static fields from PIC simulation in the CP laser case. The white dots represent the initial positions for the trapped particles. The orange arrow represents the direction of the vector potential at the starting point of the trajectories. The color scheme represents the longitudinal momentum gain for the tracked electrons along their trajectories. The gray scale plots on the two transverse planes show slices of the plasma density. Image credit: Ma (2020)

light in this region when density is increased in the centimeter scale gas cell.
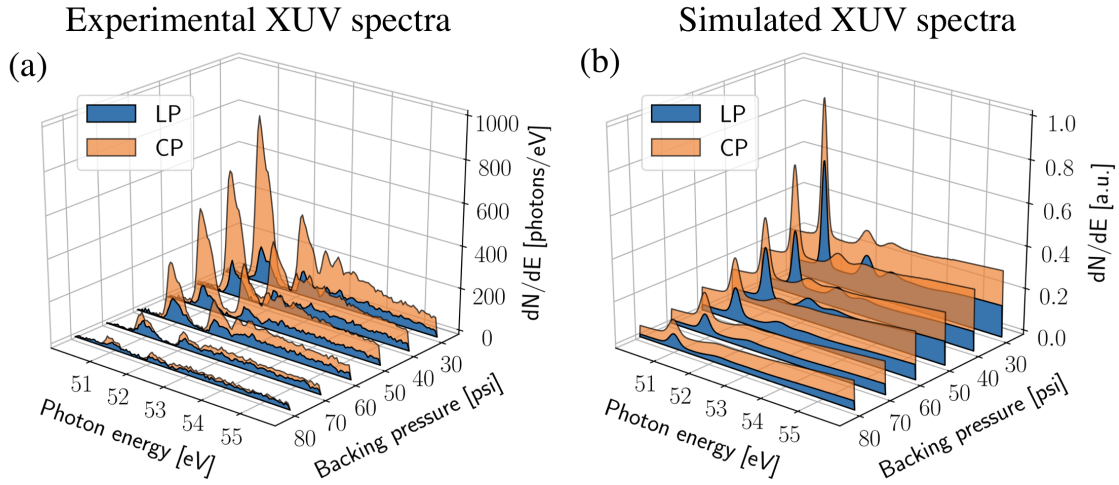
Figure 6.11: (a)Experimentally measured xuv spectra for various helium backing pressures (i.e., plasma densities). (b) xuv spectra from SCRAM atomic physics simulations with a thermal electron energy distribution with the same average energies as the electron spectra from a 1D PIC simulation. Image Credit: Ma (2020)

6.5   Conclusion

Soft xuv spectral measurements were made alongside electron spectra and inferences to the LWFA process were discovered. It was experimentally observed that by increasing the density, energy coupling and wake formation underwent changes. This is reasonable since electric field, resonantly exciting the wake and injection mechanisms depend on the plasma density. Xuv spectra may be used to diagnose the conditions of wake formation and injection mechanisms in the future. This may be a useful diagnostic for multiple-stage accelerators where a stable bubble should form but without further injection of electrons.

The observed continuum at 17-24 nm is likely betatron radiation. In the future experiments, more data should be taken in the low density regime since the high density plasma is re-

markably absorptive in this wavelength range. Further, camera position should be varied to study the emission lines (this requires the use of appropriate filters for the wavelength range of interest). Soft x-ray radiation, specially in the water window, may also be detected with different filters and positioning of the camera.

We can also conclude that self-injection dynamics and hence LWFA is polarization dependant. Circular polarization leads to significant differences in self-injection because it modifies the initial conditions for the electron trajectories and trapping is extremely sensitive to the details of the trajectory. The keV/c level momentum gain due to ATI at laser pulse front leads to a new injection mechanism for a laser pulse with a circular polarization with reduced threshed for density and higher charge beams. This injection mechanism is closely tied to the ionization processes before the arrival of the peak of the pulse. This is fundamentally different with the ionization injection mechanism, where more tightly bound inner shell electrons are ionized behind the pulse and inside the wakefield structure. Further, we may be able to produce a circularly polarized x-ray beam using LWFA, driven by a CP laser.

Chapter 7

Outlook and Conclusion

7.1 Future outlook

With the development of new laser systems, we are entering an exciting era for LWFA experiments. Researchers around the world are working to answer fundamental questions about this non-linear interaction as well as perfecting the implementation of this technique for various applications. For example, the new Zettawatt-Equivalent Ultra-short pulse laser System (ZEUS) at the University of Michigan will be one of the highest power laser systems worldwide. It will enable new studies such as pump-probe experiments with femtosecond x-rays to study ultra-short timescale material dynamics. Extreme Light Infrastructure (ELI) will soon be operational as a user facility with multiple sophisticated lasers. TFC technique can be used on these PW lasers with flat top profiles to produce single cycle pulses with 10s of Joules of energy. This will enable the experimental exploration of x-ray driven WFA in crystals and nanostructures. The High-Repetition-Rate Advanced Petawatt Laser System at ELI will deliver 30 Joules of energy in less than 30 fs with an unprecedented repetition rate of 10 Hz enabling real time optimization of the laser and resulting electron, ion and

x-ray beams.

7.2 Electron acceleration in crystals and nanostructures

Some aspects of crystal acceleration can be tested with the existing facilities such as FACET-II at SLAC, FAST at Fermilab, BELLA at LBNL and AWAKE at CERN. A comprehensive discussion of future experimental campaigns relating to this topic can be found in "Beam Acceleration in Crystals and Nanostructures", a summary of the first workshop on the subject held at Fermilab in 2019.

In the meantime, work is in progress on achieving a single cycle x-ray pulse through TFC and RC techniques. TFC technique was originally proposed to compress PW lasers with flat top profiles such as CETAL at the Institut National de Laser and lasers at ELI facilities. The concept of x-ray driven WFA in solid nanotubes can be tested after production of a single cycle x-ray pulse.

7.3 Commercial kHz LWFA

A near single cycle pulse has been achieved at UCI with a mJ energy scale laser operating at a kHz. This pulse can be converted to a single cycle x-ray pulse via RC. This could be a suitable x-ray source for generating a wakefield in nanostructures with TeV/cm acceleration gradient. The energy in the pulse will be small but as discussed before, a large energy may not be needed in this regime.

On another related note, proof of principle experiments to study wakefield generation with

shorter pulses can soon be conducted using the second and third harmonics of current Ti:Sapphire laser systems. Commercial kHz lasers can be used for these studies because of their small beam size. Electron beam characteristics and enhancement of betatron radiation generation can be experimentally studied at UCI as laser wavelength is decreased.

The compressed pulse at UCI ($\sim 7\,\mathrm{fs}$[1]) has a peak intensity of $\sim 10^{19}\,\mathrm{W/cm^2}$ and can be further increased to $> 10^{20}\,\mathrm{W/cm^2}$ with higher quality optics. This high-intensity short pulse propagating in a near critical density target can produce ~ 10 MeV energy electrons. In order to improve the electron beam quality, specifically designed gas-jets or gas-cells to control the profile of the target for density down-ramp injection and shock injection may be necessary.

In general, LWFA currently produces beams of lower quality compared to traditional accelerators. Improvements in terms of energy spread, total charge, divergence, emittance, and shot-to-shot stability are necessary before LWFA can be used for everyday applications.

LWFA involves a set of initial laser and target parameters. In addition, these parameters evolve with time according to various non-linear phenomena that affect the outcome. The consequences of subtle variations to some of these parameters such as laser wavefront has previously been studied in some experiments and simulations. However, a comprehensive scan of all the parameters has not yet been done. Machine Learning (ML) algorithms could be used to uncover the details of the complex laser-plasma dynamics and find patterns and relations between various laser and target parameters, their evolution, and the acceleration process. Generating a large set of experimental data is not yet feasible since high power lasers used for LWFA usually operate at a low repetition rate, anywhere between one shot every few minutes to couple shots per hour. Commercial kHz lasers recently have had success with accelerating electrons; however, generating a large experimental dataset will have its challenges since it involves simultaneous diagnostics for various parameters and saving the

_____

[1]~ 4 fs with broader bandwidth chirped mirrors

118

data for each shot at a fast pace. A large set of simulated data, carefully designed to mimic real experimental conditions including the imperfections and fluctuations might be a good place to start. The use of ML algorithms is particularly great here to look at a massive non-linear parameter space where humans generally fail to make the connections due to their biases. Any inherent grouping in the data or association rule that is discovered this way will have direct impact on bringing LWFA to real applications. This might enable researchers to identify factors that have a negative impact on the acceleration mechanism and possibly even improve the energy efficiency of the process.

Bibliography

[1] John Douglas Cockcroft and Ernest TS Walton. Experiments with high velocity positive ions. *Proceedings of the royal society of London. Series A, containing papers of a mathematical and physical character*, 129(811):477–489, 1930.

[2] John Douglas Cockcroft and Ernest TS Walton. Experiments with high velocity positive ions.—(i) further developments in the method of obtaining high velocity positive ions. *Proceedings of the Royal Society of London. Series A, Containing Papers of a Mathematical and Physical Character*, 136(830):619–630, 1932.

[3] R Wideroe. Archiv. f. electrotechnik 21, 387 (1929). *Google Scholar Sloan and Lawrence, Phys. Rev*, 38:2021, 1931.

[4] Ernest O Lawrence and Niels E Edlefsen. On the production of high speed protons. *Science*, 72(1867):376, 1930.

[5] Ernest O Lawrence and M Stanley Livingston. The production of high speed protons without the use of high voltages. *Physical Review*, 38(4):834, 1931.

[6] Wilfred Basil Mann. The cyclotron. 1948.

[7] US Department of Energy. Accelerators for america's future report. 2011.

[8] CM Charlie Ma and Tony Lomax. *Proton and carbon ion therapy*. CRC press, 2012.

[9] Wayne D Newhauser and Rui Zhang. The physics of proton therapy. *Physics in Medicine & Biology*, 60(8):R155, 2015.

[10] Jonathan B Farr, Jacob B Flanz, Alexander Gerbershagen, and Michael F Moyers. New horizons in particle therapy systems. *Medical physics*, 45(11):e953–e983, 2018.

[11] Vladimir I Veksler. New method for the acceleration of relativistic particles. In *Doklady Akademii Nauk USSR*, volume 43, pages 346–348, 1944.

[12] VI Veksler. The principle of coherent acceleration of charged particles. *The Soviet Journal of Atomic Energy*, 2(5):525–528, 1957.

[13] T. Tajima and J. M. Dawson. Laser electron accelerator. *Phys. Rev. Lett.*, 43(4):267, 1979.

[14] Donna Strickland and Gerard Mourou. Compression of amplified chirped optical pulses. *Optics communications*, 56(3):219–221, 1985.

[15] Pisin Chen, JM Dawson, Robert W Huff, and T Katsouleas. Acceleration of electrons by the interaction of a bunched electron beam with a plasma. *Physical review letters*, 54(7):693, 1985.

[16] James Benjamine Rosenzweig, DB Cline, B Cole, H Figueroa, W Gai, R Konecny, J Norem, P Schoessow, and J Simpson. Experimental observation of plasma wake-field acceleration. *Physical review letters*, 61(1):98, 1988.

[17] Erik Adli, Arun Ahuja, O Apsimon, Robert Apsimon, A-M Bachmann, D Barrientos, F Batsch, J Bauche, VK Berglyd Olsen, M Bernardini, et al. Acceleration of electrons in the plasma wakefield of a proton bunch. *Nature*, 561(7723):363–367, 2018.

[18] Enrico Fermi. Galactic magnetic fields and the origin of cosmic radiation. *The Astrophysical Journal*, 119:1, 1954.

[19] Toshikazu Ebisuzaki and Toshiki Tajima. Astrophysical zev acceleration in the relativistic jet from an accreting supermassive blackhole. *Astroparticle Physics*, 56:9–15, 2014.

[20] T Ebisuzaki and T Tajima. Pondermotive acceleration of charged particles along the relativistic jets of an accreting blackhole. *The European Physical Journal Special Topics*, 223(6):1113–1120, 2014.

[21] CK Lau, Po-Chun Yeh, Onnie Luk, Joseph McClenaghan, Toshikazu Ebisuzaki, and Toshiki Tajima. Ponderomotive acceleration by relativistic waves. *Physical Review Special Topics-Accelerators and Beams*, 18(2):024401, 2015.

[22] Theodore H Maiman et al. Stimulated optical radiation in ruby. 1960.

[23] FJ McClung and RW Hellwarth. Giant optical pulsations from ruby. *Journal of Applied Physics*, 33(3):828–829, 1962.

[24] LE Hargrove, Richard L Fork, and MA Pollack. Locking of he–ne laser modes induced by synchronous intracavity modulation. *Applied Physics Letters*, 5(1):4–5, 1964.

[25] Gérard A Mourou, CP Barty, and Michael D Perry. Ultrahigh-intensity laser: physics of the extreme on a tabletop. Technical Report 1, Lawrence Livermore National Lab., CA (United States), 1997.

[26] T Tajima and G Mourou. Zettawatt-exawatt lasers and their applications in ultrastrong-field physics. *Physical Review Special Topics-Accelerators and Beams*, 5(3):031301, 2002.

[27] G. Mourou, S. Mironov, E. Khazanov, and A. Sergeev. Single cycle thin film compressor opening the door to zeptosecond-exawatt physics. *Eur. Phys. J. Spec. Top.*, 223(6):1181–1188, 2014.

[28] N. M. Naumova, J. A. Nees, I. V. Sokolov, B. Hou, and G. A. Mourou. Relativistic generation of isolated attosecond pulses in a λ 3 focal volume. *Phys. Rev. Lett.*, 92(6):063902, 2004.

[29] So V Bulanov, NM Naumova, and FRANCESCO Pegoraro. Interaction of an ultrashort, relativistically strong laser pulse with an overdense plasma. *Physics of Plasmas*, 1(3):745–757, 1994.

[30] T. Tajima. Laser acceleration in novel media. *Eur. Phys. J. Spec. Top.*, 223(6):1037–1044, 2014.

[31] J. Wheeler, G. Mourou, and T. Tajima. Laser technology for advanced acceleration: Accelerating beyond tev. *Rev. Accel. Sci. and Tech.*, 9:151–163, 2016.

[32] X. Zhang, T. Tajima, D. Farinella, S. Youngmin, G. Mourou, JA Wheeler, P. Taborek, P. S. Chen, F. Dollar, and B. Shen. Particle-in-cell simulation of x-ray wakefield acceleration and betatron radiation in nanotubes. *Phys. Rev. Accel. Beams*, 19(10):101004, 2016.

[33] Sahel Hakimi, Tam Nguyen, Deano Farinella, Calvin K Lau, Hsuan-Yu Wang, Peter Taborek, Franklin Dollar, and Toshiki Tajima. Wakefield in solid state plasma with the ionic lattice force. *Physics of Plasmas*, 25(2):023112, 2018.

[34] M. L. Zhou, X. Q. Yan, G. Mourou, J. A. Wheeler, J. H. Bin, J. Schreiber, and T. Tajima. Proton acceleration by single-cycle laser pulses offers a novel monoenergetic and stable operating regime. *Phys. of Plasmas*, 23(4):043112, 2016.

[35] Gerard Mourou, Bill Brocklesby, Toshiki Tajima, and Jens Limpert. The future is fibre accelerators. *Nature Photonics*, 7(4):258–261, 2013.

[36] Toshiki Tajima, William Brocklesby, and Gérard Mourou. Ican: The next laser powerhouse. *Optics and Photonics News*, 24(5):36–43, 2013.

[37] K Nakajima, T Kawakubo, H Nakanishi, A Ogata, Y Kato, Y Kitagawa, R Kodama, K Mima, H Shiraga, K Suzuki, et al. A proof-of-principle experiment of laser wakefield acceleration. *Physica Scripta*, 1994(T52):61, 1994.

[38] K Nakajima, D Fisher, T Kawakubo, H Nakanishi, A Ogata, Y Kato, Y Kitagawa, R Kodama, K Mima, H Shiraga, et al. Observation of ultrahigh gradient electron acceleration by a self-modulated intense short laser pulse. *Physical Review Letters*, 74(22):4428, 1995.

[39] KA Marsh. Trapped electron acceleration by a laser-driven relativistic plasma wave. *Nature*, 368:7, 1994.

[40] François Amiranoff, S Baton, D Bernard, B Cros, D Descamps, F Dorchies, F Jacquet, Victor Malka, JR Marques, G Matthieussent, et al. Observation of laser wakefield acceleration of electrons. *Physical Review Letters*, 81(5):995, 1998.

[41] A Modena, Z Najmudin, AE Dangor, CE Clayton, KA Marsh, C Joshi, Victor Malka, CB Darrow, C Danson, D Neely, et al. Electron acceleration from the breaking of relativistic plasma waves. *nature*, 377(6550):606–608, 1995.

[42] Alexancer Pukhov and Jürgen Meyer-ter Vehn. Laser wake field acceleration: the highly non-linear broken-wave regime. *Applied Physics B*, 74(4-5):355–361, 2002.

[43] Wei Lu, M Tzoufras, C Joshi, FS Tsung, WB Mori, J Vieira, RA Fonseca, and LO Silva. Generating multi-gev electron bunches using single stage laser wakefield acceleration in a 3d nonlinear regime. *Physical Review Special Topics-Accelerators and Beams*, 10(6):061301, 2007.

[44] Jérôme Faure, Yannick Glinec, A Pukhov, S Kiselev, S Gordienko, E Lefebvre, J-P Rousseau, F Burgy, and Victor Malka. A laser–plasma accelerator producing monoenergetic electron beams. *Nature*, 431(7008):541–544, 2004.

[45] Stuart PD Mangles, CD Murphy, Zulfikar Najmudin, Alexander George Roy Thomas, JL Collier, Aboobaker E Dangor, EJ Divall, PS Foster, JG Gallacher, CJ Hooker, et al. Monoenergetic beams of relativistic electrons from intense laser–plasma interactions. *Nature*, 431(7008):535–538, 2004.

[46] C. G. R. Geddes, Cs. Toth, J. Van Tilborg, E. Esarey, C. B. Schroeder, D. Bruhwiler, C. Nieter, J. Cary, and W. P. Leemans. High-quality electron beams from a laser wakefield accelerator using plasma-channel guiding. *Nature*, 431(7008):538, 2004.

[47] Wim Leemans and Eric Esarey. Laser-driven plasma-wave electron accelerators. *Phys. Today*, 62(3):44–49, 2009.

[48] Wim P Leemans, Bob Nagler, Anthony J Gonsalves, Cs Tóth, Kei Nakamura, Cameron GR Geddes, ESCB Esarey, CB Schroeder, and SM Hooker. Gev electron beams from a centimetre-scale accelerator. *Nature physics*, 2(10):696–699, 2006.

[49] Chris E Clayton, JE Ralph, F Albert, RA Fonseca, SH Glenzer, Chandrasekar Joshi, Wei Lu, KA Marsh, Samuel F Martins, Warren B Mori, et al. Self-guided laser wakefield acceleration beyond 1 gev using ionization-induced injection. *Physical Review Letters*, 105(10):105003, 2010.

[50] WP Leemans, AJ Gonsalves, H-S Mao, K Nakamura, C Benedetti, CB Schroeder, Cs Tóth, J Daniels, DE Mittelberger, SS Bulanov, et al. Multi-gev electron beams from capillary-discharge-guided subpetawatt laser pulses in the self-trapping regime. *Physical review letters*, 113(24):245002, 2014.

[51] AJ Gonsalves, K Nakamura, J Daniels, C Benedetti, C Pieronek, TCH De Raadt, S Steinke, JH Bin, SS Bulanov, J Van Tilborg, et al. Petawatt laser guiding and electron beam acceleration to 8 gev in a laser-heated capillary discharge waveguide. *Physical review letters*, 122(8):084801, 2019.

[52] Dustin H Froula, David Turnbull, Andrew S Davies, Terrance J Kessler, Dan Haberberger, John P Palastro, Seung-Whan Bahk, Ildar A Begishev, Robert Boni, Sara Bucht, et al. Spatiotemporal control of laser intensity. *Nature Photonics*, 12(5):262, 2018.

[53] Alexander Debus, Richard Pausch, Axel Huebl, Klaus Steiniger, René Widera, Thomas E Cowan, Ulrich Schramm, and Michael Bussmann. Circumventing the dephasing and depletion limits of laser-wakefield acceleration. *Physical Review X*, 9(3):031044, 2019.

[54] JP Palastro, JL Shaw, P Franke, D Ramsey, TT Simpson, and DH Froula. Dephasingless laser wakefield acceleration. *Physical Review Letters*, 29, 2020.

[55] Eric Esarey, Phillip Sprangle, Jonathan Krall, and Antonio Ting. Overview of plasma-based accelerator concepts. *IEEE Transactions on plasma science*, 24(2):252–288, 1996.

[56] E. Esarey, C. B. Schroeder, and W. P. Leemans. Physics of laser-driven plasma-based electron accelerators. *Rev. Mod. Phys.*, 81(3):1229, 2009.

[57] T Tajima, K Nakajima, and G Mourou. Laser acceleration. *La Rivista del Nuovo Cimento*, 40:33–133, 2017.

[58] G. Mourou, T. Tajima, and S. V. Bulanov. Optics in the relativistic regime. *Rev. Mod. Phys.*, 78(2):309, 2006.

[59] Sébastien Corde, K Ta Phuoc, Guillaume Lambert, R Fitour, Victor Malka, Antoine Rousse, A Beck, and E Lefebvre. Femtosecond x rays from laser-plasma accelerators. *Reviews of Modern Physics*, 85(1):1, 2013.

[60] Donald Umstadter. Relativistic laser–plasma interactions. *Journal of Physics D: Applied Physics*, 36(8):R151, 2003.

[61] Karl Krushelnick and Victor Malka. Laser wakefield plasma accelerators. *Laser & Photonics Reviews*, 4(1):42–52, 2010.

[62] Toshiki Tajima. Laser acceleration and its future. *Proceedings of the Japan Academy, Series B*, 86(3):147–157, 2010.

[63] Simon Martin Hooker. Developments in laser-driven plasma accelerators. *Nature Photonics*, 7(10):775, 2013.

[64] Chan Joshi. Laser-driven plasma accelerators operating in the self-guided, blowout regime. *IEEE Transactions on plasma Science*, 45(12):3134–3146, 2017.

[65] T Tajima and V Malka. Laser plasma accelerators. *Plasma Physics and Controlled Fusion*, 62(3):034004, 2020.

[66] T. Tajima, X. Q. Yan, and T. Ebisuzaki. Wakefield acceleration. *Rev. Mod. Phys.*, 2020.

[67] Francis F Chen et al. *Introduction to plasma physics and controlled fusion*, volume 1. Springer, 1984.

[68] William Kruer. *The physics of laser plasma interactions*. Westview Press, 2017.

[69] Paul Gibbson. Short pulse laser interactions with matter: An introduction, 2005.

[70] Rick Trebino. *Frequency-resolved optical gating: the measurement of ultrashort laser pulses*. Springer Science & Business Media, 2012.

[71] Alexander A Andreev, Artur Afanasevich Mak, Artur Afanasevich Mak, and NA Solovev. *An introduction to hot laser plasma physics*, volume 233. Nova Science Pub Inc, 2000.

[72] Félicie Albert and Alec G. R. Thomas. Applications of laser wakefield accelerator-based light sources. *Plasma Physics and Controlled Fusion*, 58(10):103001, September 2016.

[73] V Yanovsky, V Chvykov, G Kalinchenko, P Rousseau, T Planchon, T Matsuoka, A Maksimchuk, J Nees, G Cheriaux, G Mourou, et al. Ultra-high intensity-300-tw laser at 0.1 hz repetition rate. *Optics Express*, 16(3):2109–2114, 2008.

[74] Stephen A Reed. *Electron and Proton Acceleration Using the 30 TW, 30 fs Hercules Laser.* PhD thesis, 2008.

[75] V Chvykov, P Rousseau, S Reed, G Kalinchenko, and V Yanovsky. Generation of 10 11 contrast 50 tw laser pulses. *Optics letters*, 31(10):1456–1458, 2006.

[76] Edmond Treacy. Optical pulse compression with diffraction gratings. *IEEE Journal of quantum Electronics*, 5(9):454–458, 1969.

[77] Stuart D Brorson and Hermann A Haus. Diffraction gratings and geometrical optics. *JOSA B*, 5(2):247–248, 1988.

[78] Deano Michael-Angelo Farinella. *Thin film compression toward the single-cycle regime for the advancement of high field*. PhD thesis, University of California, Irvine, 2018.

[79] Rick Trebino, Kenneth W DeLong, David N Fittinghoff, John N Sweetser, Marco A Krumbügel, Bruce A Richman, and Daniel J Kane. Measuring ultrashort laser pulses in the time-frequency domain using frequency-resolved optical gating. *Review of Scientific Instruments*, 68(9):3277–3295, 1997.

[80] Yannick Glinec, Jérôme Faure, A Guemnie-Tafo, Victor Malka, H Monard, JP Larbre, V De Waele, JL Marignier, and M Mostafavi. Absolute calibration for a broad range single shot electron spectrometer. *Review of scientific instruments*, 77(10):103301, 2006.

[81] T. D. Arber, K. Bennett, C. S. Brady, A. Lawrence-Douglas, M. G. Ramsay, N. J. Sircombe, P. Gillies, R. G. Evans, H. Schmitz, A. R. Bell, et al. Contemporary particle-in-cell approach to laser-plasma modelling. *Plasma Physics and Controlled Fusion*, 57(11):113001, 2015.

[82] Ricardo A Fonseca, Luis O Silva, Frank S Tsung, Viktor K Decyk, Wei Lu, Chuang Ren, Warren B Mori, S Deng, S Lee, T Katsouleas, et al. Osiris: A three-dimensional, fully relativistic particle in cell code for modeling plasma based accelerators. In *International Conference on Computational Science*, pages 342–351. Springer, 2002.

[83] C. K. Birdsall and A. B. Langdon. *Plasma physics via computer simulation.* CRC press, 2004.

[84] T. Tajima. *Computational plasma physics With applications to fusion and astrophysics.* Frontiers in Physics, Vol. 72, 1989.

[85] H. Wu. Jpic & how to make a pic code. *arXiv preprint arXiv:1104.3163*, 2011.

[86] H. Ruhl. Classical particle simulations with the psc code. *Ruhr-Universität Bochum*, 2005.

[87] T. Tajima and M. Cavenago. Crystal x-ray accelerator. *Phys. Rev. Lett.*, 59(13):1440, 1987.

[88] Mohammed Hassan, Adrian Wirth, Ivanka Grguras, Tran Trung Luu, Antoine Moulet, Vladislav Yakovlev, Justin Gagnon, Olga Razskazovskaya, Robin Santra, Stefan Pabst, Abdallah M. Azzeer, Zeyad A. Alahmed, Vladimir Pervak, Ferenc Krausz, and Eleftherios Goulielmakis. Attosecond physics with synthesized transients of light. In *Laser Science*, pages LW4H–2. Optical Society of America, 2012.

[89] Adrian Wirth, M Th Hassan, Ivanka Grguraš, Justin Gagnon, Antoine Moulet, Tran Trung Luu, S Pabst, R Santra, ZA Alahmed, AM Azzeer, V. S. Yakovlev1, V. Pervak, F. Krausz, and E. Goulielmakis. Synthesized light transients. *Science*, 334(6053):195–200, 2011.

[90] Bernhard Rau, T Tajima, and H Hojo. Coherent electron acceleration by subcycle laser pulses. *Physical review letters*, 78(17):3310, 1997.

[91] N. V. Myung, J. Lim, J. P. Fleurial, M. Yun, W. West, and D. Choi. Alumina nanotemplate fabrication on silicon substrate. *Nanotechnology*, 15(7):833, 2004.

[92] R. J. Lazarowich, P. Taborek, B-Y Yoo, and N. V. Myung. Fabrication of porous alumina on quartz crystal microbalances. *J. Appl. Phys.*, 101(10):104909, 2007.

[93] P. X. Hou, C. Liu, C. Shi, and H. M. Cheng. Carbon nanotubes prepared by anodic aluminum oxide template method. *Chin. Sci. Bull.*, 57(2-3):187–204, 2012.

[94] M. M. Shulaker, G. Hills, N. Patil, H. Wei, H. Chen, H-S. P. Wong, and S. Mitra. Carbon nanotube computer. *Nature*, 501(7468):526–530, 2013.

[95] T. Tajima and S. Ushioda. Surface polaritons in lo-phonon-plasmon coupled systems in semiconductors. *Phys. Rev. B*, 18(4):1892, 1978.

[96] R. F. Wallis and J. J. Brion. Theory of surface plasmon-surface optical phonon interaction in polar semiconductors. *Solid State Communications*, 9(23):2099–2103, 1971.

[97] A. Mooradian and A. L. McWhorter. Polarization and intensity of raman scattering from plasmons and phonons in gallium arsenide. *Phys. Rev. Lett.*, 19(15):849, 1967.

[98] A. A. Maradudin and D. L. Mills. Effect of spatial dispersion on the properties of a semi-infinite dielectric. *Phys. Rev. B*, 7(6):2787, 1973.

[99] E. G. Martin, A. A. Maradudin, and R. F. Wallis. Theory of surface polaritons in n-type silicon in the presence of a dc current. *Surface Science*, 91(1):37–50, 1980.

[100] Charles Kittel. *Introduction to solid state physics*. Wiley, 2005.

[101] Sahel Hakimi, Xiaomei Zhang, Calvin Lau, Peter Taborek, Franklin Dollar, and Toshiki Tajima. X-ray laser wakefield acceleration in a nanotube. *International Journal of Modern Physics A*, 34(34):1943011, 2019.

[102] K. Nakajima. Novel efficient thz undulator using a laser-driven wire. *Light: Science & Applications*, 6(5):e17063, 2017.

[103] D Guénot, D Gustas, A Vernier, B Beaurepaire, F Böhle, M Bocoum, M Lozano, Aurélie Jullien, R Lopez-Martens, Agustin Lifschitz, et al. Relativistic electron beams driven by khz single-cycle light pulses. *Nature Photonics*, 11(5):293–296, 2017.

[104] J. Cowley, C. Thornton, C. Arran, R. J. Shalloo, L. Corner, G. Cheung, C. D. Gregory, S. P. D. Mangles, N. H. Matlis, D. R. Symes, et al. Excitation and control of plasma wakefields by multiple laser pulses. *Phys. Rev. Lett.*, 119(4):044802, 2017.

[105] S. M. Hooker, R. Bartolini, S. P. D. Mangles, A. Tünnermann, L. Corner, J. Limpert, A. Seryi, and R. Walczak. Multi-pulse laser wakefield acceleration: a new route to efficient, high-repetition-rate plasma accelerators and high flux radiation sources. *Journal of Physics B: Atomic, Molecular and Optical Physics*, 47(23):234003, 2014.

[106] S. Cheshkov, T. Tajima, W. Horton, and K. Yokoya. Particle dynamics in multistage wakefield collider. *Phys. Rev. Spec. Top. Accel. Beams*, 3(7):071301, 2000.

[107] K. Nakajima, A. Deng, X. Zhang, B. Shen, J. Liu, R. Li, Z. Xu, T. Ostermayr, S. Petrovics, C. Klier, et al. Operating plasma density issues on large-scale laser-plasma accelerators toward high-energy frontier. *Phys. Rev. Spec. Top. Accel. Beams*, 14(9):091301, 2011.

[108] J. S. Liu, C. Q. Xia, W. T. Wang, H. Y. Lu, C. H. Wang, A. H. Deng, W. T. Li, H. Zhang, X. Y. Liang, Y. X. Leng, X. M. Lu, C. Wang, J. Z. Wang, K. Nakajima, R. X. Li, and Z. Z. Xu. All-optical cascaded laser wakefield accelerator using ionization-induced injection. *Phys. Rev. Lett.*, 107(3):035001, 2011.

[109] B. Newberger, T. Tajima, F. R. Huson, W. Mackay, B. C. Covington, J. R. Payne, ZG Zou, NK Mahale, and S. Ohnuma. Application of novel material in crystal accelerator concepts. In *Particle Accelerator Conference, 1989. Accelerator Science and Technology., Proceedings of the 1989 IEEE*, pages 630–632. IEEE, 1989.

[110] B. S. Newberger and T. Tajima. High-energy beam transport in crystal channels. *Phys. Rev. A*, 40(12):6897, 1989.

[111] T. Tajima, N. K. Mahale, W. W. MacKay, F. R. Huson, S. Ohnuma, B. C. Covington, J. Payne, and B. S. Newberger. Beam transport in the crystal x-ray accelerator. *Part. Accel.*, 32(IFSR-403):235–240, 1989.

[112] E. A. Peralta, K. Soong, R. J. England, E. R. Colby, Z. Wu, B. Montazeri, C. McGuinness, J. McNeur, K. J. Leedle, D. Walz, et al. Demonstration of electron acceleration in a laser-driven dielectric microstructure. *Nature*, 503(7474):91, 2013.

[113] Daiki Kawahito and Yasuaki Kishimoto. Multi-phase ionization dynamics of carbon thin film irradiated by high power short pulse laser. *Physics of Plasmas*, 24(10):103105, 2017.

[114] Q Su and Joseph H Eberly. Stabilization of a model atom in superintense field ionization. *JOSA B*, 7(4):564–568, 1990.

[115] G. W. Bryant, E. Waks, and J. R. Krenn. Plasmonics: The rise of quantum effects. *Optics and Photonics News*, 25(11):50–53, 2014.

[116] Y. Kojima, Y. Masaki, and F. Kannari. Control of ultrafast plasmon pulses by spatiotemporally phase-shaped laser pulses. *JOSA B*, 33(12):2437–2444, 2016.

[117] X. Liu, Y. Wang, and E. Potma. Surface-mediated four-wave mixing of nanostructures with counterpropagating surface plasmon polaritons. *Opt. Lett.*, 36(12):2348–2350, 2011.

[118] A. V. Kildishev, A. Boltasseva, and V. M. Shalaev. Planar photonics with metasurfaces. *Science*, 339(6125):1232009, 2013.

[119] K. Kurihara, F. Kuwashima, O. Morikawa, K. Yamamoto, and M. Tani. Principle and applications of plasmonic superfocusing of thz waves in metallic v-groove tapered waveguides: surface plasmon polaritons of thz waves as a complex system of electrons and electromagnetic waves. *Rev. Laser Eng.*, 45(3):158–164, 2017.

[120] H Yasufuku, H Yoshikawa, M Kimura, K Ito, K Tani, and S Fukushima. Application of x-ray photoemission electron microscopy developed at spring-8 bl15xu. *Surface and interface analysis*, 36(8):892–895, 2004.

[121] Sencer Ayas, Andi Cupallari, and Aykutlu Dana. Probing hot-electron effects in wide area plasmonic surfaces using x-ray photoelectron spectroscopy. *Applied Physics Letters*, 105(22):221608, 2014.

[122] G. Andonian, D. Stratakis, M. Babzien, S. Barber, M. Fedurin, E. Hemsing, K. Kusche, P. Muggli, B. O'Shea, X. Wei, O. B. Williams, V. Yakimenko, and J. B. Rosenzweig. Dielectric wakefield acceleration of a relativistic electron beam in a slab-symmetric dielectric lined waveguide. *Phys. Rev. Lett.*, 108(24):244801, 2012.

[123] B. D. O'Shea, G. Andonian, S. K. Barber, K. L. Fitzmorris, S. Hakimi, J. Harrison, P. D. Hoang, M. J. Hogan, B. Naranjo, O. B. Williams, V. Yakimenko, and J. B. Rosenzweig. Observation of acceleration and deceleration in gigaelectron-volt-per-metre gradient dielectric wakefield accelerators. *Nature communications*, 7, 2016.

[124] T. N. Huan, R. T. Jane, A. Benayad, L. Guetaz, P. D. Tran, and V. Artero. Bio-inspired noble metal-free nanomaterials approaching platinum performances for h 2 evolution and uptake. *Energy & Env. Sci.*, 9(3):940–947, 2016.

[125] T. R. Simmons, G. Berggren, M. Bacchi, M. Fontecave, and V. Artero. Mimicking hydrogenases: From biomimetics to artificial enzymes. *Coord. Chem. Rev.*, 270:127–150, 2014.

[126] D. Brazzolotto, M. Gennari, N. Queyriaux, T. R. Simmons, J. Pécaut, S. Demeshko, F. Meyer, M. Orio, V. Artero, and C. Duboc. Nickel centred h+ reduction catalysis in a model of [nife] hydrogenase. *Nature chemistry*, 8(11):1054, 2016.

[127] N. Kaeffer, A. Morozan, J. Fize, E. Martinez, L. Guetaz, and V. Artero. The dark side of molecular catalysis: Diimine–dioxime cobalt complexes are not the actual hydrogen evolution electrocatalyst in acidic aqueous solutions. *ACS Catalysis*, 6(6):3727–3737, 2016.

[128] D. M. Farinella, J. Wheeler, A. E. Hussein, J. Nees, M. Stanfield, N. Beier, Y. Ma, G. Cojocaru, R. Ungureanu, M. Pittman, J. Demailly, E. Baynard, R. Fabbri, M. Masruri, R. Secareanu, A. Naziru, R. Dabu, A. Maksimchuk, K. Krushelnick, D. Ros, G. Mourou, T. Tajima, and F. Dollar. Focusability of laser pulses at petawatt transport intensities in thin-film compression. *Journal of the Optical Society of America B*, 36(2):A28, February 2019.

[129] M. Masruri, J. Wheeler, I. Dancus, R. Fabbri, A. Nazîru, R. Secareanu, D. Ursescu, G. Cojocaru, R. Ungureanu, D. Farinella, M. Pittman, S. Mironov, S. Balascuta, D. Doria, D. Ros, and R. Dabu. Optical Thin Film Compression for Laser Induced Plasma Diagnostics. In *Conference on Lasers and Electro-Optics*, page SW4E.3, San Jose, California, 2019. OSA.

[130] Askash A. Sahai and Toshiki Tajima. Solid-state tube accelerator using surface wave wakefields in crystals. *International Journal of Modern Physics A*, 2019.

[131] Mattias Marklund and Padma K. Shukla. Nonlinear collective effects in photon-photon and photon-plasma interactions. *Reviews of Modern Physics*, 78(2):591–640, May 2006.

[132] A.J. Krasznahorkay, M. Csatlós, L. Csige, Z. Gácsi, J. Gulyás, M. Hunyadi, I. Kuti, B.M. Nyakó, L. Stuhl, J. Timár, T.G. Tornyi, Zs. Vajta, T.J. Ketel, and A. Krasznahorkay. Observation of Anomalous Internal Pair Creation in $^{8}\mathrm{Be}$: A Possible Indication of a Light, Neutral Boson. *Physical Review Letters*, 116(4):042501, January 2016.

[133] Jonathan L. Feng, Bartosz Fornal, Iftah Galon, Susan Gardner, Jordan Smolinsky, Tim M.P. Tait, and Philip Tanedo. Protophobic Fifth-Force Interpretation of the Observed Anomaly in $^{8}\mathrm{Be}$ Nuclear Transitions. *Physical Review Letters*, 117(7):071803, August 2016.

[134] Askash A. Sahai, Toshiki Tajima, and Vladimir Shiltsev. Schemes of laser muon acceleration: ultra-short, micron-scale beams. *International Journal of Modern Physics A*, 2019.

[135] Scott B. Nicks, Toshiki Tajima, Dante , Roa, Alec Necas, and Gerard A. Mourou. Laser-wakefield application to endoscopic oncology. *International Journal of Modern Physics A*, 2019.

[136] Toshiki Tajima, Masaki Kando, and Masahiro Teshima. Feeling the texture of vacuum: laser acceleration toward pev. *Progress of theoretical physics*, 125(3):617–631, 2011.

[137] G. Amelino-Camelia, John Ellis, N. E. Mavromatos, D. V. Nanopoulos, and Subir Sarkar. Tests of quantum gravity from observations of -ray bursts. *Nature*, 393(6687):763–765, June 1998.

[138] Y. M. Shin. Beam-driven acceleration in ultra-dense plasma media. *Appl. Phys. Lett.*, 105(11):114106, 2014.

[139] B Svedung Wettervik, A Gonoskov, and M Marklund. Prospects and limitations of wakefield acceleration in solids. *arXiv preprint arXiv:1709.02190*, 2017.

[140] LaserNetUS. Center for ultrafast optical science. `https://www.lasernetus.org/facility/center-ultrafast-optical-science`, 2020.

[141] Z-H He, B Hou, V Lebailly, JA Nees, K Krushelnick, and AGR Thomas. Coherent control of plasma dynamics. *Nature communications*, 6(1):1–7, 2015.

[142] SJD Dann, CD Baird, N Bourgeois, O Chekhlov, S Eardley, CD Gregory, J-N Gruse, J Hah, D Hazra, SJ Hawkes, et al. Laser wakefield acceleration with active feedback at 5 hz. *Physical Review Accelerators and Beams*, 22(4):041303, 2019.

[143] M Stanfield, NF Beier, S Hakimi, H. Allison, DM Farinella, AE Hussein, T Tajima, and F Dollar. Relativistic few cycle laser pulses produced from self phase modulation in thin dielectric media. *Submitted to Nature Photonics*, 2020.

[144] ZH He, B Hou, JA Nees, JH Easter, Jérôme Faure, K Krushelnick, and AGR Thomas. High repetition-rate wakefield electron source generated by few-millijoule, 30 fs laser pulses on a density downramp. *New Journal of Physics*, 15(5):053016, 2013.

[145] B Beaurepaire, A Vernier, M Bocoum, F Böhle, A Jullien, JP Rousseau, T Lefrou, D Douillet, G Iaquaniello, R Lopez-Martens, et al. Effect of the laser wave front in a laser-plasma accelerator. *Physical Review X*, 5(3):031012, 2015.

[146] AJ Goers, GA Hine, L Feder, B Miao, F Salehi, JK Wahlstrand, and HM Milchberg. Multi-mev electron acceleration by subterawatt laser pulses. *Physical review letters*, 115(19):194802, 2015.

[147] Fatholah Salehi, AJ Goers, GA Hine, Linus Feder, Donghoon Kuk, Bo Miao, Daniel Woodbury, Ki-Yong Kim, and HM Milchberg. Mev electron acceleration at 1 khz with¡ 10 mj laser pulses. *Optics letters*, 42(2):215–218, 2017.

[148] Dominykas Gustas, Diego Guénot, Aline Vernier, Shankar Dutt, Frederik Böhle, Rodrigo Lopez-Martens, Agustin Lifschitz, and Jérôme Faure. High-charge relativistic electron bunches from a khz laser-plasma accelerator. *Physical Review Accelerators and Beams*, 21(1):013401, 2018.

[149] Z-H He, AGR Thomas, B Beaurepaire, JA Nees, B Hou, Victor Malka, K Krushelnick, and Jérôme Faure. Electron diffraction using ultrafast electron bunches from a laser-wakefield accelerator at khz repetition rate. *Applied Physics Letters*, 102(6):064104, 2013.

[150] Yusa Muroya, Mingzhang Lin, Zhenhui Han, Yuta Kumagai, Akira Sakumi, Toru Ueda, and Yosuke Katsumura. Ultra-fast pulse radiolysis: A review of the recent system progress and its application to study on initial yields and solvation processes of solvated electrons in various kinds of alcohols. *Radiation Physics and Chemistry*, 77(10-12):1176–1182, 2008.

[151] B Beaurepaire, Agustin Lifschitz, and Jérôme Faure. Electron acceleration in sub-relativistic wakefields driven by few-cycle laser pulses. *New Journal of Physics*, 16(2):023023, 2014.

[152] Jérôme Faure, Dominikas Gustas, Diego Guénot, Aline Vernier, Frederik Böhle, Marie Ouillé, Stefan Haessler, R Lopez-Martens, and Agustin Lifschitz. A review of recent progress on laser-plasma acceleration at khz repetition rate. *Plasma Physics and Controlled Fusion*, 61(1):014012, 2018.

[153] Lucas Rovige, Julius Huijts, Aline Vernier, Vidmantas Tomkus, Valdas Girdauskas, Gediminas Raciukaitis, Juozas Dudutis, Valdemar Stankevic, Paulius Gecys, Marie Ouillé, et al. Demonstration of stable long-term operation of a kilohertz laser-plasma accelerator. *arXiv preprint arXiv:2005.06929*, 2020.

[154] Alexander Buck, Johannes Wenz, Jiancai Xu, Konstantin Khrennikov, Karl Schmid, Matthias Heigoldt, Julia M Mikhailova, M Geissler, B Shen, Ferenc Krausz, et al. Shock-front injector for high-quality laser-plasma acceleration. *Physical review letters*, 110(18):185006, 2013.

[155] Carlo Benedetti, CB Schroeder, Eric Esarey, Francesco Rossi, and WP Leemans. Numerical investigation of electron self-injection in the nonlinear bubble regime. *Physics of Plasmas*, 20(10):103108, 2013.

[156] Sergei Bulanov, Nataria Naumova, Francesco Pegoraro, and Junichi Sakai. Particle injection into the wave acceleration phase due to nonlinear wake wave breaking. *Physical Review E*, 58(5):R5257, 1998.

[157] Hyyong Suk, Nick Barov, James Benjamin Rosenzweig, and E Esarey. Plasma electron trapping and acceleration in a plasma wake field using a density transition. In *The Physics Of High Brightness Beams*, pages 404–417. World Scientific, 2000.

[158] Karl Schmid, Alexander Buck, Christopher MS Sears, Julia M Mikhailova, Raphael Tautz, Daniel Herrmann, Michael Geissler, Ferenc Krausz, and Laszlo Veisz. Density-transition based electron injector for laser driven wakefield accelerators. *Physical Review Special Topics-Accelerators and Beams*, 13(9):091301, 2010.

[159] Matthias Burza, Arkady Gonoskov, Kristoffer Svensson, Franck Wojda, Anders Persson, Martin Hansson, Guillaume Genoud, Mattias Marklund, C-G Wahlström, and Olle Lundh. Laser wakefield acceleration using wire produced double density ramps. *Physical Review Special Topics-Accelerators and Beams*, 16(1):011301, 2013.

[160] WT Wang, WT Li, JS Liu, ZJ Zhang, R Qi, CH Yu, JQ Liu, M Fang, ZY Qin, C Wang, et al. High-brightness high-energy electron beams from a laser wakefield accelerator via energy chirp control. *Physical review letters*, 117(12):124801, 2016.

[161] Myung Hoon Cho, Vishwa Bandhu Pathak, Hyung Taek Kim, and Chang Hee Nam. Controlled electron injection facilitated by nanoparticles for laser wakefield acceleration. *Scientific reports*, 8(1):1–8, 2018.

[162] Min Chen, Zheng-Ming Sheng, Yan-Yun Ma, and Jie Zhang. Electron injection and trapping in a laser wakefield by field ionization to high-charge states of gases, 2006.

[163] Arthur Pak, KA Marsh, SF Martins, W Lu, WB Mori, and C Joshi. Injection and trapping of tunnel-ionized electrons into laser-produced wakes. *Physical Review Letters*, 104(2):025003, 2010.

[164] C McGuffey, AGR Thomas, W Schumaker, T Matsuoka, V Chvykov, FJ Dollar, G Kalintchenko, V Yanovsky, A Maksimchuk, K Krushelnick, et al. Ionization induced trapping in a laser wakefield accelerator. *Physical review letters*, 104(2):025004, 2010.

[165] D Umstadter, JK Kim, and E Dodd. Laser injection of ultrashort electron pulses into wakefield plasma waves. *Physical review letters*, 76(12):2073, 1996.

[166] E Esarey, RF Hubbard, WP Leemans, A Ting, and P Sprangle. Electron injection into plasma wakefields by colliding laser pulses. *Physical Review Letters*, 79(14):2682, 1997.

[167] H Kotaki, S Masuda, M Kando, JK Koga, and K Nakajima. Head-on injection of a high quality electron beam by the interaction of two laser pulses. *Physics of Plasmas*, 11(6):3296–3302, 2004.

[168] G Fubiani, E Esarey, CB Schroeder, and WP Leemans. Beat wave injection of electrons into plasma waves using two interfering laser pulses. *Physical Review E*, 70(1):016402, 2004.

[169] X Davoine, E Lefebvre, Clément Rechatin, Jérôme Faure, and Victor Malka. Cold optical injection producing monoenergetic, multi-gev electron bunches. *Physical review letters*, 102(6):065001, 2009.

[170] B Hidding, G Pretzler, JB Rosenzweig, T Königstein, D Schiller, and DL Bruhwiler. Ultracold electron bunch generation via plasma photocathode emission and acceleration in a beam-driven plasma blowout. *Physical review letters*, 108(3):035001, 2012.

[171] R Lehe, AF Lifschitz, X Davoine, Cédric Thaury, and Victor Malka. Optical transverse injection in laser-plasma acceleration. *Physical review letters*, 111(8):085005, 2013.

[172] L-L Yu, Eric Esarey, CB Schroeder, J-L Vay, Carlo Benedetti, CGR Geddes, Min Chen, and WP Leemans. Two-color laser-ionization injection. *Physical review letters*, 112(12):125001, 2014.

[173] Ming Zeng, Min Chen, Lu-Le Yu, Warren B Mori, Zheng-Ming Sheng, Bernhard Hidding, DA Jaroszynski, and Jie Zhang. Multichromatic narrow-energy-spread electron bunches from laser-wakefield acceleration with dual-color lasers. *Physical review letters*, 114(8):084801, 2015.

[174] Zahra M Chitgar, Paul Gibbon, Jürgen Böker, Andreas Lehrach, and Markus Büscher. Electron self-injection threshold for the tandem-pulse laser wakefield accelerator. *Physics of Plasmas*, 27(2):023106, 2020.

[175] Grigory Golovin, Wenchao Yan, Ji Luo, Colton Fruhling, Dan Haden, Baozhen Zhao, Cheng Liu, Min Chen, Shouyuan Chen, Ping Zhang, et al. Electron trapping from interactions between laser-driven relativistic plasma waves. *Physical review letters*, 121(10):104801, 2018.

[176] J Vieira, SF Martins, VB Pathak, RA Fonseca, WB Mori, and LO Silva. Magnetic control of particle injection in plasma based accelerators. *Physical review letters*, 106(22):225001, 2011.

[177] S Kneip, C McGuffey, JL Martins, SF Martins, C Bellei, V Chvykov, F Dollar, R Fonseca, C Huntington, G Kalintchenko, et al. Bright spatially coherent synchrotron x-rays from a table-top source. *Nature Physics*, 6(12):980–983, 2010.

[178] JM Cole, JC Wood, NC Lopes, K Poder, RL Abel, S Alatabi, JSJ Bryant, A Jin, S Kneip, K Mecseki, et al. Laser-wakefield accelerators as hard x-ray sources for 3d medical imaging of human bone. *Scientific reports*, 5(1):1–7, 2015.

133

[179] Victor Malka, Jérôme Faure, Yannick Glinec, Clément Rechatin, Thomas Fuchs, Uwe Oelfke, and Hannitra Szymanowski. Medical applications with electron beam generated by laser plasma accelerators. In *Commercial and Biomedical Applications of Ultrafast Lasers VIII*, volume 6881, page 68810B. International Society for Optics and Photonics, 2008.

[180] Kyung Nam Kim, Yonghun Hwangbo, Seok-Gy Jeon, and Jaehoon Kim. Characteristics of high electron beam generation and dose distribution in laser wakefield accelerator for cancer treatment. In *2018 IEEE Advanced Accelerator Concepts Workshop (AAC)*, pages 1–5. IEEE, 2018.

[181] Shouyuan Chen, Grigory Golovin, Cameron Miller, Daniel Haden, Sudeep Banerjee, Ping Zhang, Cheng Liu, Jun Zhang, Baozhen Zhao, Shaun Clarke, et al. Shielded radiography with a laser-driven mev-energy x-ray source. *Nuclear Instruments and Methods in Physics Research Section B: Beam Interactions with Materials and Atoms*, 366:217–223, 2016.

[182] Aghapi G Mordovanakis, Paul-Edouard Masson-Laborde, James Easter, Konstantin Popov, Bixue Hou, Gérard Mourou, Wojciech Rozmus, and Malcolm G Haines. John nees, and karl krushelnick. temperature scaling of hot electrons produced by a tightly focused relativistic-intensity laser at 0.5 khz repetition rate. *Applied Physics Letters*, 96(7):071109, 2010.

[183] MG Haines, MS Wei, FN Beg, and RB Stephens. Hot-electron temperature and laser-light absorption in fast ignition. *Physical Review Letters*, 102(4):045008, 2009.

[184] FN Beg, AR Bell, AE Dangor, CN Danson, AP Fews, ME Glinsky, BA Hammel, P Lee, PA Norreys, and Ma Tatarakis. A study of picosecond laser–solid interactions up to 1019 w cm- 2. *Physics of plasmas*, 4(2):447–457, 1997.

[185] Y Ma, D Seipt, AE Hussein, S Hakimi, NF Beier, SB Hansen, J Hinojosa, A Maksimchuk, J Nees, K Krushelnick, et al. Polarization-dependent self-injection by above threshold ionization heating in a laser wakefield accelerator. *Physical Review Letters*, 124(11):114801, 2020.

[186] S-W Bahk, Pascal Rousseau, TA Planchon, Vladimir Chvykov, Galina Kalintchenko, Anatoly Maksimchuk, GA Mourou, and Victor Yanovsky. Generation and characterization of the highest laser intensities (10 22 w/cm 2). *Optics letters*, 29(24):2837–2839, 2004.

[187] M Vargas, W Schumaker, Z-H He, Z Zhao, K Behm, V Chvykov, B Hou, K Krushelnick, A Maksimchuk, V Yanovsky, et al. Improvements to laser wakefield accelerated electron beam stability, divergence, and energy spread using three-dimensional printed two-stage gas cell targets. *Applied Physics Letters*, 104(17):174103, 2014.

[188] Mitsuo Takeda, Hideki Ina, and Seiji Kobayashi. Fourier-transform method of fringe-pattern analysis for computer-based topography and interferometry. *JosA*, 72(1):156–160, 1982.

[189] Stuart Peter David Mangles. *Measurements of relativistic electrons from intense laser-plasma interactions.* PhD thesis, Imperial College London (University of London), 2005.

[190] N Nakanii, K Kondo, T Yabuuchi, K Tsuji, KA Tanaka, S Suzuki, T Asaka, K Yanagida, H Hanaki, T Kobayashi, et al. Absolute calibration of imaging plate for gev electrons. *Review of Scientific Instruments*, 79(6):066102, 2008.

[191] Zhen Zhao. *Control of Synchrotron X-ray Emission from Laser Wakefield Accelerators.* PhD thesis, 2016.

[192] D Neely, D Chambers, C Danson, P Norreys, S Preston, F Quinn, M Roper, J Wark, and M Zepf. A multi-channel soft x-ray flat-field spectrometer. In *AIP Conference Proceedings*, volume 426, pages 479–484. American Institute of Physics, 1998.

[193] P Sprangle, Cha-Mei Tang, and E Esarey. Relativistic self-focusing of short-pulse radiation beams in plasmas. *IEEE transactions on plasma science*, 15(2):145–153, 1987.

[194] S Hakimi, NF Beier, Y Ma, J Hinojosa, SB. Hansen, AE Hussein, A Maksimchuk, J Nees, T Tajima, K Krushelnick, Thomas AGR, and F Dollar. Plasma temperature correlation with electron acceleration processes in laser wakefield acceleration. *In preparation*, 2020.

[195] PB Corkum, NH Burnett, and F Brunel. Above-threshold ionization in the long-wavelength limit. *Physical review letters*, 62(11):1259, 1989.

[196] CI Moore, A Ting, SJ McNaught, J Qiu, HR Burris, and P Sprangle. A laser-accelerator injector based on laser ionization and ponderomotive acceleration of electrons. *Physical review letters*, 82(8):1688, 1999.

[197] CI Moore, A Ting, T Jones, E Briscoe, B Hafizi, RF Hubbard, and P Sprangle. Measurements of energetic electrons from the high-intensity laser ionization of gases. *Physics of Plasmas*, 8(5):2481–2487, 2001.

[198] Bing Zhou, Aurélien Houard, Yi Liu, Bernard Prade, André Mysyrowicz, Arnaud Couairon, Patrick Mora, Christopher Smeenk, Ladan Arissian, and Paul Corkum. Measurement and control of plasma oscillations in femtosecond filaments. *Physical review letters*, 106(25):255002, 2011.

[199] BM Penetrante and JN Bardsley. Residual energy in plasmas produced by intense subpicosecond lasers. *Physical Review A*, 43(6):3100, 1991.

[200] N Lemos, T Grismayer, L Cardoso, J Geada, G Figueira, and JM Dias. Effects of laser polarization in the expansion of plasma waveguides. *Physics of Plasmas*, 20(10):103109, 2013.

[201] SB Hansen, J Bauche, C Bauche-Arnoult, and MF Gu. Hybrid atomic models for spectroscopic plasma diagnostics. *High Energy Density Physics*, 3(1-2):109–114, 2007.

Appendix A

Derivations

A.1 Dispersion Relations

Derivation for the dispersion relation is shown here. For simplicity, let us assume that all vector quantities are in the x direction and perform the derivation of the dispersion relation in one dimension only. We will also assume that electrons have a constant drift velocity and are going through a solid medium. Starting from the continuity equation and using small amplitude perturbation theory to linearize the equations we write:

$$\frac{\partial n_e}{\partial t} + \nabla \cdot (n_e v_e) = 0, \tag{A.1}$$

$$\frac{\partial(n_{e0} + n_{e1} + ...)}{\partial t} + \nabla \cdot (n_{e0} + n_{e1} + ...)(v_{e0} + v_{e1} + ...) = 0, \tag{A.2}$$

Equating the 1st order terms from above and using Fourier theory we obtain:

$$\frac{\partial n_{\alpha 1}}{\partial t} + \nabla \cdot (n_{\alpha 0} v_{\alpha 1} + n_{\alpha 1} v_{\alpha 0}) = 0, \tag{A.3}$$

$$-i\omega n_{\alpha 1} + ik_x n_{\alpha 0} v_{\alpha 1} + ik_x n_{\alpha 1} v_{\alpha 0} = 0, \tag{A.4}$$

where $\alpha = e, i$ and $v_{i0} = 0$ since ions are assumed to be immobile due to their larger mass. Starting from the general equation of motion for electrons and ions and only keeping the first order terms, we obtain:

$$m_e n_e \left(\frac{\partial v_e}{\partial t} + (v_e) \cdot \nabla v_e \right) = n_e q_e E - \nabla P_e, \tag{A.5}$$

$$m_e (n_{e0} + n_{e1}) \left(\frac{\partial (v_{e0} + v_{e1})}{\partial t} + (v_{e0} + v_{e1}) \cdot \nabla v_e \right) = (n_{e0} + n_{e1}) q_e (E_0 + E_1) - \nabla P_e, \tag{A.6}$$

$$m_e n_{e0} \left(\frac{\partial v_{e1}}{\partial t} + m_e n_{e0} v_{e0} \cdot \nabla v_{e1} \right) = n_{e0} q_e E_1 - \nabla \gamma n_{e1} T_{e0}, \tag{A.7}$$

$$- m_e n_{e0} i \omega v_{e1} + m_e n_{e0} v_{e0} i k_x v_{e1} = -n_{e0} e E_1 - i k_x \gamma n_{e1} T_{e0}, \tag{A.8}$$

$$m_i n_i \left(\frac{\partial v_i}{\partial t} + v_i \cdot \nabla v_i \right) = n_i q_i E - K_i (x_i - x_{i0}) \tag{A.9}$$

From Maxwell's equations, we have the Poisson equation $\nabla \cdot E_1 = 4\pi e(n_{i1} - n_{e1})$ and by definition we have expressions for particle's velocity in terms of position $v_{e,i} = -i\omega x_{e,i}$. The dispersion equation is obtained by simplifying the above 7 equations:

$$\epsilon(k, \omega) = 1 - \frac{\omega_{pi}^2}{(\omega^2 - \omega_{TO}^2)} - \frac{\omega_{pe}^2}{(\omega - k_x v_d)^2 - k_x^2 v_e^2} = 0, \tag{A.10}$$

where $\omega_{TO} = \sqrt{K_i/m_i}$ is the phonon frequency and v_d is the drift velocity of the electrons. If ω_{TO} and v_d are set to zero, we will obtain the general dispersion relation with the plasma oscillation and ion acoustic modes as solutions. If ω_{TO} is not negligible, the ion acoustic mode will be modified to $\omega^2 = k^2 c_s^2 + \omega_{TO}^2$. If v_d is not zero, we will obtain the Buneman instability. These different cases are shown below.

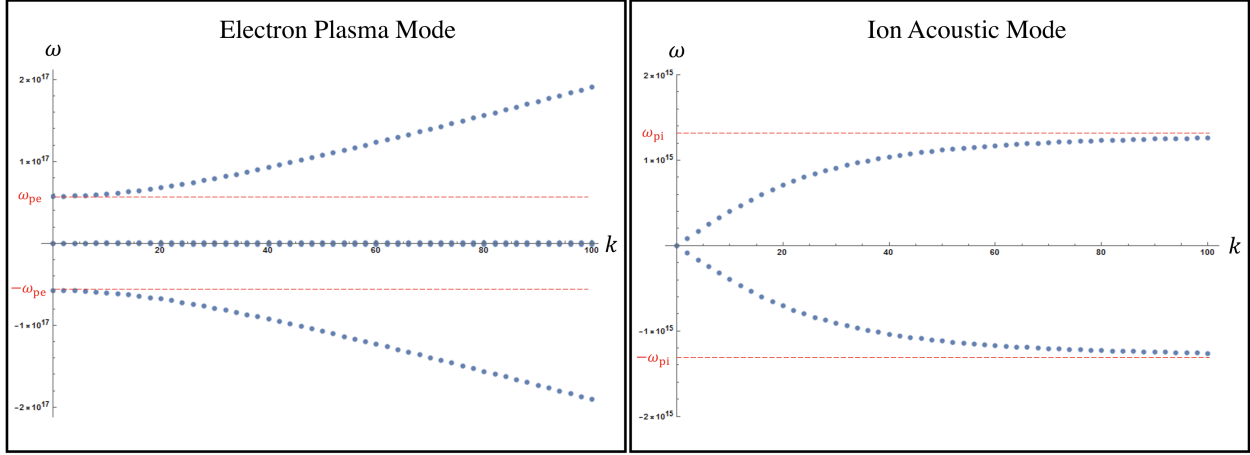**General dispersion relation**

$\omega_{TO} = 0, v_d = 0$

Figure A.1: $n_e = 1 \times 10^{30}$ cm^{-3}, $\omega_{pe} = 5.64 \times 10^{16}$ rad/sec, $\omega_{pi} = 1.32 \times 10^{15}$ rad/sec, $v_e^2 = 3.3 \times 10^{30}$ (m/s)^2

General dispersion relation modified by addition of lattice force
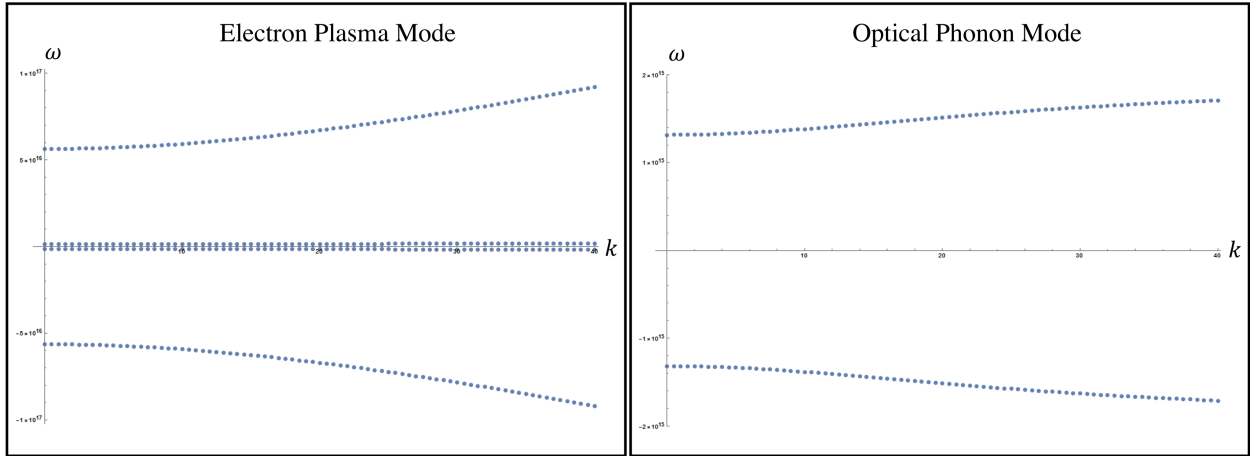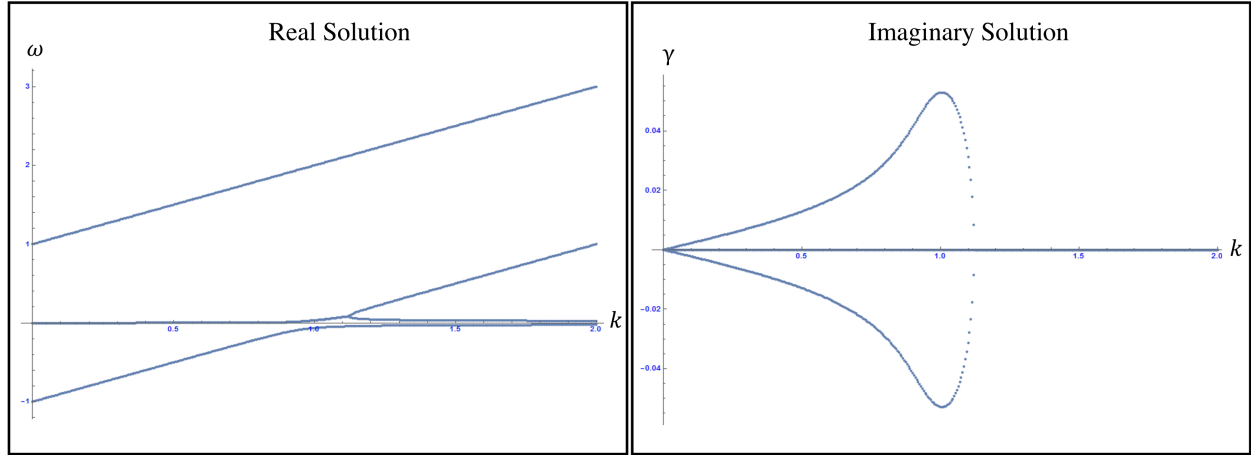
$\omega_{TO} = \omega_{pi}$, $v_d = 0$

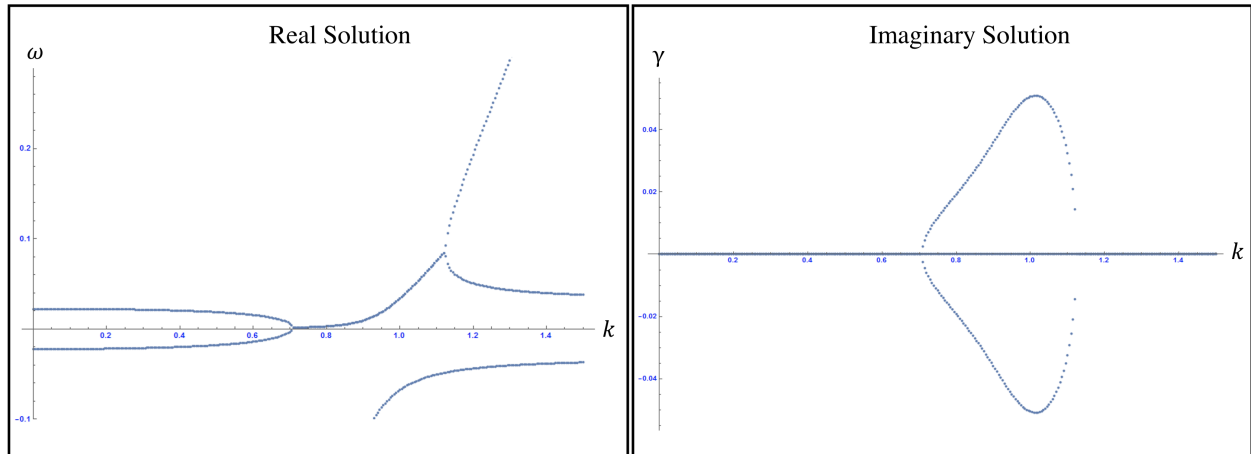Figure A.2: $n_e = 1 \times 10^{30}$ cm^{-3}, $\omega_{pe} = 5.64 \times 10^{16}$ rad/sec, $\omega_{pi} = \omega_{TO} = 1.32 \times 10^{15}$ rad/sec, $v_e^2 = 3.3 \times 10^{30}$ (m/s)^2

Buneman instability

$\omega_{TO} = 0$, $v_e = 0$

Figure A.3: $n_e = 1 \times 10^{30}$ cm^{-3}, $\omega_{pe} = 5.64 \times 10^{16}$ rad/sec, $\omega_{pi} = 1.32 \times 10^{15}$ rad/sec, $v_d = c/3$ m/s

Buneman instability with addition of lattice force

$\omega_{TO} = \omega_{pi}$, $v_e = 0$

Figure A.4: $n_e = 1 \times 10^{30}$ cm^{-3}, $\omega_{pe} = 5.64 \times 10^{16}$ rad/sec, $\omega_{pi} = \omega_{TO} = 1.32 \times 10^{15}$ rad/sec, $v_d = c/3$ m/s
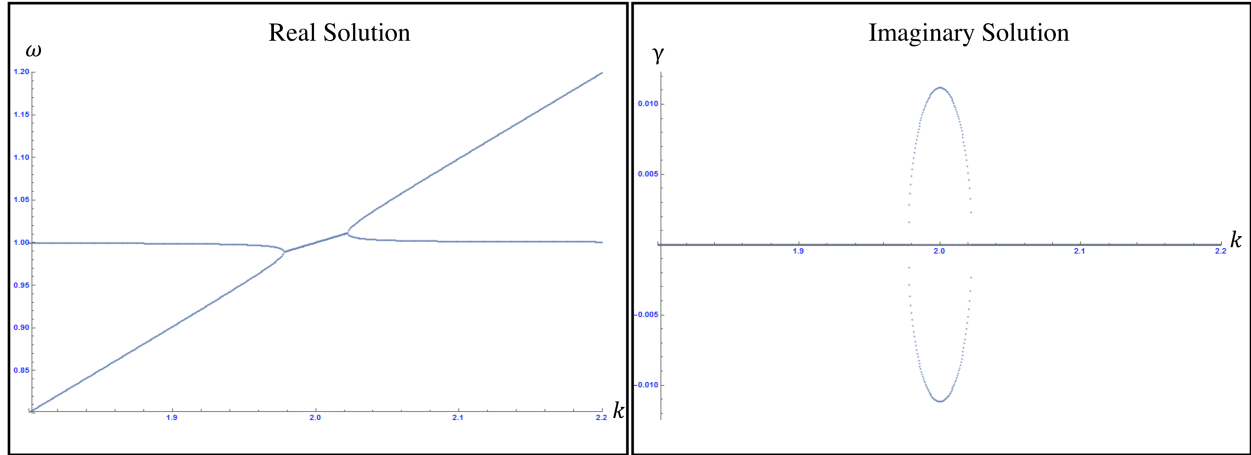
$\omega_{TO} = \omega_{pe}$, $v_e = 0$

Figure A.5: $n_e = 1 \times 10^{30}$ cm^{-3}, $\omega_{pe} = \omega_{TO} = 5.64 \times 10^{16}$ rad/sec, $\omega_{pi} = 1.32 \times 10^{15}$ rad/sec, $v_d = c/3$ m/s
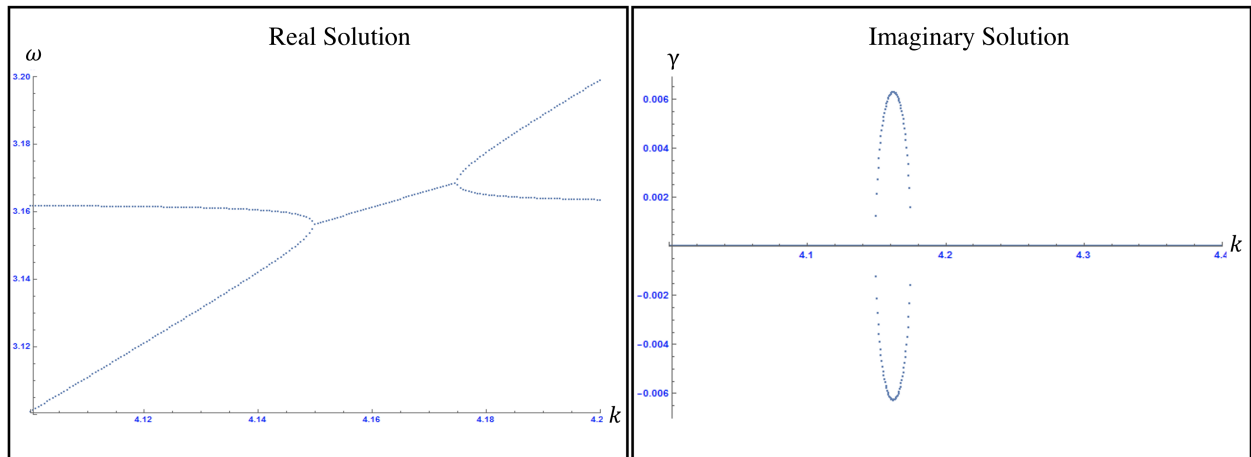
$\omega_{TO} > \omega_{pe}$, $v_e = 0$

Figure A.6: $n_e = 1 \times 10^{30}$ cm^{-3}, $\omega_{pe} = 5.64 \times 10^{16}$ rad/sec, $\omega_{TO} = 10 \times \omega_{pe}$, $\omega_{pi} = 1.32 \times 10^{15}$ rad/sec, $v_d = c/3$ m/s